Masterarbeit

Design of an Icing Wind Tunnel for UAVs

cand. aer. Joachim Wallisch

Juli 2020

Institut für Thermodynamik der Luft- und Raumfahrt
der Universität Stuttgart

Direktor: Professor Dr.-Ing. B. Weigand

Universität Stuttgart
INSTITUT FÜR THERMODYNAMIK DER LUFT- UND RAUMFAHRT
Direktor: Professor Dr.-Ing. B. Weigand
Pfaffenwaldring 31, 70569 Stuttgart, Germany · http://www.itlr.uni-stuttgart.de

Masterthesis

for cand. aer. Joachim Wallisch

Design of an Icing Wind Tunnel for UAVs

Motivation:

A key limitation to the operational envelope of medium-sized fixed-wing unmanned aerial vehicles (UAVs) today is the risk of atmospheric icing. In contrast to icing in general aviation, UAV icing is not well established and is an emerging research topic. We at NTNU want to investigate the possibility of building a subsonic wind tunnel with icing capabilities.

Such a wind tunnel consists of three main building groups: a conventional wind tunnel, a nozzle system for spraying droplets into the tunnel, and a cooling system to generate freezing temperatures. We envision an open return wind tunnel that will be placed inside a climate chamber with limited footprint. The objective of this thesis is to design the main components, determine power and cooling needs, and investigate suitable spray systems.

Tasks:

- Literature search on the topic of wind tunnel design and icing.
- Aerodynamic design of the wind tunnel components for given test specifications and size limitations. Estimating fan power and cooling requirements.
- CAD model of the final design alternatives.
- Critical discussion of design alternatives.

Location and duration:

The thesis is to be conducted at NTNU in Trondheim, Norway over a period of 6 months.

Supervisor:

- Prof. Dr.-Ing. habil. B. Weigand, ITLR
- Dr. Richard Hann, NTNU

Issue date: 20.01.2020

Delivery date: 20.07.2020

B. Weigand

Prof. Dr.-Ing. B. Weigand

Hiermit versichere ich, dass ich diese Masterarbeit selbstständig mit Unterstützung des Betreuers / der Betreuer angefertigt und keine anderen als die angegebenen Quellen und Hilfsmittel verwendet habe.

Die Arbeit oder wesentliche Bestandteile davon sind weder an dieser noch an einer anderen Bildungseinrichtung bereits zur Erlangung eines Abschlusses eingereicht worden.

Ich erkläre weiterhin, bei der Erstellung der Arbeit die einschlägigen Bestimmungen zum Urheberschutz fremder Beiträge entsprechend den Regeln guter wissenschaftlicher Praxis eingehalten zu haben. Soweit meine Arbeit fremde Beiträge (z.B. Bilder, Zeichnungen, Textpassagen etc.) enthält, habe ich diese Beiträge als solche gekennzeichnet (Zitat, Quellenangabe) und eventuell erforderlich gewordene Zustimmungen der Urheber zur Nutzung dieser Beiträge in meiner Arbeit eingeholt. Mir ist bekannt, dass ich im Falle einer schuldhaften Verletzung dieser Pflichten die daraus entstehenden Konsequenzen zu tragen habe.

…………………………………………………

Ort, Datum, Unterschrift

Abstract

Unmanned aerial vehicles are an emerging topic. They see increased use all over the world. Their use in geographic areas with cold climatic conditions causes new challenges. One particular challenge occurs when ice accumulates on the aircraft. Ice can accumulate when the aircraft flies through clouds with supercooled droplets. This phenomenon is called atmospheric icing. Icing has a negative influence on many components of the aircraft. Because icing on unmanned aerial vehicles is not understood completely, further research is necessary. For this purpose, experiments in special wind tunnels need to be done. To offer such a facility, this thesis was done to design a new wind tunnel for icing experiments on unmanned aerial vehicles.

The thesis starts with a short introduction into the topic. Afterwards, a literature review is given. Some general basics are presented that help to understand the other topics. The wide area of unmanned aerial vehicles is introduced and a more narrow part of the spectrum is selected that plays an important role in this thesis. A presentation of the topic of atmospheric icing follows. The physical background and possible effects are named as well as possible protection systems. The last part of this chapter is based on wind tunnels, their design, and the special needs of wind tunnels for icing experiments.

The third chapter contains the requirements and equations that were used during the design of the wind tunnel and all related considerations. This also includes the behavior of droplets in an icing wind tunnel and the pressure losses. Furthermore, the foundation for the calculation of the necessary cooling power of the wind tunnel is given.

The results are presented in the fourth chapter. First, the final design of the icing wind tunnel is presented. Then the characteristics of droplet flows inside this wind tunnel are calculated to achieve insight into the quality of the wind tunnel design. An overview of the pressure losses and the produced heat is given, divided into the single terms that are relevant. Finally, the results of a CFD simulation are given that was done to be able to check the quality of the design with a more powerful tool.

The last part of this thesis presents a short discussion of the results found during the work and provides recommendations on possible actions that should be done in the future.

Contents

List of Figures

List of Tables

List of Symbols

Latin Symbols

a	$\mathrm{m\,s^{-2}}$	acceleration
A	$\mathrm{m^2}$	area
AR		area ratio
$blockage$		blockage value
c_D		drag coefficient
c_{latent}	$\mathrm{J\,kg^{-1}}$	specific latent heat of fusion
c_p	$\mathrm{J\,kg^{-1}\,K^{-1}}$	specific heat capacity at constant pressure
c_v	$\mathrm{J\,kg^{-1}\,K^{-1}}$	specific heat capacity at constant volume
d	m	diameter
d		differential
d_h	m	hydraulic diameter
D	$\mathrm{m^2\,s^{-1}}$	diffusivity
$\dot{E}$	W	rate of change of internal energy
f		function
F	N	force
$\vec{g}$	$\mathrm{m\,s^{-2}}$	vector of gravity
H	m	height
k	$\mathrm{W\,m^{-1}\,K^{-1}}$	heat conductivity
K		pressure loss coefficient
K_{EXP}		pressure loss coefficient for expansions
K_{MESH}		mesh constant for pressure loss coefficient
K_{Re}		Reynolds number dependence of pressure loss coefficient
L	m	length
L_V	$\mathrm{J\,kg^{-1}}$	latent heat of vaporization
m	kg	mass
M		Mach number
$\dot{m}$	$\mathrm{kg\,s^{-1}}$	mass flow rate
Nu		Nusselt number
p	Pa	static pressure
P	m	perimeter
Pr		Prandtl number
p_T	Pa	total pressure
q	Pa	dynamic pressure
$\dot{Q}$	W	heat flux
r	m	radius

R	$\mathrm{m^2\,s^{-2}\,K}$	gas constant
Re		Reynolds number
S		drag area
Sc		Schmidt number
Sh		Sherwood number
t	s	time
T	K	temperature
$\vec{u}$	$\mathrm{m\,s^{-1}}$	speed vector of the droplets
v	$\mathrm{m\,s^{-1}}$	air speed
$\vec{v}$	$\mathrm{m\,s^{-1}}$	speed vector of the air
v_S	$\mathrm{m\,s^{-1}}$	speed of sound
$\dot{V}$	$\mathrm{m^3\,s^{-1}}$	volume flux
W	m	width
x	m	coordinate in streamwise direction
z	m	coordinate perpendicular to stream direction

Greek Symbols

γ		heat capacity ratio
δ	m	boundary layer height
Δ	m	surface roughness of the honeycomb cells
Δ		difference
ϵ		emissivity
ϵ		downstream influence of flow obstruction
θ	$^\circ$	angle
λ		friction coefficient
μ	$\mathrm{kg\,s^{-1}\,m^{-1}}$	dynamic viscosity
ν	$\mathrm{m^2\,s^{-1}}$	kinematic viscosity
ρ	$\mathrm{kg\,m^{-3}}$	density
σ	$\mathrm{W\,m^{-2}\,K^{-4}}$	Stefan-Boltzmann constant

Indizes

1		diffuser inlet plane
2		diffuser exit plane
a		ambient
air		value for air
C		convection
$circular$		circular diffuser shape
d		droplet
e		equivalent value
E		evaporation
$FLOW$		flow value
$Inlet$		value at the inlet of the spray nozzle
$latent$		latent heat

m		matching point
$projected$		projected dimension
R		radiation
$sensible$		sensible heat
$square$		square diffuser shape
TS		test section
$Water$		value of water
$wire$		value for the screen wire

Abbreviations

CFD		computational fluid dynamics
EASA		European Union Aviation Safety Agency
LWC	$\mathrm{kg\,m^{-3}}$	liquid water content
MVD		median volume diameter
PVC		polyvinyl chloride
UAV		unmanned aerial vehicle
IWT		icing wind tunnel

1 Introduction

1.1 Background & motivation

Even beyond classic passenger and freight transport, aircraft offer a wide range of possible uses. From the air, reconnaissance, surveillance, and search and rescue missions, especially of large areas, are often much easier than from the ground. Nevertheless, manned aircraft are not always the best choice for these applications. Sometimes unmanned aerial vehicles (UAVs) may be able to fulfill the task in comparable quality but cheaper and safer. For some missions UAVs even have huge advantages compared to manned aircraft. This is because the weight of a pilot can be saved and the design does not need to take a pilot into account. Hence, UAVs can be built much smaller than manned aircraft. Because of all these reasons, UAVs are experiencing increased popularity.

The use of UAVs in colder regions is however difficult. This is because the aircraft might experience icing. Icing occurs in clouds with supercooled liquid droplets. Therefore an aircraft can experience large accretions of ice on the whole vehicle if it flies through clouds under icing conditions without any protection system. These ice accretions can lead to severe problems, for example significant losses in aerodynamic performance if the ice accumulates on the airfoil as presented by Bragg et al. [1]. All impacts of ice accretions reduce the capability of the UAV or can even cause the aircraft to crash. Therefore, the risk of icing leads to a limitation in the use of UAVs. Even with an ice protection system, the deployment or flight in icing conditions is often associated with high risks.

Icing is not limited to UAV operations but also influences manned aircraft, see Kind et al. [2] or Peck et al. [3]. However, manned and unmanned aircraft are different in several characteristics. For example, UAVs are normally smaller and fly slower than manned aircraft. Therefore, manned and unmanned aircraft operate in different Reynolds number regimes. The difference in Reynolds number affects the accretion process and the consequent performance penalties, see Szilder and McIlwain [4] and Hann [5]. Therefore, a direct transfer of icing on manned aircraft to icing on unmanned aircraft is not possible. This is also why an implementation of the existing ice protection systems for manned aircraft into UAVs is not possible without an in-depth analysis, see Hann and Johansen [6]. The ice protection system must first be adapted to different characteristics of the UAV, e.g. the typically smaller size than manned aircraft.

1.2 The scope of the thesis

In-flight tests in icing conditions can be dangerous and it can be difficult to find icing conditions in nature. This and the wish for a better understanding of ice accretion processes on UAVs lead to the desire of having suitable icing wind tunnels. These wind tunnels shall be capable of providing realistic icing conditions and the necessary dimensions to test full-sized parts of a UAV. While some icing wind tunnels exist today, most of them are designed for manned aircraft. UAVs are typically smaller and operate at lower speeds. Therefore, it is often not possible to test icing on UAVs under realistic conditions in the existing icing wind tunnels. This thesis shall explore the design considerations for a low-speed icing wind tunnel that is capable to fit a real UAV airfoil and produce conditions typical for UAVs and icing conditions.

1.3 The outline of the thesis

The basics to understand icing and the special issues of unmanned aerial vehicles are given in Chapter 2. This chapter also contains an introduction into wind tunnels and icing wind tunnels. The methods used to develop the components of the wind tunnel are introduced in the third chapter. Chapter 3 also contains the necessary steps to calculate the behavior of water droplets inside the wind tunnel. The final design of the wind tunnel and its environment are presented in Chapter 4. Also the results of droplet calculations are presented in that chapter. A discussion about the results and a recommendation on further work can be found in Chapter 5.

2 Background

In this chapter, the necessary basics for the thesis are presented. First, the topic of atmospheric icing is introduced. Afterwards, the necessary knowledge of flow dynamics as well as droplet behavior is presented. After this, there is a definition for the term UAV and a short overview of different designs and possible areas of operation. A special concern are the differences between manned and unmanned aircraft and how these differences influence icing. This is followed by a short explanation on wind tunnels and different design options in general, and a special look on changes that need to be made to transform a conventional wind tunnel into an icing wind tunnel.

2.1 Atmospheric icing

An objective for every aircraft, no matter if manned or unmanned is to be able to operate also under bad weather conditions. One potentially hazardous weather condition for aircraft is icing. A physical description of the icing process was given by Kind et al. [2]. Their description shall be summarized in the following paragraphs.

2.1.1 Basics of atmospheric icing

In-cloud icing or just called icing might occur once an aircraft flies through a cloud with supercooled liquid water droplets. For the presence of supercooled droplets, the ambient temperature needs to be below the freezing temperature that is 0 °C for water. If these supercooled droplets are too big to follow the streamlines around the body, they will hit the surfaces that are facing upstream as can be seen in Figure 2.1. This can have

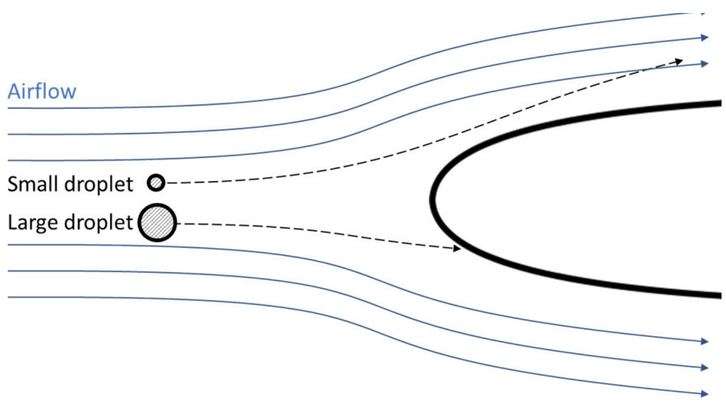

Figure 2.1: Trajectories of droplets around a leading edge. Adapted from Hann and Johansen [6].

effects at several parts of the airplane, e.g. the propellers, the wings, the pitot tubes, or sensors. However, this thesis will solely focus on icing on the airfoils.

The impacting droplets may either freeze completely or partially, depending on the heat balance in the impact region. This heat balance is formed by multiple terms, but two have a major influence. When droplets freeze, the enthalpy of fusion gets set free and tends to warm the surrounding. On the other side, due to convection, heat is transferred from the surface towards the colder surrounding air. Three cloud parameters play an important role in the question which term is bigger: The ambient temperature, the liquid water content (LWC), and the median volume diameter (MVD). The LWC is a measure of the amount of water in the cloud. It can be interpreted as a kind of density and is noted in mass per volume. The MVD is the diameter where 50% of the whole volume of all the droplets is made up of bigger droplets and 50% of smaller droplets. Therefore the MVD is a diameter representative for the different droplet sizes in the droplet cloud.

For problems with low LWC and/or temperatures well below 0 °C, the convective heat transfer is high enough to transport away the heat that is released when the droplets freeze. Therefore the temperature of the surface and the accumulated ice stays below 0 °C and the droplets freeze entirely when they hit the surface. This case is known as rime ice. The shape of rime ice is rather simple as the droplets just freeze where their trajectory hits the surface. A characteristic of rime ice is its rather milky look that can be seen in Figure 2.2(a). This milky look arises because air is trapped between the freezing droplets and the surface.

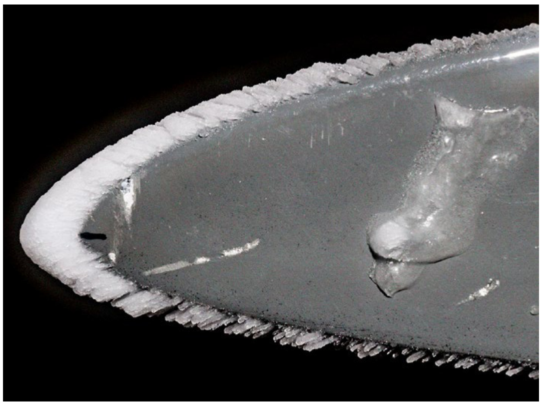

(a) Typical look of a rime ice case. Adapted from Hann and Johansen [6].

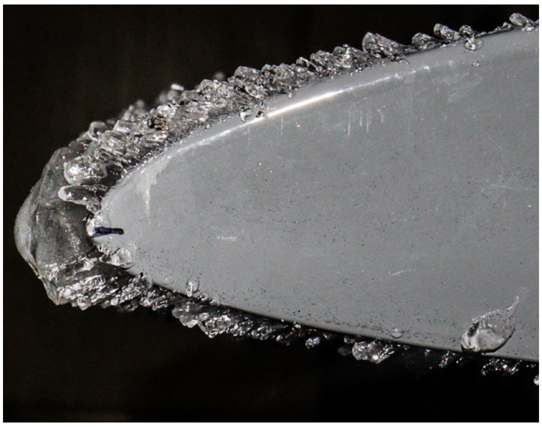

(b) Typical look of a glaze ice case. Adapted from Hann and Johansen [6].

Figure 2.2: Examples for different ice cases.

In cases of temperatures just slightly below the freezing temperature and/or high LWC, the temperature of the ice is around 0 °C and just a part of the droplet freezes when hitting the surface. The other, still liquid, part runs back on the airfoil and may eventually freeze downstream. This behavior is even more probable for high MVDs. This is because then the droplets have a higher mass and the enthalpy of fusion is much larger. This case is called glaze ice. Because of the runback water, it has a much more complex shape and it looks clear as just few air is trapped inside as can be seen in Figure

2.2(b). Often in real flights, the aircraft will experience a case between glaze and rime ice. This case is called mixed ice.

The European Aviation Safety Agency [7] (EASA) has certification guidelines for aircraft. If a company wants an aircraft to be certified and be allowed to also start and fly during icing conditions, the aircraft needs to be able to deal with specified icing conditions. The EASA works closely with the Federal Aviation Administration on the topic of icing and both agencies have the same rules for icing conditions. As no certification guideline is available for UAVs, typically the guidelines for large passenger transport aircraft are used. The certification guidelines of the EASA consist of a continuous and an intermittent maximum the aircraft might experience. To describe the icing surrounding, the EASA uses three different parameters. These parameters are the already stated ambient temperature, the LWC, and the MVD. The parameters of the maximum icing conditions an aircraft might experience are visualized in Figure 2.3(a) for the continuous case and in Figure 2.3(b) for the intermittent case. While the values are higher for the intermittent case, clouds with these more severe conditions are typically smaller. Nevertheless, to obtain a complete coverage of icing conditions, these parameters have to be fulfilled. The icing conditions contain MVDs between 15 μm and 50 μm and LWCs up to almost 3 g m^{-3}. Additionally, the figures show that the LWC the aircraft might experience is much higher for temperatures around 0 °C than for lower temperatures.

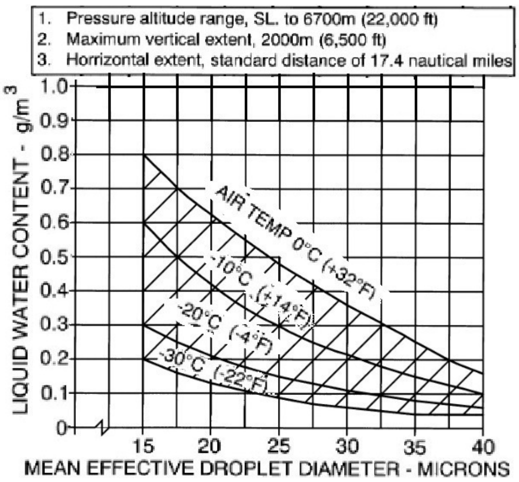

(a) Maximum parameters of continuous maximum icing conditions. Adapted from European Aviation Safety Agency [7].

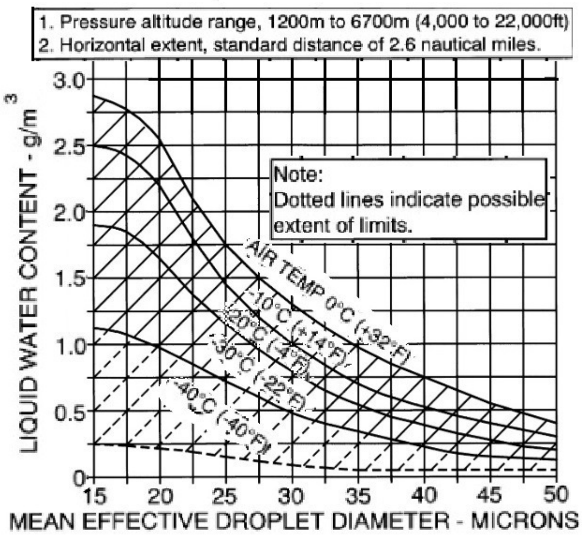

(b) Maximum parameters of intermittent maximum icing conditions. Adapted from European Aviation Safety Agency [7].

Figure 2.3: Icing conditions stated in the certification guidelines for aircraft for two different types of clouds.

2.1.2 Typical ice shapes on airfoils

To understand why ice accretions can lead to big aerodynamic performance losses and therefore influence the abilities of the aircraft, the next passages shall show the four most typical ice shapes and how they change the aerodynamics of the airfoil. However, as the major topic of this work is the design of an icing wind tunnel, the overview will not go too much into detail. For further information see Bragg et al. [1], as this was also used as the main source for the next passages.

At the beginning of the ice accretion, no matter whether it is glaze or rime ice, the occurring phenomenon is called ice roughness. The ice will always be rough to a certain degree. In this first phase, however, the surface is not yet covered in a way that the shape of the airfoil is significantly changed. Therefore also the flowfield around the airfoil is almost unchanged compared to an ice-free situation. The resulting rough zones are three-dimensional and have a height typically larger than the boundary layer. Therefore ice roughness can be thought of like normal surface roughness. If the roughness is high enough, it may cause transition of the flow or even separation. This leads to less lift and higher drag.

A typical shape for glaze ice conditions is a horn at the surface. A horn ice shape can be seen in Figure 2.4. At the horn's top, the flow will separate if the horn is too high and if the pressure gradient is not favorable. The size of the separation zone behind the horn and accordingly how huge the aerodynamic losses are, depends on several attributes, for example the angle of attack, the height of the horn, and its location on the surface. Horns on the lower surface just have an influence on the lift coefficient of low angles of attack, but they add up to the drag in a significant manner and therefore can not be neglected. An other problem arising with ice horns is that the induced separation zones may fluctuate. Vortices develop behind the horns and the separation bubble moves with the reattachment point varying over time.

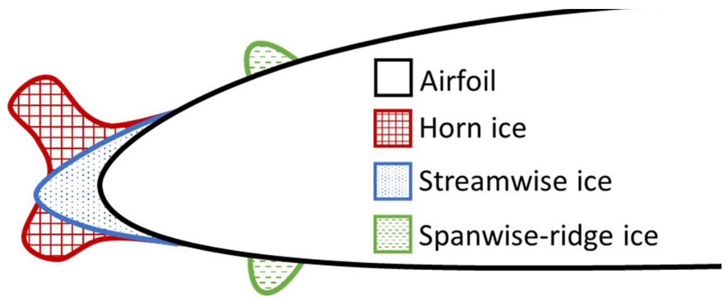

Figure 2.4: Typical ice shapes on an airfoil. Adapted from Hann and Johansen [6].

While horn shapes are typical for glaze ice conditions, so-called streamwise ice is typical for rime ice conditions. The droplets just freeze where they hit the surface and therefore form an ice shape that does not really change the shape of the airfoil unless the accretion time is long. This shape can also be seen in Figure 2.4. Because of the little change of shape, the aerodynamic effects are minor compared to the horn shapes. Anyway, as there is a passage from the ice to the clean surface, an adverse pressure gradient may occur and lead to flow separations. The aerodynamic impact of streamwise ice is however still much smaller than in the horn case. This is because a separation does not occur on the leading edge but further downstream.

The ice shapes presented so far were all a result of the icing cloud itself. The fourth shape is a result of the use of an ice protection system. Ice protection systems are normally just in the region of the leading edge and therefore a huge part of the airfoil is not heated or protected similarly. Once such a system is used but does not remove every part of the incoming water, the remaining water will run back and may eventually freeze downstream at a part of the surface that is not heated. An exemplary plot of how the ice shapes may then look like is given in Figure 2.4. Because of the shapes it produces, most of the time it is called spanwise-ridge ice. For the earlier mentioned horn shapes, the boundary layer is not developed yet and the stagnation point of the flow might even be at the horn. However, the spanwise ridges are located much farther downstream and therefore see a boundary layer that might already have transitioned due to roughness on the surface. The ice acts on the flow in a similar way an obstacle would do and causes separation of the flow with vortices inside the separation and reattachment region. As in the previously mentioned cases, this reduces the maximum lift and the stall angle, while increasing the drag at the same time.

Depending on the ambient situation, an aircraft might accrete one or more of the mentioned ice shapes during the flight through a cloud. While the different shapes form for different reasons, all of them reduce the aerodynamic performance of the aircraft. Numerical simulations by Fajt et al. [8] showed that a decrease of 35% in lift coefficient and 33% in corresponding angle of attack as well as an increase of drag by 160% might occur in the worst-case conditions for a continuous case. Experiments by Hann et al. [9] also showed severe losses in the aerodynamic performance of an iced airfoil. These performance losses and the risks of losing an aircraft are so high that often UAVs stay grounded once they may experience icing conditions as reported by Peck et al. [3].

2.1.3 Ice protection systems

It is the goal to use aircraft also during weather conditions that are not perfect. Therefore ice protection systems need to be introduced that allow flight under potentially dangerous icing conditions at least for a short time.

Ice protection systems can typically be divided into two categories: de-icing and anti-icing systems. As described by Lawson [10] de-icing concepts shed the ice once there is more ice accretion than a specified threshold. Anti-icing devices are active continuously and prevent the accretion of ice. There are a lot of different possibilities and this topic is not of much importance for this work. Therefore, the works of Lawson [10], Hann and Johansen [6] and Hann et al. [11] are recommended to get further insight into ice protection systems. These literature contain a further overview of the techniques used and how the necessary energy is provided.

2.2 Basics about flow dynamics and droplet behavior

Some knowledge is important for the understanding of the topic of icing on UAVs.

2.2.1 Flow dynamics

Every time air moves relatively to a body, certain flow phenomena occur. The region close to the surface is of special interest. This is because directly at the surface, the velocity is zero. Due to friction, the surrounding flow is also slowed down. Therefore a region develops where the velocity is smaller than in the free stream. This region is called the boundary layer.

An important parameter to characterize the flow behavior is the Reynolds number

$$Re = \frac{vL}{\nu} \tag{2.1}$$

with a typical velocity of the air v, a characteristic length L of the body, and the kinematic viscosity ν. The Reynolds number is an indicator of whether a flow is laminar or turbulent. Laminar flows are well structured and regular. Turbulent flows are chaotic, unsteady and three-dimensional. For low Reynolds numbers, the laminar flow effects dominate. If the Reynolds number is increased, the flow will be transitional and finally the turbulent flow effects will dominate. Laminar flows normally have a thinner boundary layer than turbulent flows. However, the velocity profile of turbulent flows is steeper at the surface than the velocity profile of a laminar flow. As the flow characteristics of laminar and turbulent flows differ strongly, the Reynolds number plays an important role in flow experiments and calculations.

Another dimensionless group that is often used to describe a flow is the Mach number

$$M = \frac{v}{v_S} = \frac{v}{\sqrt{\gamma R T}} \tag{2.2}$$

that describes the ratio of the local air speed v to the local speed of sound v_S. The speed of sound is calculated with the heat capacity ratio γ, the specific gas constant R, and the local temperature T. For $M < 0.3$, a flow can be considered to be incompressible as stated by Anderson [12]. If a flow is incompressible, the substantial change of the density ($D\rho/Dt$) is zero.

If a flow around a body is no longer able to follow the contour, the phenomenon is called separation. Separation can happen once the pressure downstream is higher than upstream as explained by Anderson [12]. The flow then has to fight against this so-called adverse pressure gradient. The air close to the wall has already a lower velocity than the air outside the boundary layer. At a certain point, the flow might stop and change its direction due to the adverse pressure gradient. This is called separation. As the velocity close to the wall is higher in turbulent boundary layers than in laminar ones, turbulent flows have a higher margin before they separate. Separation increases the pressure losses drastically and is therefore normally not wanted. The point of separation is defined as the position where the wall-normal gradient of the velocity is zero.

If air flows through a duct, the continuity equation

$$\rho v A = const. \tag{2.3}$$

describes the averaged air velocity v at every position in dependency of the air density ρ and the area A of the cross-section. Essentially the continuity equation says that all the air that enters a cross-section also has to leave it. If a flow is incompressible, the density might be considered to be constant in the whole flow and can therefore be eliminated from the continuity equation.

Equations for the calculation of flow properties for flows through ducts often require the diameter of the duct. For ducts with a cross-section that is not circular, the hydraulic diameter

$$d_h = \frac{4A}{P} \tag{2.4}$$

can be used instead. The area A of the cross-section and the length P of the perimeter of the duct are needed to calculate the hydraulic diameter.

To have an idea about the characteristics of certain flow situations, either experiments can be done or the governing equations can be solved. Solving the governing equations analytically is possible for few, mostly rather basic cases. This is because the governing equations are nonlinear partial differential equations. With the improvements in computer performance over the last decades, a new possibility arrived, the use of Computational Fluid Dynamics (CFD). As CFD just played a minor role in this thesis, just the basics of CFD simulations will be explained. For a more thorough introduction into the topic, Versteeg and Malalasekera [13] can be checked.

The first step of a CFD simulation is to divide the geometry of interest into many smaller geometries. The power of a CFD simulation is to transform the conservation equations into algebraic equations and solve them with an iterative method for each of the small geometries and combine the results. Many different iterative solvers and models to decrease the complexity of the calculation can be used. As the computational grid needs to be very fine to calculate turbulence without a model, the simulations would need much computational power and time. Therefore turbulence is normally modeled. To model turbulence, many different methods are known, see Versteeg and Malalasekera [13].

2.2.2 Droplets

If a flow contains droplets, both the flow and the droplets will influence each other. The influence of the flow on the droplets' path can be formulated with Newton's second law

$$F = ma \tag{2.5}$$

that explains that the acceleration a of a body depends on the driving force F and the mass m of the body.

The temperature of the droplets is influenced by the temperature of the air flow. To calculate the change of temperature of a droplet due to the air, a heat balance can be done as explained by Gates et al. [14]. However, depending on the case, different heat terms are relevant. The relevant heat terms will be discussed in section 3.3.2.

2.3 Unmanned aerial vehicles

Summarized under the term unmanned aerial vehicle (UAV) are all kinds of aircraft that are able to fly without a pilot on board. The vehicle might be piloted from a ground station, navigate according to a programmed route or be able to autonomously adapt its course.

2.3.1 UAV database

There is a wide range of different sizes and types of UAVs. To get a first impression about the wide variety of UAVs, a database was created. To do so, information for 93 different UAVs that are used today, were used during the last decades, or are in the final stage of production was collected. The information was found on the homepages of the manufacturers or the US military, but also in scientific papers, newspaper articles, and online articles. The database contains main information like the wingspan, the maximum take-off-weight or the cruise speed of UAVs, but also chord lengths and the airfoil profile where available. The database is printed in Appendix A.1 in a short form with just the most important parameters. The complete form of the database with all parameters can be found on the enclosed CD.

2.3.2 Design and missions of UAVs

While the smallest UAVs have dimensions of just a few centimeters and weigh much less than a kilogram, large UAVs have proportions comparable to a small airliner like the Airbus A320 or the Boeing 737. The type of the aircraft depends on the size and especially the mission. Two different techniques are regularly used to generate lift. The first one is a fixed-wing configuration. As it is the case for normal airliners, the wing is fixed and rigid and the aircraft needs to have an additional source of thrust. An example for a fixed-wing UAV is the PX-31 by Maritime Robotics that is shown in Figure 2.5(a). The goal for many UAV missions is to stay in the air for many hours. Good aerodynamics is important to fulfill this requirement. Therefore the wing design is very important. The parameters that typically denote a wing are the wingspan, the chord length, and the aspect ratio. The aspect ratio is the ratio of the wingspan to the mean chord length of the wing.

As an alternative to fixed wings, rotary wings can be installed, as used for manned helicopters for example. While a helicopter usually just has one rotor, UAVs might have multiple rotors. UAVs with multiple rotors are often also called multicopters. The Agras T16 by DJI is an example of rotary wing UAVs and is shown in Figure 2.5(b).

As already mentioned, the design of the UAV depends to a high degree on the missions it shall be able to execute. Very small UAVs are usually of the rotary-wing type as a fixed wing would be much wider to produce the same lift as the rotors. For larger UAVs however, the fixed-wing type is much more common. In history, most of the missions have been military, for example to transport and shoot missiles or for the purpose of surveillance. But with better knowledge of UAVs and therefore cheaper solutions, also governments, civil and customer applications play an increasing role.

(a) The PX-31 by Maritime Robotics is an example of a fixed-wing UAV. Adapted from Maritime Robotics [15].

(b) The Agras T16 is an example of a rotary-wing UAV. Adapted from DJI [16].

Figure 2.5: Examples for the different types of UAVs

Possible areas of usage are surveillance, search and rescue, atmospheric monitoring, cargo, or as communications relay as summarized by DeGarmo [17]. These missions lead to a wider range of UAV designs and areas of use. However, the most missions are still endurance-driven. This means that the purpose of the UAV is to stay in the air for a very long time. Further applications can be found in DeGarmo [17]. While in the past, UAVs were used most of the time in rather warm areas, a lot of the stated applications have great value all over the world.

2.3.3 Differences to normal aircraft

Although UAVs exist in a huge range of sizes, most UAVs are much smaller than typical manned aircraft. But not just the size is different for manned and unmanned aircraft. Because of their size, their different mission profiles and the lack of a pilot on-board, UAVs have a lot of different parameters compared to manned aircraft as presented by Hann and Johansen [6]. In this subsection, typical differences between UAVs with a wingspan of a few meters and typical manned aircraft will be worked out. This is important because of two reasons. First, the differences between UAVs and manned aircraft lead to differences in the way the ice accumulates on each aircraft. Second, the effects that the ice accretion has on the aircraft are different for manned and unmanned aircraft because of their different characteristics as was explained by Hann and Johansen [6].

Gent et al. [18] showed that smaller aircraft normally experience higher droplet impingement rates. This is because the droplet trajectory is changed stronger by large objects. As UAVs normally have smaller leading edge diameters than manned aircraft, the droplet trajectories are changed less for UAVs than for manned aircraft. Therefore more droplets hit a UAV than a manned aircraft. Additionally, the typically smaller chord lengths of UAVs lead to the phenomenon that the ice accretes over a larger part of the airfoil than it is the case for larger aircraft. Because a larger part of the aircraft is covered with ice for smaller aircraft than for bigger ones, also the weight of the ice accretion compared to the weight of the aircraft is often higher for smaller aircraft.

Manned aircraft typically travel at much higher velocities than unmanned aircraft. This is because many UAV missions are endurance driven and the endurance increases with lower speeds. This has multiple effects. First, higher speeds lead to higher aerodynamic heating. Aerodynamic heating is the effect of the heating of a surface due to a flow being decelerated close to it. According to Anderson [12], the aerodynamic heating rate varies with the cube of the velocity. The velocity of manned aircraft is therefore often high enough to prevent icing if the air temperature is not too low. Due to the lower speed of most UAVs, aerodynamic heating however is typically negligible for UAVs. A second effect of lower speeds is that the aircraft flies through a smaller amount of air at the same time span and therefore typically accumulates a smaller amount of water at the same time. However, because of the lower velocities also the time an aircraft spends inside icing conditions normally increases and therefore counterbalances this second effect.

As both the size and the speed of UAVs is typically lower than the values of manned aircraft, also the Reynolds number is lower for the flights of UAVs. Simulations by Szilder and McIlwain [4] showed that decreasing Reynolds numbers lead to a smaller mass of ice that accretes on a body. However, the size of the ice accretions compared to the size of the aircraft is bigger for lower Reynolds number. Therefore the aerodynamic performance suffers more for aircraft with lower Reynolds numbers. This was also researched by Hann [5] and Hann and Johansen [19]. Additionally, the lower Reynolds numbers lead to longer laminar parts of the flow over the airfoil. As explained, laminar flows are more prone to separate. As one of the effects of the ice shapes normally is to encourage separation, laminar flows are even worse for these ice shapes.

The altitude of UAVs can vary a lot. While some UAVs operate just a few meters above the ground, others fly much higher than typical airliners. Therefore, finding a typical altitude is almost impossible. However, Gent et al. [18] state that a height of about 3000 ft to 5000 ft (900 m to 1500 m) is the most dangerous concerning icing conditions. The typical cruise altitude of airliners of about 30,000 ft to 40,000 ft (9000 m to 12,000 m) is less severe for icing. This is because the temperatures in these heights are much lower. Therefore, fewer supercooled droplets are in the air, but more ice crystals. These ice crystals lead to other problems for aircraft but are not reviewed in this work. Hence, aircraft at lower altitudes are more prone to see problems with icing.

Another point that arrives with the flight without a pilot on board is that the icing situation must be recognized by sensors. Especially if the UAV is flying completely automatically, the aircraft must be able to recognize autonomously the icing conditions and find the correct solution on its own. As ice can also accrete on sensors and make them worthless, UAVs are much more prone to crash than manned aircraft where a pilot can maybe recognize problems with sensors in time and may be able to act in time to secure the aircraft.

2.4 Wind tunnels

While more detailed CFD simulations are possible nowadays due to increasing computational power, wind tunnels are still needed to test and validate components or even complete aircraft. They offer the possibility to do measurements at the parts of an aircraft in a controlled environment. This controlled environment leads to a big advantage of icing tests in wind tunnels compared to icing tests in nature. While in nature the tests can be done only when icing conditions exist, the conditions can easily be set in a wind tunnel.

2.4.1 Basics of wind tunnels

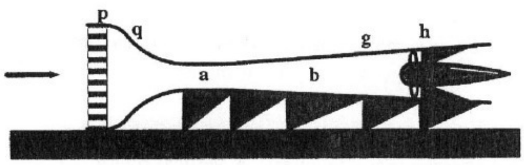

(a) Schematic look of an open-return wind tunnel. Adapted from Barlow et al. [20].

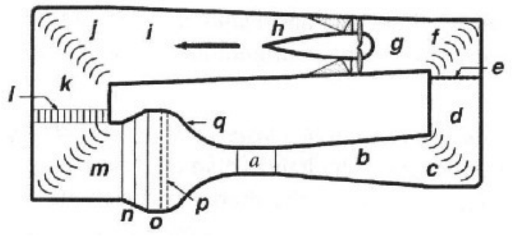

(b) Schematic look of a closed-return wind tunnel. Adapted from Barlow et al. [20].

Figure 2.6: Examples for the different types of wind tunnels

Wind tunnels are devices that cause air to flow past a test object. For most cases, this leads to similar characteristics of the flow field as if the object was moving through air. Therefore wind tunnels are a great possibility to perform measurements on objects moving through air like cars, trains, or aircraft. Normally wind tunnels are characterized by two different classes. An open-return wind tunnel sucks air from the surrounding. This air flows through the wind tunnel and is then blown into the surrounding again as can be seen in Figure 2.6(a). The open-return wind tunnel can be either placed outside where it has to deal with wind influences or inside a room where sufficient clearance from the walls must be ensured. The other option is to have a wind tunnel of the closed-return type. Closed-return wind tunnels have a return section through which the air circulates continuously while the wind tunnel is working as can be seen in Figure 2.6(b). Barlow et al. [20] list some advantages for each of the two types. An open-return tunnel is typically smaller in space. This also leads to less initial costs for an open-return wind tunnel as it consists of less structure. Furthermore, it is also better for visualization experiments as it sucks fresh air and does not just recirculate the air inside the tunnel. However, due to the return section, with a closed-return tunnel, the flow quality can be controlled better and less conditioning is needed. Additional advantages of a closed-return wind tunnel are that they need less power and that they are typically less noisy.

The second distinguishing criterion of a wind tunnel is the section that contains the test object. While it was either a closed or open duct in the past, over the last years slotted walls have seen increased use. Open test sections allow easier access to the model and offer some advantages in bluff body aerodynamics. For aeronautical experiments, a closed test section is often more reasonable. Because open test sections suck air from the surrounding that was not accelerated before, the power need is higher for open than for closed test sections.

In the following paragraphs, the most typical parts of a wind tunnel and their tasks shall be presented. This passage is based on the work of Barlow et al. [20]. This book can also be recommended for further and more detailed research on the topic of wind tunnels.

The most important part of a wind tunnel is its **test section**. The test object and all the measuring equipment is mounted inside the test section. The goal is to be able to use the largest possible part of the test section for the experiment. Otherwise, the construction and energy costs would be higher without any need. Therefore the conditions inside the test section have to be constant over a large part of the cross-section to have comparable conditions over the whole area in which the measurements take place. Not only spatial uniformity of the conditions is important, but also temporal uniformity. To ensure this, there should not be any separation inside the wind tunnel. Additionally, the power unit and the cooling unit have to be strong enough to keep the volume flow and the temperatures constant. As turbulence can have a strong influence on the results of experiments, normally the aim is either a design with as less turbulence as possible or a design with a specified turbulence level. The test section is usually of the closed type. If the test section is closed, most of the time its cross-sectional shape is either rectangular or circular.

A **contraction** is placed upstream of the test section. Due to acceleration through this nozzle, variations in velocity decrease. This is however not the main reason for placing a contraction upstream of the test section. Upstream of the nozzle are flow conditioners. To reduce their pressure losses, the velocity should be low. Therefore an acceleration between the flow conditioners and the test section is needed that is provided by the nozzle. While a 1D-analysis indicates falling pressure and therefore no risk of separation, it is different in reality. Regions with increasing pressure will occur near the wall in the area of the beginning and the end of the nozzle. This leads to the need for a good design of the nozzle because separation reduces the flow quality.

The mentioned flow conditioners can be divided into honeycombs and screens. Both are placed inside a part with constant cross-section that is called **settling area** because of the low speed inside. Honeycombs are small pipes inside this section. As the flow has to go through those narrow pipes, the velocity component normal to the pipe is reduced and the flow is straightened into the direction of the test section. According to Barlow et al. [20], the most common honeycombs are either round, square, or hexagonal. Those shapes can also be seen in Figure 2.7(a). Screens on the other side are grids consisting of regularly arranged thin wires as can be seen in Figure 2.7(b). The non-uniformity of the flow is reduced over a screen because the flow resistance is higher for higher velocities than for low velocities. A downside of screens is that they are responsible for rather high pressure losses.

Downstream of the test section is the **diffuser** which is of diverging cross-section. The divergence is placed at this position to have a good pressure recovery and therefore fewer pressure losses in the wind tunnel. If the increase in cross-section is too big over a short length, the diffuser might experience separation. This will reduce the flow quality in the test section and might lead to unsteadiness. Barlow et al. [20] however state

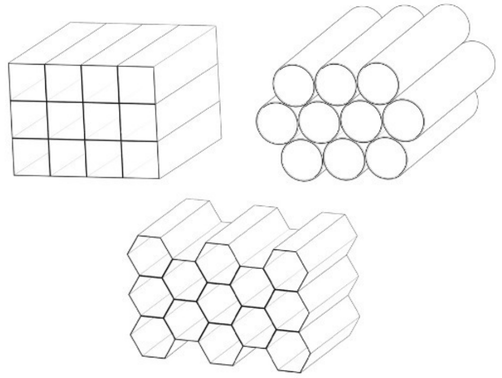

(a) Different options for honeycombs. Adapted from Kulkarni et al. [21].

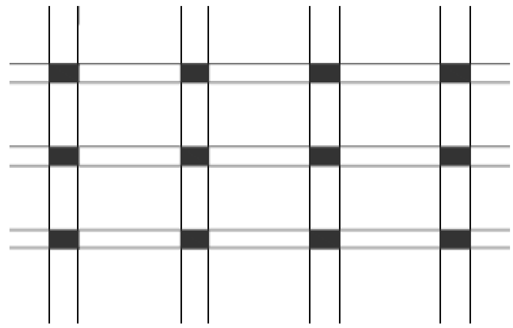

(b) Schematic of a turbulence screen. Adapted from Arifuzzaman and Mashud [22].

Figure 2.7: The typical flow conditioners.

that separation can be accepted to a small degree as the upstream impact is usually negligible.

As pressure losses take place all over the length of the wind tunnel, a **power unit** is needed. Additionally, this fan is required to force the air through the wind tunnel. In open-return tunnels, this power unit is either placed downstream of the diffuser or upstream of the settling area. The installed fan shall balance the pressure losses and provide a steady air flow through the wind tunnel.

In a closed-return wind tunnel, the **return duct** will follow after the diffuser. The return duct consists of corners and ducts to connect the end of the diffuser and the beginning of the settling area. Also, the power unit is placed somewhere inside the return duct, often after the second of four corners.

2.4.2 Icing wind tunnels

Icing wind tunnels contain two new components compared to common wind tunnels as explained by IEA Wind Task 19 [23]. A spray system needs to be included to inject water droplets into the wind tunnel. Furthermore, extra cooling is required to cool the tunnel to subzero temperatures. Closed-return tunnels often have heat exchangers included in their channel to cool the fluid constantly. Open-return tunnels need to have external cooling and are therefore often placed inside a climate chamber that provides the necessary cooling power.

Today already several icing wind tunnels exist. A list with all icing wind tunnels was compiled by IEA Wind Task 19 [23]. However, most of those wind tunnels are designed for manned aircraft. Manned aircraft typically are larger and faster than UAVs and therefore also the icing wind tunnels for manned aircraft are bigger and designed for higher air speeds. This is why most of the existing icing wind tunnels operate at velocities of $75\,\mathrm{m\,s^{-1}}$ or higher, for example the icing wind tunnel at CIRA [24] or the Icing Research Tunnel at NASA Glenn Research Center [25] and therefore way faster than the air speed of most UAVs. Also, some icing wind tunnels with up to $20\,\mathrm{m\,s^{-1}}$ or

$25\,\mathrm{m\,s^{-1}}$ are available. While this is fast enough to test some UAVs, it is too slow for most of them. Hence, very few of the existing icing wind tunnels can be used for UAV experiments. Two examples for icing wind tunnels that can be used for icing experiments on UAVs are the VTT icing wind tunnel (see Tiihonen et al. [26]) and the icing tunnel at Cranfield University [27]. There is however a need for more test capabilities. This is why new icing wind tunnels are necessary that are specially designed for UAV tests.

The basic wind tunnel design presented this far is perfectly suited for experiments with airfoils. The situation is more complex when rotary-wing UAVs or manned helicopters are the objects of interest. Flemming et al. [28] mounted the main rotor of a helicopter inside a conventional icing wind tunnel. Their results fit well to theoretical predictions. With common wind tunnels, it is however not possible to account for the centrifugal forces that are important for helicopter icing as explained by Brouwers et al. [29]. These authors therefore used a test facility that has the spray nozzles mounted to the ceiling. The complex field of doing icing experiments on rotary-wing aircraft also lead to different methods of simulating icing during the flight. To do so, the rotorcraft is flying inside a droplet cloud produced by an aircraft flying in front or by a stationary facility as can be seen in Cao and Chen [30]. However, all of those systems have shortcomings. Therefore research on test facilities for rotorcraft icing is still necessary.

2.4.3 Scaling

During the planing of experiments, often the question arises whether it is possible to scale the experiment. Scaling is especially desired if the tests would otherwise be very expensive or the number of suitable test facilities is very small. Often the available space is a problem and therefore smaller models of the real parts are used. The dimensionless quantities which are the most important for describing the flow should be the same for the experiment and the real-life situation. If this is possible, a transfer of the results of the experiment to real life situations is rather easy.

Scaling the models for icing experiments is however very difficult. This is because 18 dimensionless quantities have to be matched for complete equality according to Kind et al. [2]. The large number can be explained with the need of matching the dimensionless parameters for three different fields: the air flow, the trajectories of the droplets and the impingement and freezing of the droplets. For conventional wind tunnel tests most often just the air flow is of interest. Then normally a matching of Reynolds and Mach number between test and reality is necessary. Matching some of the dimensionless quantities for icing wind tunnel experiments is rather easy, for example by using air and water as in the real life situation. Especially matching the quantities for the impingement and freezing is however much more difficult. Therefore, until today, scaling of the results of icing experiments can not be done with good accuracy. Hence, experiments have to be done with full-scale models to have meaningful results. This is however a bigger problem for manned aircraft than for UAVs. As manned aircraft are typically larger and operate at higher speeds than UAVs, they need bigger test facilities and the tests cost much more. Therefore, scaling would be more beneficial for manned aircraft than for unmanned.

3 Methods

This chapter is about the steps it took to design the components of the icing wind tunnel. Decisions made during this design are explained. Several rules and equations were used to design the components of the wind tunnel. In this chapter, these rules and equations are presented and explained. The necessary formulas to analyze the behavior of the droplets are also shown and commented on. To calculate the pressure losses and the necessary cooling power, certain equations were needed. Those are presented in this chapter as well.

3.1 Basic decisions

Some decisions have to be made before the wind tunnel components can be designed. An open-return design was chosen to decrease the dimensions of the icing wind tunnel and the costs. A closed test section was chosen as otherwise droplets could leave the icing wind tunnel and change the LWC and the MVD. Additionally, closed test sections reduce the power requirements for the wind tunnel fan. It has to be considered that not all droplets will hit the airfoil. The ones that do not, will travel further in the tunnel. If the fan was placed after the diffuser, droplets would hit the fan. Those droplets would accrete there and influence the fan's performance. Therefore the fan will be placed at the inlet of the wind tunnel. The resulting order of components inside the icing wind tunnel can be seen in Figure 3.1 and is fan(A), wide-angle-diffuser(B), settling area(C), nozzle(D), test section(E), diffuser(F).

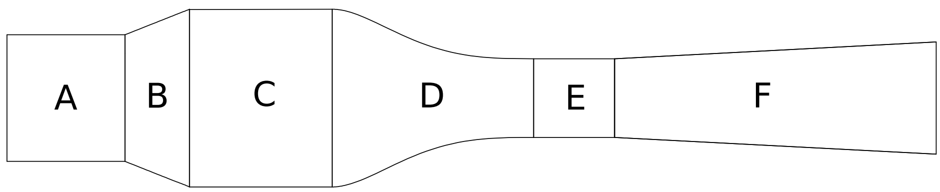

Figure 3.1: Order of components in the resulting icing wind tunnel.

3.2 Components of the wind tunnel

3.2.1 Test section

The first question when designing a wind tunnel is the necessary size of the test section. The test section contains the test object and therefore is the area of the most interest.

The size of the test object must not be too big compared to the size of the test section. The main design parameter is the blockage. The blockage is calculated as the fraction of the projected area of the test object to the cross-sectional area of the test section. The projected area of the test object is the area the shadow of the test object would have on a plane normal to the wind tunnel direction. Because of the blockage, the effective flow area decreases. Therefore the flow velocity increases as well as the surface stresses. This leads to results that are different from results in free air where no blockage occurs. To keep the differences small, the blockage should be at most 10% according to Barlow et al. [20].

Not only the test object has an influence on the flow inside the test section but also the boundary layer. The influence of the boundary layer is active until a distance of the wall of 10% of the distance between the two walls for the icing wind tunnel of Bansmer et al. [31] and 12% for the wind tunnel of Arifuzzaman and Mashud [22]. As this is the case on both sides of the wind tunnel, the boundary layer will influence about 20% of the width and height. However, this is just a rule of thumb. Hence, it should only be used as a first hint for the test section dimensions. For the final icing wind tunnel design, a calculation of the boundary layer thickness should be done. The steps to calculate the boundary layer thickness exactly are presented in section 3.7.

The flow at the transition from the nozzle to the test section is unsettled and contains disturbances. Therefore a short length with a constant cross-section is recommended before the test object. Barlow et al. [20] recommend to allow the flow a settling length of about 0.5 times the hydraulic diameter of the test section for this purpose. This settling length will be included directly into the test section. Therefore the test section should not be too short in order to have good flow conditions. If the test section is too long however, the boundary layer will be rather thick and will decrease the effective flow area massively. If a longer test section is needed or if the influence of the boundary layer is already too big, the test section can be designed with a very small opening angle. Then the effects of the boundary layer growth and the increasing cross-sectional area balance each other. Barlow et al. [20] recommend an opening angle of 0.5° in this case.

3.2.2 Nozzle

While the test section has a constant cross-sectional shape, the nozzle contracts towards the test section. Therefore the first decision for the design of a nozzle is its contraction ratio, also called area ratio. According to Barlow et al. [20], nozzles normally have a contraction ratio between 6 and 12 but also smaller and larger values are used. High contraction ratios lead to better flow quality and reduced speed at the upstream end. At the same time, high contraction ratios lead to bigger and longer components upstream of the test section.

Once the area ratio is known, the length is the next topic to think about. This is because short nozzles have a higher chance of separation, while long nozzles increase the wind tunnel length. Eckert et al. [32] collected data from existing wind tunnels. With those results, they estimated how long a nozzle should be depending on the ratio of inlet and outlet diameter. The data are shown in Figure A.1. While a few wind tunnels have shorter nozzles, they do recommend to not go below the shown minimum value.

Finally, the nozzle contour is important as well for the separation and also for the droplet behavior. According to Barlow et al. [20], the wall radius of the curvature at the wider end should be higher than at the smaller end. This is done to reduce the chance of separation inside the nozzle.

Different nozzle designs were compared for this task. For the ease of comparison, they are written all in the same form: z stands for half the width or height of the nozzle and the subscript TS describes the test section. The length of the nozzle is L, x is the coordinate in flow direction. The value AR denotes the contraction ratio of the nozzle. The first nozzle design is the **AVA nozzle** which contour is

$$\frac{z(x)}{z_{TS}} = \left(\sqrt{AR} - 1\right)\left(1 - \frac{x}{L}\right)^3 \left[2 - \left(1 - \frac{x}{L}\right)^3\right] + 1 \tag{3.1}$$

according to Bansmer et al. [31].

The second nozzle design is the **Witoszynski nozzle** whose contour

$$\frac{z(x)}{z_{TS}} = \frac{1}{\sqrt{1 + \left(\frac{1}{AR} - 1\right)\frac{\left[1 - \left(\frac{x}{L}\right)^2\right]^2}{\left[1 + \frac{1}{3}\left(\frac{x}{L}\right)^2\right]^3}}} \tag{3.2}$$

is also given by Bansmer et al. [31].

Bell and Mehta [33] compared different contraction designs. One was a **third order polynomial** with the contour

$$\frac{z(x)}{z_{TS}} = \sqrt{AR} - \left(\sqrt{AR} - 1\right)\left[-2\left(\frac{x}{L}\right)^3 + 3\left(\frac{x}{L}\right)^2\right]. \tag{3.3}$$

The same authors also recommended a **fifth order polynomial** with the contour

$$\frac{z(x)}{z_{TS}} = \sqrt{AR} - \left(\sqrt{AR} - 1\right)\left[6\left(\frac{x}{L}\right)^5 - 15\left(\frac{x}{L}\right)^4 + 10\left(\frac{x}{L}\right)^3\right]. \tag{3.4}$$

Brassard and Ferchichi [34] proposed an **improvement to the fifth order polynomial**. To do this, they introduced a transformation function $f\left(\frac{x}{L}\right)$. This function has to be defined for $0 \leq \frac{x}{L} \leq 1$ with a value $0 < f\left(\frac{x}{L}\right) < 1$. Then the equation changes to

$$\frac{z(x)}{z_{TS}} = \left[-\left(6\left(\frac{x}{L}\right)^5 - 15\left(\frac{x}{L}\right)^4 + 10\left(\frac{x}{L}\right)^3\right)\left[1 - \sqrt{\frac{1}{AR}}^{\,1/f(x/L)}\right] + 1\right]^{f(x)}. \tag{3.5}$$

As will be explained in the next chapter, it is beneficial for the droplet behavior if the point of steep contraction is further upstream. As the paper by Brassard and Ferchichi [34] indicates, values of $f\left(\frac{x}{L}\right)$ close to 1 lead to the contour being steep in a more upstream position. Therefore $f\left(\frac{x}{L}\right) = 0.7$ was chosen for this thesis.

The last contour checked in this work is made up of two **matched cubics** as recommended by Morel [35]. The exact equations are copied from Martin [36]. The equation for the first cubic is

$$\frac{z(x)}{z_{TS}} = \left(\sqrt{AR} - 1\right)\left[1 - \frac{1}{\left(\frac{x_m}{L}\right)^2}\left(\frac{x}{L}\right)^3\right] + 1 \tag{3.6}$$

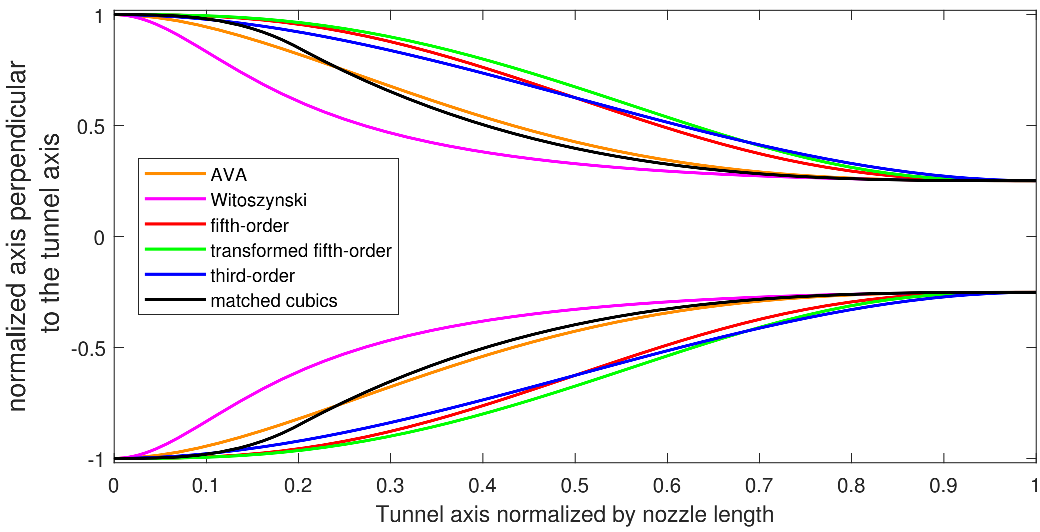

Figure 3.2: Comparison of the different nozzle contours for an area ratio of 9.

and the equation for the second cubic is

$$\frac{z(x)}{z_{TS}} = \frac{\sqrt{AR}-1}{\left(1-\frac{x_m}{L}\right)^2}\left(1-\frac{x}{L}\right)^3 + 1. \tag{3.7}$$

The coordinate x_m is the coordinate in x-direction where the two cubics meet. To have a steep contraction further upstream, a low value of x_m is beneficial. This is why $x_m = 0.2$ was chosen.

All nozzle contours are compared in Figure 3.2. It can be seen that the AVA contour, the Witoszynski contour, and the contour with the matched cubics have a larger slope on an upstream position than the other nozzle contours. This will be important in the following chapter.

Another parameter that can be chosen is the cross-sectional shape of the nozzle. Most of the nozzles are designed circular. Some sources report a higher chance of separation for rectangular shaped nozzles. This is due to the secondary flow between the corners and the centerline. Mehta [37] however states that the corner flow stays localized in the absence of separation. Therefore a rectangular nozzle cross-section is also possible. If separation occurs inside rectangular nozzles nevertheless, Barlow et al. [20] recommend using corner fillets to give the nozzle an octagonal shape. These fillets should however be continued through the test section as well. Downie et al. [38] did calculations of rectangular shaped contractions with changing aspect ratios. Their calculations showed that designs with changing aspect ratios are possible. However, they also stated that the point of maximum slope should be at the same position for both the vertical and the horizontal walls.

3.2.3 Settling area

The settling area contains the honeycombs and the turbulence screen. In the case of an icing wind tunnel, also the spray system is located in the settling area.

The honeycombs are typically placed furthest upstream. For the design of the honeycombs, Barlow et al. [20] recommend a length-to-diameter ratio between 6 and 8. The same authors also state that around 150 honeycombs per settling chamber diameter should be used. This would result in a total of 25000 honeycombs.

The turbulence screens damp the flow non-uniformity. To do so a high blockage of the air flow is necessary. The blockage is described by the value of the porosity. The porosity is the ratio of the area the flow can pass through to the total cross-sectional area of the settling area. Lower values of porosity therefore increase the damping of the non-uniformities. However, according to Barlow et al. [20] the screens must have a porosity greater than 0.57. Otherwise the flow inside the test section would be unstable. The maximum value of a useful porosity is 0.8 according to Barlow et al. [20].

Mehta and Bradshaw [39] recommend to keep a distance of 0.2 times the hydraulic diameter of the settling area between turbulence screens. They also stated that the distance between the last screen and the nozzle entry should be about 0.2 settling area diameters. Barlow et al. [20] recommend using a total length of 0.5 times the hydraulic diameter for settling areas that contain one honeycomb section and one turbulence screen.

3.2.4 Wide-angle diffuser

Because the fan is chosen to be on the upstream end and not on the downstream end, the fan is upstream of the settling area. As the fan is normally smaller in size than the settling area, a diffuser is needed to connect the fan with the settling area. To keep the length of the diffuser short, typically very high opening angles are chosen. Therefore separation would occur if no action was taken. To prevent separation, different methods can be used. Mehta and Bradshaw [39] report that the most common method is to include screens in the diffuser. A design rule was formulated by the same authors for the usage of screens. Figure A.2 shows the possible total opening angles of a wide-angle diffuser for different area ratios and different numbers of screens. The screens should be spaced equally inside the diffuser according to Mehta and Bradshaw [39] if no position of the diffuser is more prone to separate than the others. The first screen should normally be placed very close to the entrance of the diffuser. This is because the rapid opening at the entrance often leads to separation already. Other passive options are to use splitters or vanes to reduce the effective opening angle of the diffuser. Also vortex generators or suction can be used to prevent separation. Those methods however are much more complicated, also because they are active systems.

3.2.5 Fan

The equations to calculate the total pressure losses of the wind tunnel are explained in Section 3.4. Additionally to compensating the pressure losses, the fan must also be able to deliver the necessary volume flow

$$\dot{V} = uA \tag{3.8}$$

through the wind tunnel. For $\rho = const.$, the volume flow is the same in the whole wind tunnel. Therefore it is easiest to calculate the maximum volume flow with the conditions at the test section. This is because the maximum speed at the test section is a requirement for the wind tunnel and the cross-sectional area of the test section needs to be known before being able to design the other components.

Different fan options can be used to compensate for the pressure losses and deliver the necessary volume flow. For this thesis, three possible fan section designs are described.

The first one is the use of a **centrifugal blower**. Mehta and Bradshaw [39] describe the advantage of centrifugal fans to be that their performance is typically more stable over a wider range of loads. Another argument for centrifugal blowers is that the shape of the exit can vary and be either rectangular or square. This is an advantage as a change of shape needs to take place if the fan and the test section have different shapes. Such a change of shape can introduce problems with the flow quality and even lead to separation. The biggest argument against the use of a centrifugal blower is that they need a lot of space. Often the length of a centrifugal blower is about two times the length of an axial fan with comparable power.

The second option is the use of one **axial fan**. According to Savio Srl [40], axial fans are typically smaller, lighter, and less expensive than centrifugal blowers. Additionally, according to this source, no direct impact of the choice of the fan on the flow quality can be seen. As axial fans are always circular, they fit good for circular wind tunnels and can also be introduced into square ones without many problems. If axial fans shall be included in wind tunnels with rectangular cross-sections, it requires more effort however, as a change of shape needs to take place between the test section and the fan.

The third possibility is the use of **multiple axial fans** as proposed by Hernández et al. [41]. One of the advantages of this option is that smaller fans can be chosen. This decreases the costs for the fans. Additionally smaller fans in diameter are normally also shorter in length. Therefore probably less space would be needed compared to the other options. Another advantage is that designs with different amounts of fans in each direction are possible. Hence, also a rectangular fan section shape can be achieved. However, there is one big disadvantage. With the use of multiple fans, the uniformity of the flow might be affected negatively. Most of the time when multiple fans are used, they are placed downstream of the test section. This normally has lower influences on the flow quality inside the test section. In our case, the fan is placed upstream of the test section. Therefore shortcomings in flow quality or flow uniformity may have a huge downstream influence and decrease the quality of the measurements inside the test section strongly.

3.2.6 Diffuser

As already mentioned the task of the exit diffuser is to ensure a good pressure recovery. Flow separation can maybe be accepted until a certain degree. This is why Barlow et al.

[20] recommend an equivalent conical angle

$$\theta_e = arctan\left(\frac{r_2 - r_1}{L}\right) = arctan\left(\frac{1}{2}\frac{\sqrt{AR} - 1}{L/d_1}\right) \tag{3.9}$$

between 2° and 3.5°. The hydraulic radii r_i and hydraulic diameters d_i are measured at the entrance position 1 and the exit position 2 of the diffuser. The recommended area ratio of the diffuser is between 2 and 3. The resulting diffuser length should be about 3 or 4 times the test section length. While those recommendations and rules are developed for closed-return tunnels, with a small safety margin they can also be applied for open-return wind tunnels. The cross-sectional shape of the diffuser is not too important, although a cross-section with corners might increase the risk of separation a little bit.

3.3 Droplets inside the tunnel

As explained in the previous chapter, droplet clouds normally contain a range of different droplet sizes. The distribution needs to be known to do calculations for certain MVDs. Otherwise, the different behavior of droplets with a smaller or bigger diameter than the MVD will not be considered. This would lead to errors if the results are compared to real-life experiments. According to Gent et al. [18], the most common approach to rebuilding the distribution that occurs in nature is the Langmuir D distribution. These authors also state that this distribution is well suited to cover the typical droplet distribution of a spray system of an icing wind tunnel. The distribution of droplet sizes according to Langmuir D is shown in Table 3.1. Hence, the biggest droplets will be about 2.22 times bigger than the MVD. This is why simulations are done with way bigger droplet diameters than the MVDs that are necessary for obtaining flight allowance by the EASA.

The temperature of droplets when they are injected into the wind tunnel will be different from the temperature the droplets shall have when reaching the test object. The same will usually be true for the velocity of the droplets. Therefore calculations on the development of the droplet velocity and temperature need to be done.

diameter/MVD	fraction of LWC [%]
0.31	5
0.52	10
0.71	20
1.00	30
1.37	20
1.74	10
2.22	5

Table 3.1: Droplet size distribution with the Langmuir D distribution according to Langmuir and Blodgett [42].

3.3.1 Droplet velocity and trajectories

The velocity of a droplet inside the wind tunnel can be calculated with the equations of motions. For a single droplet, the equation of motion becomes

$$m_d \frac{d\vec{u}}{dt} = -m_d \vec{g} + \frac{1}{2} \rho_{air} A_d c_D \left| \vec{u} - \vec{v} \right| (\vec{v} - \vec{u}) \tag{3.10}$$

according to Gates et al. [14]. The same authors also state that the droplets can be assumed to be rigid spheres. Therefore their mass is

$$m_d = 4/3 \pi r_d^3 \rho_d. \tag{3.11}$$

The second term on the left side is the time derivative of the droplet velocity $\vec{u}$. The first term on the right side denotes the gravitational forces. Gravitation is just relevant for the direction pointing towards earth. Then the gravitation $g = 9.81\,\mathrm{m\,s^{-2}}$ is active. The second term on the right side describes the drag forces. The drag force depends on the difference of the velocity of the droplets $\vec{u}$ and the velocity of the air $\vec{v}$. The projected area of the droplet

$$A_d = \pi r^2 = 0.25 \pi d^2 \tag{3.12}$$

is taken into account as well as the drag coefficient c_D. As water droplets in icing wind tunnels can usually be assumed to be rigid spheres, the equation of Morrison [43] for the drag coefficient

$$c_D = \frac{24}{Re} + \frac{2.6 \left(\frac{Re}{5.0} \right)}{1 + \left(\frac{Re}{5.0} \right)^{1.52}} + \frac{0.411 \left(\frac{Re}{2.63 \cdot 10^5} \right)^{-7.94}}{1 + \left(\frac{Re}{2.63 \cdot 10^5} \right)^{-8.00}} + \frac{0.25 \left(\frac{Re}{10^6} \right)}{1 + \left(\frac{Re}{10^6} \right)} \tag{3.13}$$

can be used in this case. The velocity in the calculation of the Reynolds number is the velocity difference between air and droplet. Bansmer et al. [31] also calculated the speed of droplets during their wind tunnel design. However, they used a different equation to calculate the drag coefficient. A comment about their choice and the influence can be found on the CD.

To solve equation 3.10, the velocity of the air needs to be known. If the contour of the nozzle is known, also the cross-sectional area of the nozzle is known at each position. With this information and the continuity equation, the velocity can be calculated. As the wind tunnel will operate at low Mach numbers, the density can be assumed to be constant. Therefore the equation can be simplified and just the velocity at one spot needs to be known. The air speed at the test section is usually the target velocity of the droplets. This is because the droplets adjust asymptotically to the air speed. As the velocity of the air at the exit of the nozzle is the same as inside the test section, the air speed at each position can be calculated with

$$v(x) = \frac{v_{TS} A_{TS}}{A(x)}. \tag{3.14}$$

The equation of motion is a differential equation. Both the derivative of the droplet velocity and the droplet velocity are included as well as the drag coefficient that also depends on the droplet velocity. Therefore an easy analytical solution is not possible. However, the derivatives can be assumed to be differences. With this step and a rearrangement of the different terms, the equation of motions can be formulated as:

$$\Delta u = \frac{1}{2}\rho_{air}\frac{A_d}{m_d}c_D\left|\vec{u}-\vec{v}\right|\left(\vec{v}-\vec{u}\right)\Delta t. \tag{3.15}$$

Now a time-step procedure can be used. Equation 3.15 is solved for every time step and the new velocity is summed up by the old velocity and the new calculated Δu. The required values for the droplet velocity on the right side of the equation can just be taken from the last time step. The droplet velocity at the first time step is the velocity that the droplets have when they leave the spray nozzle. The droplet velocity at the spray nozzle exit can roughly be calculated using the Bernoulli law according to the manufacturer of spray nozzles PNR [44]. It follows that the initial droplet velocity

$$u = \sqrt{\frac{2}{\rho}p_{Inlet}} \tag{3.16}$$

just depends on the density ρ and the pressure p_{Inlet} at the inlet to the spray nozzle. For spray nozzles that use air and water, ρ is the density of the mixture.

Therefore every information is given that is necessary to calculate the velocity of the droplet. To calculate the complete trajectories, the equation of motion 3.15 is solved again, but this time in y- and z-direction. This is done to check if droplets would hit the wall before reaching the test section and how they distribute inside the test section.

3.3.2 Droplet temperature

The temperature of the droplets can be calculated from the first law of thermodynamics. This results for the present case in the equation

$$\dot{E} = \dot{Q}_C + \dot{Q}_R + \dot{Q}_E \tag{3.17}$$

which contains four terms. The term on the left is the change of the droplet's internal energy over time

$$\dot{E} = \frac{4}{3}\pi r_d^3\rho_d c_v\frac{dT_d}{dt} \tag{3.18}$$

with the specific heat capacity at constant volume c_v and the droplet temperature T_d.

The first term on the right hand side is the rate of heat transfer due to convection

$$\dot{Q}_C = 4\pi r_d k\left(T_a - T_d\right)\frac{Nu}{2} \tag{3.19}$$

with the thermal conductivity of air k, the ambient temperature T_a, and the Nusselt number Nu. The Nusselt number is a dimensionless quantity that describes the heat transfer between a body and the surrounding air. As already mentioned, the droplets can be treated as spheres. Therefore the correlation for the Nusselt number of spheres by Knudsen and Katz [45]

$$Nu = 2 + 0.6Pr^{1/3}Re^{1/2} \tag{3.20}$$

can be used. The term Pr is the Prandtl number of air.

The second term on the right hand side is the heat flux due to radiation

$$\dot{Q}_R = 4\pi r_d^2 \sigma \epsilon_d \left(T_a^4 - T_d^4\right) \tag{3.21}$$

with the Stefan-Boltzmann constant $\sigma = 5.67 \cdot 10^{-8}\,\mathrm{kg\,s^{-3}\,K^{-4}}$ and the emissivity ϵ_d of the droplet. As recommended by Gates et al. [14], the emissivity will be taken to be 1.

The last term on the right hand side is the heat flux due to evaporation

$$\dot{Q}_e = 4\pi r_d L_v D \left[\frac{p_a}{T_a} - \frac{p_d}{T_d}\right] \frac{Sh}{2R}. \tag{3.22}$$

The equation contains the latent heat of vaporization of water L_v, the diffusivity of water vapor in air D, and the Sherwood number Sh. The Sherwood number is a dimensionless quantity that describes the mass transfer of a droplet to the surrounding air and can be calculated with

$$Sh = 2 + 0.6Sc^{1/3}Re^{1/2} \tag{3.23}$$

according to Knudsen and Katz [45]. The term Sc denotes the Schmidt number of air.

The importance of evaporation however is under discussion. For example, Bansmer et al. [31] neglected this term for their calculation of droplet behavior. Additionally, Gates et al. [14] also state themselves that the influence of evaporation is minor. In the designed icing wind tunnel the relative humidity of the air will be around one. This value indicates that the air is saturated. Therefore, there will be no droplet evaporation inside the icing wind tunnel and the evaporative term will be neglected in the following.

By rearranging the terms in equation 3.17, the following equation can be gained:

$$\frac{dT_d}{dt} = \frac{3\left(\dot{Q}_C + \dot{Q}_R\right)}{4\pi r_d^3 \rho_d c_v} \tag{3.24}$$

As was done for the equation of motion, the derivatives can be assumed to be differences. This yields

$$\Delta T_d = \frac{3\left(\dot{Q}_C + \dot{Q}_R\right)}{4\pi r_d^3 \rho_d c_v} \Delta t \tag{3.25}$$

and again a time-step procedure can be used. The temperatures in equations 3.19, 3.21 and 3.22 can be taken from the last time step.

The whole reason for designing an icing wind tunnel is to have steady real-flight conditions at the test section. To ensure this is the case, the equation of motions and the heat balance are calculated for different parameters. Additionally, all of the equations above are solved for different nozzles to determine which nozzle is the most suitable for the wind tunnel.

The given equations have been solved using MATLAB. The used MATLAB code can be found on the CD.

3.4 Pressure losses

All components of the wind tunnel lead to pressure losses. To choose a suitable fan, the pressure losses need to be known. Eckert et al. [32] presented rules and equations for the calculation of pressure losses. Almost all equations in this paragraph were taken from them. Therefore just the ideas that were not taken from them will be marked to enhance the readability of this section.

The total pressure loss of the wind tunnel can be calculated by simply adding up the pressure losses of each component. The equations used to calculate the pressure losses can only be used for rectangular, circular, or flat-oval shapes. The given equations calculate most of the times the pressure loss coefficient K rather than the real pressure loss. This pressure loss coefficient

$$K = \frac{\Delta p_T}{q} \tag{3.26}$$

is the non-dimensional pressure loss calculated with the loss in total pressure Δp_T and the dynamic pressure q. The dynamic pressure used to non-dimensionalize the loss in total pressure is taken at the smallest-area at the end of each section. Therefore

$$\Delta p_T = Kq = K\left(0.5\rho v^2\right) \tag{3.27}$$

is the equation to calculate the real pressure loss.

Pressure losses in **ducts with constant cross-section** are due to friction. The corresponding loss coefficient is

$$K = \frac{\lambda L}{d_h}. \tag{3.28}$$

The pressure losses depend on the friction loss coefficient λ. According to Eckert et al. [32], the friction coefficient for smooth walls is described by

$$\frac{1}{\sqrt{\lambda}} = 2\log_{10}\left(Re\sqrt{\lambda}\right) - 0.8. \tag{3.29}$$

To calculate the friction loss coefficient, the equation can be reformulated to

$$\lambda = \left[\log_{10}\left(\lambda Re^2\right) - 0.8\right]^{-2}. \tag{3.30}$$

Now, this equation can be solved iteratively by taking the value of the last iteration for λ on the right side to calculate a new value of λ. As start value, λ will be set to 1. 5 iterations normally lead to a value with sufficient quality.

The pressure loss in **contractions** is also mostly due to friction. The loss coefficient can be calculated approximately by

$$K = 0.32\frac{\lambda L}{d_h} \tag{3.31}$$

with the hydraulic diameter being the value of the test section according to Eckert et al. [32]. Contractions have different inlet and outlet areas and therefore a changing velocity over its length. Hence, a choice has to be made which Reynolds number is for the calculation of the friction loss coefficient. Barlow et al. [20] recommend using the average of the friction loss coefficient values at the inlet and the outlet.

The pressure loss in a **diffuser** is both due to friction and expansion. Eckert et al. [32] therefore published an equation for the corresponding loss coefficient

$$K = \left[K_{EXP} + \left(\frac{\lambda}{8sin\theta}\frac{AR+1}{AR-1}\right)\right]\left(\frac{AR-1}{AR}\right)^2 \tag{3.32}$$

that is made up of one term for the expansion losses and one for the friction losses. The friction loss coefficient has to be calculated with the entry Reynolds number according to Barlow et al. [20] and therefore is the same as for the test section. The value of the expansion parameter K_{EXP} depends on the cross-sectional shape of the diffuser and the semi-opening angle θ:

For circular cross-sections:

$$K_{EXP_{Circular}} = 1.033395 \cdot 10^{-1} - 1.1465 \cdot 10^{-2}(2\theta) \quad \text{for } 0^\circ < \theta < 1.5^\circ \tag{3.33}$$

$$\begin{aligned} K_{EXP_{Circular}} =& 1.70925 \cdot 10^{-1} - 5.84932 \cdot 10^{-2}(2\theta) + 8.14936 \cdot 10^{-3}(2\theta)^2 && (3.34)\\ &+1.34777 \cdot 10^{-4}(2\theta)^3 - 5.67258 \cdot 10^{-5}(2\theta)^4 - 4.15879 \cdot 10^{-6}(2\theta)^5 && (3.35)\\ &+2.10219 \cdot 10^{-7}(2\theta)^6 \qquad \text{for } 1.5^\circ < \theta < 5^\circ && (3.36) \end{aligned}$$

$$K_{EXP_{Circular}} = -9.66135 \cdot 10^{-2} + 2.336135 \cdot 10^{-2}(2\theta) \quad \text{for } \theta > 5^\circ \tag{3.37}$$

For square cross-sections:

$$K_{EXP_{Square}} = 9.62274 \cdot 10^{-2} - 2.07582 \cdot 10^{-3}(2\theta) \quad \text{for } 0^\circ < \theta < 1.5^\circ \tag{3.38}$$

$$\begin{aligned} K_{EXP_{Square}} =& 1.22156 \cdot 10^{-1} - 2.29480 \cdot 10^{-2}(2\theta) + 5.50704 \cdot 10^{-3}(2\theta)^2 && (3.39)\\ &-4.08644 \cdot 10^{-4}(2\theta)^3 - 3.84056 \cdot 10^{-5}(2\theta)^4 + 8.74969 \cdot 10^{-6}(2\theta)^5 && (3.40)\\ &-3.65217 \cdot 10^{-7}(2\theta)^6 \qquad \text{for } 1.5^\circ < \theta < 5^\circ && (3.41) \end{aligned}$$

$$K_{EXP_{Square}} = -1.1321685 \cdot 10^{-1} + 2.93315 \cdot 10^{-2}(2\theta) \quad \text{for } \theta > 5^\circ \tag{3.42}$$

The variable AR in the term for the friction losses denotes the area ratio over the diffuser.

At the **exit of an open-return wind tunnel**, the kinetic energy of the flow that leaves the wind tunnel is lost. The total pressure loss is therefore equal to the dynamic pressure of the flow at the exit. Using compressibility relationships, the dynamic pressure of the flow can be calculated under the assumption that the static pressure of the flow is equal to the atmospheric pressure. This results in a pressure loss coefficient of

$$K = \frac{2\left\{\left[1 + \left(\frac{\gamma-1}{2}M^2\right)\right]^{\frac{\gamma}{\gamma-1}} - 1\right\}}{\gamma M^2}. \tag{3.43}$$

The pressure loss coefficient of **honeycombs** was defined by Eckert et al. [32] to be

$$K = \lambda \left(3 + \frac{L}{d_h}\right)\left(\frac{A}{A_{FLOW}}\right)^2 + \left(\frac{A}{A_{FLOW}} - 1\right)^2 \tag{3.44}$$

with d_h being the hydraulic diameter of a honeycomb cell. The friction coefficient is calculated with

$$\lambda = 0.375 Re^{-0.1}\left(\frac{\Delta}{d_h}\right)^{0.4} \tag{3.45}$$

for $Re \leq 275$ and

$$\lambda = 0.214\left(\frac{\Delta}{d_h}\right)^{0.4} \tag{3.46}$$

for $Re > 275$. In those equations Δ is the surface roughness of the honeycomb cells. Additionally, the Reynolds number is calculated with the surface roughness and the air velocity. The term A_{FLOW}/A describes the ratio of the local flow area to the area of the local cross-section and is therefore equal to the porosity.

Every **structure inside the tunnel** leads to drag and therefore to pressure losses as well. The pressure loss coefficients can be calculated with

$$K = c_D \frac{S}{A_{FLOW}} \epsilon. \tag{3.47}$$

Because the pressure loss depends on the drag of the structure, the drag area S of the considered internal structure needs to be taken into account. Additionally, the term $\epsilon \geq 1$ is included that describes the influence of the drag on downstream components.

A part of the reason behind the use of **mesh screens** are the pressure losses. The corresponding loss coefficient in the form published by Eckert et al. [32]

$$K = K_{Re}K_{MESH}\left(1 - \frac{A_{FLOW}}{A}\right) + \left(\frac{A}{A_{FLOW}} - 1\right)^2 \tag{3.48}$$

contains two parameters. The dependence on the Reynolds number is taken into account with K_{Re}. For this value, both an equation and a graph are given. However, they do not match. As indicated by Barlow et al. [20] the calculation of pressure losses is rather inaccurate. Therefore the worse case will be considered in the design of this wind tunnel and the Reynolds number influence factor becomes

$$K_{Re} = 0.785\left(1 - \frac{Re_{wire}}{354}\right) + 1.01 \tag{3.49}$$

for $0 \leq Re_{wire} < 400$ and

$$K_{Re} = 1.0 \tag{3.50}$$

for $Re_{wire} \geq 400$. The Reynolds number of the wire Re_{wire} is built with the velocity at the settling area and the diameter of the screen wire. The mesh constant K_{MESH} depends on the material of the mesh. For average circular metal wire K_{MESH} becomes 1.3, for new metal wire 1.0 and 2.1 for silk thread.

The pressure loss over the **wide-angle diffuser** depends on its area ratio. Mehta and Bradshaw [39] published the following equation for the minimum pressure loss coefficient of a wide-angle diffuser with a given area ratio:

$$K \geq \frac{AR - 1}{1.14}. \tag{3.51}$$

3.5 Cooling power

During a run of the wind tunnel, heat is released in different ways. If there was no cooling included, the temperature of the air would rise rather quickly as calculations by Barlow et al. [20] show. As the designed wind tunnel will be placed inside a cooling chamber, the necessary cooling power of this chamber needs to be calculated. First, the fan produces heat while it is running. All of the energy supplied to the fan needs to be balanced by the cooling system. This is because a part of the energy is directly transferred into heat and the other part will eventually become heat due to frictional heating of the air flow at the walls of the icing wind tunnel. Second, cooling is required, as heat is transferred from the droplets to the air. This heat transfer takes place in two ways as explained by Bansmer et al. [31]. First, cooling is required to cool the droplets down from their initial temperature when they leave the spray nozzle to the air temperature. This term is called the sensible heat and can be calculated

$$\dot{Q}_{sensible} = \dot{m}_{water} c_{p,water} \Delta T \tag{3.52}$$

with the specific heat capacity at constant pressure c_p.

The second term for heat transfer between droplets and air is the latent heat. The latent heat is released when a droplet freezes on a surface. It is

$$\dot{Q}_{latent} = \dot{m}_{water} c_{latent,water} \tag{3.53}$$

and depends on the specific latent heat of fusion c_{latent} of water. To be able to calculate the two heat transfer terms, the flow rate of water

$$\dot{m}_{water} = \dot{V}_{air} LWC = (v_{TS} A_{TS})\, LWC \tag{3.54}$$

needs to be known that depends on the volumetric flow rate $\dot{V}$ of air.

3.6 Clearance requirements

As already mentioned, open return wind tunnels are often placed inside a cooling chamber. Therefore the walls of this chamber will limit the surrounding. Mehta and Bradshaw [39] recommend to obtain enough space in the room in which the wind tunnel will be placed. This is because they compare the path the flow takes between the outlet and the inlet to a badly designed return duct.

Greenway and Wood [46] did some experiments before they put their wind tunnel into a given room. They changed the distance between the wall and the inlet and measured the flow quality. For their wind tunnel, the area of the incoming flow needed to be at least 1.8 the area of the inlet of the wind tunnel to achieve a good flow quality. While this is just the result for one wind tunnel, it can still be used as a coarse rule of thumb for other designs.

3.7 Calculation of the boundary layer thickness

To calculate the necessary width of the test section, the boundary layer height needs to be known. As the thickness of boundary layers is different for turbulent and laminar flows, the type of the flow needs to be known before the calculation. Chmielewski [47] presents basic rules of thumb that are representative of typical conditions in wind tunnels. The beginning of the nozzle should be used as the leading edge of the boundary layer. Furthermore, they assume that the transition from laminar to turbulent flow takes place at 0.15 times the inlet radius. However, a different approach was proposed by Morel [35]. He recommends using the position of the last turbulence screen as the starting point for the boundary layer. To do the calculations conservatively, the starting point will be chosen at the last turbulence screen as recommended by Morel [35]. The point of transition however is assumed to be at 0.15 times the inlet radius of the nozzle as recommended by Chmielewski [47]. This is chosen as no suitable point of transition was given by Morel [35].

The equations for the thickness of boundary layers are usually just given for flat plates. The nozzle however is curved. Nevertheless, Schlichting [48] shows that as long as the radius of the curvature is much larger than the boundary layer height, the equations for flat plates can still be used. To do so, a virtual coordinate system is created with one axis following the wall contour and the second axis being perpendicular to the first axis. The equation for the boundary layer height of a laminar flow

$$\delta\left(x\right) = 5\sqrt{\frac{\nu x}{v}} \tag{3.55}$$

is given by Schlichting [48] as well as the equation for the boundary layer height of a turbulent flow

$$\delta\left(x\right) = 0.37x\left(\frac{vx}{\nu}\right)^{-1/5}. \tag{3.56}$$

A necessity for the calculation of the boundary layer height is to know the velocity of the air. However, the velocity is different at every position in the nozzle. To calculate the boundary layer height nevertheless, the nozzle is separated in a lot of small sections. At every location, the velocity can be calculated with the continuity equation. As the boundary layer height develops over the whole length between the turbulence screen and the test object, a method needed to be found to capture this development as well. To do so, at every position, an equivalent length was calculated. This is the length of a plate with the same boundary layer and velocity. Afterwards, the new boundary layer can be calculated with the equivalent length being increased by the length of the small part. This can be done through all the components starting from the last turbulence screen to the position of the test object.

This procedure to calculate the boundary layer height at the position of the test object is also included in the MATLAB script. It can therefore be found on the CD.

4 Results

In this chapter, first the design requirements that the icing wind tunnel has to fulfill are presented. With the requirements and the equations presented in the previous chapter, the design of the wind tunnel components is explained. The characteristics of droplets inside the tunnel are analyzed as well as the pressure losses and the cooling requirements. A preliminary CFD simulation is also presented in this chapter. Finally, design options for a smaller icing wind tunnel are given.

4.1 Icing wind tunnel design

Certain design specifications need to be defined to be able to calculate the size and power of the icing wind tunnel. The test objects that will be tested in this icing wind tunnel are typical UAV airfoils. Scaling of the results of experiments is always problematic and even more for icing experiments as presented in subsection 2.4.3. Therefore an objective for the icing wind tunnel is to simulate real-life situations of UAVs. This means that airfoils with life-sized chord lengths are supposed to be tested at typical flight velocities. Figure 4.1 shows how the UAVs in the created database in Appendix A.1 can be arranged into different categories for flight speeds. For this purpose, 5 UAVs with flight speeds over $60\,\mathrm{m\,s^{-1}}$ were excluded, because very large UAVs are out of scope for this work. This was also done to have a clearer picture of the typical flight speeds of UAVs without a too long axis. The plot shows that most UAVs have typical flight speeds between $15\,\mathrm{m\,s^{-1}}$ and $35\,\mathrm{m\,s^{-1}}$. The requirement resulting from this knowledge is to obtain speeds up to

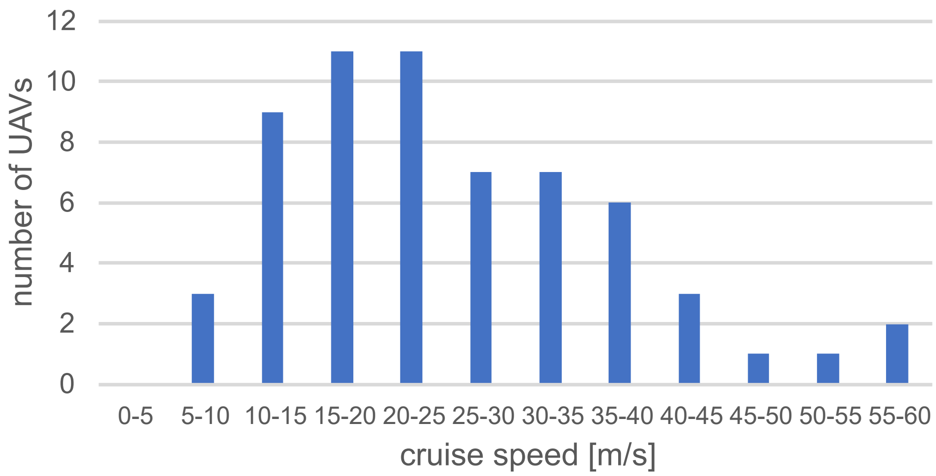

Figure 4.1: Division of UAVs according to their flight speed.

$35\,\mathrm{m\,s^{-1}}$ in the test section of the designed icing wind tunnel.

To find typical chord lengths for UAVs with speeds up to $35\,\mathrm{m\,s^{-1}}$, the table in Appendix A.1 was used again. However, data for chord lengths could just be found for 12 UAVs. As explained in Chapter 2, the chord length and the wingspan of an aircraft are linked with the aspect ratio. Therefore the chord length of the airfoil can also be calculated if the wingspan and the aspect ratio of the wing are known. While the wingspan is given for many UAVs, the aspect ratio is often not available. However, the average of the known aspect ratios in the database is about 11. Additionally, according to Nagel and Shepshelovich [49], typical aspect ratios for UAVs are about 12. Therefore, chord lengths were also calculated with the given wingspan and an estimated aspect ratio of 12. With this information, Figure 4.2 was created. It contains the known chord lengths, the chord lengths calculated with the known wingspan and aspect ratio, and the chord lengths calculated with the known wingspan and an estimated area ratio of 12. In total 61 data points are presented. According to this Figure, the most UAVs with speeds in the range to $35\,\mathrm{m\,s^{-1}}$ have chord lengths smaller than 0.4 m. Therefore a chord length of 0.4 m was chosen as the maximum for this icing wind tunnel.

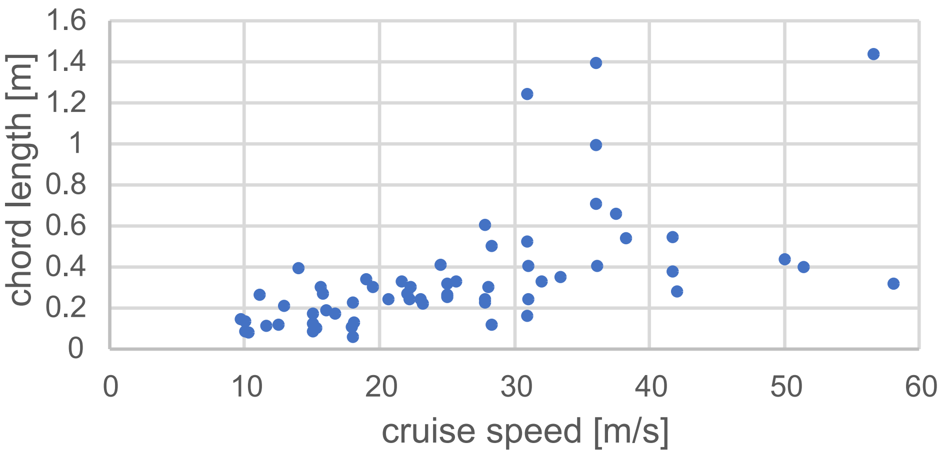

Figure 4.2: Chord lengths and cruise speeds of different UAVs.

While the chord length obviously has a huge influence on the length of the test section, it is also relevant for the height. This is because of the influence of the solid blockage effect that was presented in the previous chapter. The blockage depends on the thickness of the airfoil, its chord length, and the angle of attack. This will be further explained in the next subsection. For the design of this wind tunnel, an RG15 airfoil was taken as an example of the airfoils that will be tested. The coordinates of the airfoil surface are listed in Appendix A.3 as well as a plot of the profile with an angle of attack of 0°. Inside the wind tunnel, just the linear section of the c_L-α-curve shall be tested. This is because the linear part refers to those angles of attack where no stall appears. Figure 4.3 shows the c_L-α-curve for different Reynolds numbers with values taken by Airfoil Tools [50]. As higher angles of attacks lead to bigger and longer wind tunnels, a maximum angle of attack of about 8° was chosen. It follows that the test section must be high enough to contain the RG15 airfoil with a chord length of 0.4 m under an angle of attack of 8°

without significant blockage effects.

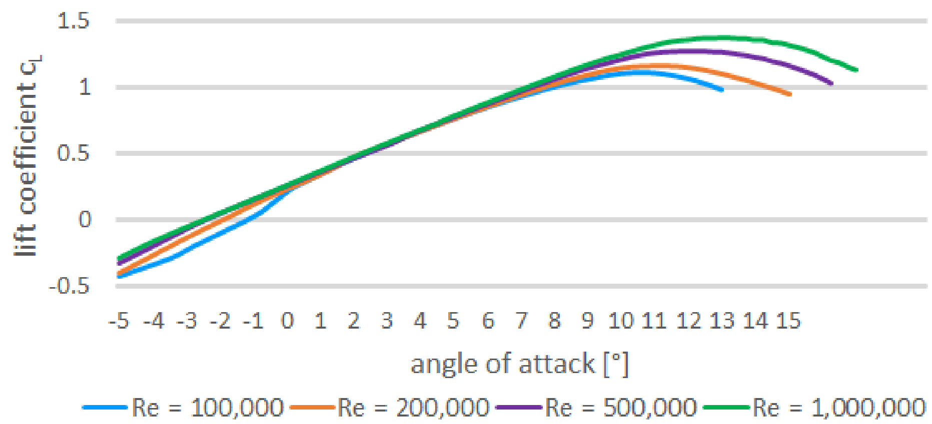

Figure 4.3: The lift coefficient of the RG 15 plotted over the angle of attack for different Reynolds numbers. Values taken from Airfoil Tools [50].

Although wind tunnels aim to have uniform conditions inside the whole test section, this is typically not true. Instead, the conditions will normally deviate in space and time. With icing experiments, an additional problem arrives. Ice shapes are already varying in nature. Therefore, ice shapes are normally measured on multiple locations along the span as was for example done by Hann [51]. The different measurements can be compared to have a better understanding of the icing wind tunnel quality and to have mean values that balance non-uniformity. For this icing wind tunnel, it shall be possible to do measurements over a width of 0.3 m. Therefore the test section must be wide enough to contain uniform flow conditions over a width of 0.3 m.

The EASA lists icing conditions for temperatures as low as −40 °C in their requirements for aircraft allowance. However, the LWC is decreasing with decreasing temperatures. Therefore, temperatures closer to 0 °C are more severe concerning the amount of water in the air. It was also shown by Fajt et al. [8] that icing at temperatures near the freezing point leads to higher aerodynamic penalties than icing at lower temperatures. Additionally, the transition between rime ice and glace ice takes place in a temperature region around −3 °C. Therefore temperatures around −40 °C do not offer much improvement to the field that can be studied in the icing wind tunnel. Additionally lower temperatures inside the icing wind tunnel lead to higher cooling requirements as more

parameter	value
speed at test section	$35\,\mathrm{m\,s^{-1}}$
chord length	0.4 m
maximum angle of attack	8°
width without boundary layer interference	0.3 m
air temperature	−15 °C

Table 4.1: List of the requirements for the icing wind tunnel.

heat has to be removed. Therefore, it was decided that the icing wind tunnel needs to guarantee temperatures of −15 °C but not lower.

All requirements for the icing wind tunnel are summarized in Table 4.1.

4.2 Thermophysical properties

The equations presented in the last chapter have to be used to receive the results that are presented in the following sections. These equations contain thermophysical properties of either air or water. These thermophysical properties depend on temperature. As the icing wind tunnel will operate with various temperatures, a choice for the reference temperature has to be made. To be conservative with every calculation, the worst case was chosen for every property. To do so, the maximum and minimum limit for both the air and the droplet temperature need to be known. The air will always be below the freezing point and as stated in Table 4.1 never lower than −15 °C. The droplets will leave the spray nozzle with a temperature of 15 °C. As the droplet temperature will adjust asymptotically to the air temperature, droplets can never get colder than −15 °C. With the known limits, the values of the thermophysical properties become the values summarized in Table 4.2. The density and the kinematic viscosity of air have different worst cases for the droplet behavior and the pressure loss calculations. Therefore for each of the two cases a different worst case was selected. All values for

property & symbol	value	T [°C]
thermophysical properties of air		
kinematic viscosity ν (Droplet behavior)	$12.11 \cdot 10^{-6}\,\mathrm{m^2\,s^{-1}}$	−15
kinematic viscosity ν (Pressure loss)	$13.38 \cdot 10^{-6}\,\mathrm{m^2\,s^{-1}}$	0
dynamic viscosity μ	$16.55 \cdot 10^{-6}\,\mathrm{kg\,s^{-1}\,m^{-1}}$	−15
heat capacity ratio γ	1.4	-
specific gas constant R	$287.0\,\mathrm{m^2\,s^{-2}\,K}$	-
Prandtl number Pr	0.7362	0
thermal conductivity k	$0.0225\,\mathrm{W\,m^{-1}\,K^{-1}}$	−15
density ρ (Droplet behavior)	$1.292\,\mathrm{kg\,m^{-3}}$	0
density ρ (Pressure loss)	$1.367\,\mathrm{kg\,m^{-3}}$	−15
thermophysical properties of water		
density ρ	$999.9\,\mathrm{kg\,m^{-3}}$	5
specific heat capacity c_p	$4349\,\mathrm{J\,kg^{-1}\,K^{-1}}$	−15
specific heat capacity c_v	$4349\,\mathrm{J\,kg^{-1}\,K^{-1}}$	−15
specific latent heat of fusion c_{latent}	$334{,}000\,\mathrm{J\,kg^{-1}}$	0

Table 4.2: Thermophysical properties of air and water for the reference temperature T. Different worst-cases might exist for the droplet behavior and the pressure loss.

air were taken by Çengel and Cimbala [52]. However, these authors just offer values for water for temperatures above the freezing point. Therefore their properties of water were compared with Hare and Sorensen [53], Stepanov [54] and Szedlak et al. [55]. In cases where the value was not given for the exact temperature, a linear interpolation between the two next closest values was done.

4.3 Final design

In this section, the final design of every single component is presented. During the design, the question about the necessary number of significant digits came up. The icing wind tunnel will have dimensions of multiple meters. Therefore, being more precise than rounding on centimeters seems not required.

4.3.1 Test section

Airfoils are essentially two-dimensional objects extracted in the spanwise direction. To have comparable conditions over the whole width it is therefore the easiest to have a rectangular shaped test section. With this decision, the space under and above the airfoil is the same inside the whole test section. Hence, both the test section and the airfoil are essentially two-dimensional. As explained in the previous chapter, the area of the test section must be chosen in a manner that the blockage stays below 10%. If an observer looks inside the test section from an upstream position, he will recognize both the airfoil and the test section as rectangular shapes with the same width. Therefore the equation for the blockage can be simplified to

$$\frac{A_{projected}}{A_{TS}} = \frac{H_{projected}W_{TS}}{H_{TS}W_{TS}} \approx \frac{H_{projected}}{H_{TS}}. \tag{4.1}$$

The area is denoted with A, the height with H, and the width with W. The index *projected* is used for the projected values of the airfoil and the index TS indicates the values of the test section. With equation 4.1 the blockage reduces to the fraction of two lengths. The projected height is the difference between the highest point of the airfoil and the lowest one. The coordinates of an airfoil depend on its shape, the chord length, and the angle of attack. The airfoil coordinates of an RG15 for an angle of attack of 0° are listed in Appendix A.3. The counter-clockwise rotation of a body can be formulated with

$$x' = x\cos(\theta) - y\sin(\theta) \tag{4.2a}$$

$$y' = x\sin(\theta) + y\cos(\theta) \tag{4.2b}$$

according to Kreyszig et al. [56]. The coordinates with an apostrophe denote the coordinates after rotation. With the equations 4.2a and 4.2b, the projected height of an RG15 airfoil with a chord length of 0.4 m under an angle of attack is 0.068 m. To ensure the blockage is 10% at most, the height of the test section hence needs to be 0.68 m.

As explained in section 4.1, a width of 0.3 m without any boundary layer interaction is required. According to the rule of thumb by Barlow et al. [20], that was presented in the previous chapter, the boundary layer will influence 20% of the width and height. Therefore the test section width would have to be increased by 25%. This results in a safety margin of about 0.038 m on each side. More detailed simulations with the method presented in the previous chapter however lead to a boundary layer height of 0.043 m at the test section. Therefore at least 0.086 m have to be added to the airfoil width to avoid boundary layer interactions. To introduce a small safety margin, a test section width of 0.39 m was chosen.

Hence, the test section is rectangular with a width of 0.39 m and a height of 0.68 m. This results in a hydraulic diameter of 0.50 m.

As mentioned, the flow should be allowed a settling length of half the hydraulic diameter of the test section between the nozzle exit and the test object. Therefore, for the stated design, the settling length is 0.25 m. Additionally, for this design, it was chosen to increase the test section length by 0.05 m behind the test object. This reduces the probability of separation on the transition of the test section and the diffuser and allows to insert longer airfoils as well. Hence, the length of the test section is calculated by adding up the settling length, the considered chord length of 0.4 m, and the enlargement of 0.05 m. This sum is also visualized in Figure 4.4. Therefore the final length of the test section is 0.70 m. The final design of the test section is shown in Figure 4.4.

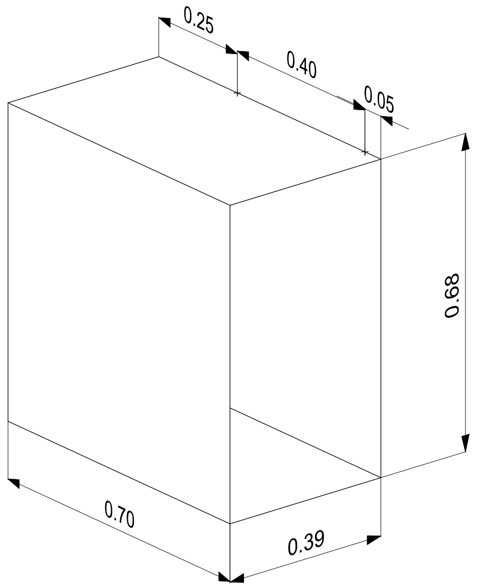

Figure 4.4: Final design of the test section.

4.3.2 Nozzle

The downstream end of the nozzle connects to the test section. Therefore the cross-section of the downstream end of the nozzle is the same as the test section's cross-section. Hence, at this end, the nozzle has a rectangular shape with a width of 0.39 m and a height of 0.68 m.

For this work, a medium contraction ratio of 9 was chosen. This should offer a balance between good flow quality and few pressure losses on one side and a small wind tunnel size on the other side. With the contraction ratio that is effectively the area ratio, also the cross-sectional area of the upstream end is given, but the cross-section can still be determined. Upstream of the nozzle, the settling area, the wide-angle diffuser and the fan will be mounted. As will be explained in subsection 4.3.5, the fan of this wind tunnel will be circular. The test section however has a rectangular cross-section with an aspect ratio of almost 2:1. Therefore, the cross-section must change somewhere from circular to rectangular between the fan and the test section. As explained in the last chapter, rectangular nozzles with a changing aspect ratio are an option. A change of cross-section from circular to rectangular or square is however introducing new problems. This is because the nozzle itself is designed with a narrow margin to separation and changes of the cross-section between circular and rectangular have the same downside.

Having a square cross-section at the upstream end makes the transition to a circular shape further upstream easier. Additionally, the maximum opening angle of the nozzle with changing aspect ratio is smaller compared to keeping the aspect ratio. As separation depends on the opening angle and the maximum opening angle of the nozzle is reduced, the separation risk is reduced. Hence, the upstream end of the nozzle was chosen to be square. As both the area at the downstream end and the area ratio are given, the side length of the square can be calculated to 1.54 m.

In Figure A.1 in the Appendix, the minimum length of nozzles is plotted over the ratio of the equivalent diameters at inlet and outlet. For an area ratio of 9, the ratio of the equivalent diameters becomes 3. According to the stated figure, the length of the nozzle should be at least 0.9 times the equivalent diameter at the inlet for this case. As short nozzles have a higher risk of separation and long nozzles increase the wind tunnel length, a compromise needs to be found. Therefore, a length of exactly the equivalent diameter of the upstream end was chosen. The equivalent diameter of a square with sides of 1.54 m is 1.74 m. Hence, the length of the nozzle is 1.74 m. The design of the nozzle is visualized in Figure 4.10.

With the inlet and outlet geometry given as well as the length of the nozzle, the last question is the shape of the nozzle walls. A closer look at the contours presented in subsection 3.2.2 shows that the shapes of the third-order polynomial, the fifth-order polynomial, and the transformed fifth-order polynomial are steeper near the entry of the test section than the AVA nozzle, the Witoszynski nozzle, and the matched cubics nozzle contours. Figure 4.5 shows the trajectories of droplets with 50 µm droplet diameter for a nozzle shape based on a third-order polynomial. When the droplets reach the test section, they still have a significant velocity normal to the wind tunnel direction. This is due to their character to follow the air streamlines to a certain degree. Due to the steep contraction at the end of the nozzle, also the streamlines of the air have a steep contraction. Hence, the droplets receive a huge velocity normal to the wind tunnel direction to be able to follow the air streamlines. The velocity component normal to the wind tunnel direction changes the effective angle of attack for the airfoil and therefore decreases the quality of the measurements and results.

As a comparison, the trajectories of droplets with 50 µm inside the AVA nozzle are shown in Figure 4.6. As the gradient of the nozzle contour close to the test section is

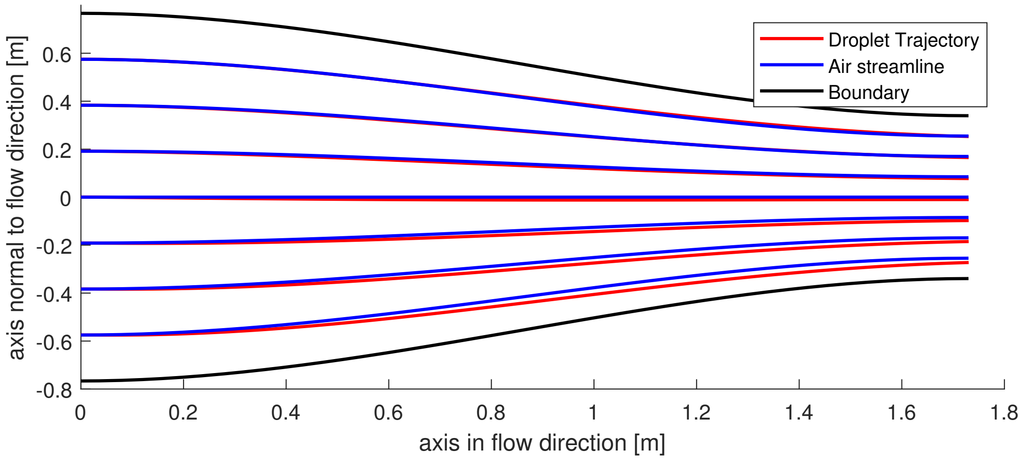

Figure 4.5: Trajetories of droplets with 50 µm diameter in a nozzle with a third order polynomial contour.

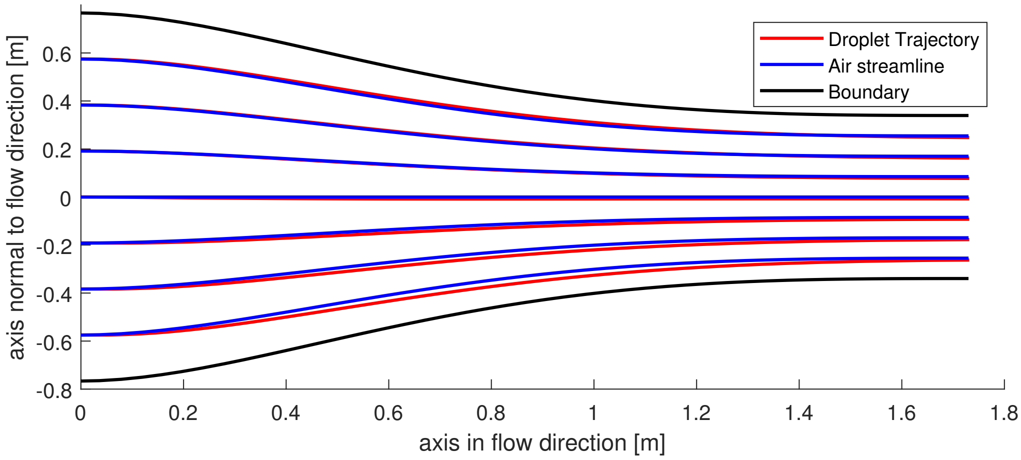

Figure 4.6: Trajetories of droplets with 50 µm diameter in a nozzle with an AVA contour.

small, the droplets have a much smaller velocity component in the upwards direction. Therefore the nozzle contours that are less steep in their final part are preferable for the concern of the trajectories.

A plot of the development of the velocities of the droplets through the nozzle can be rather difficult to understand. This is because the velocity of the droplets adjusts to the air speed. However, if different nozzle contours are compared, the air speed of the different nozzle contours is different at every position. Therefore, Figure 4.7 contains an exemplary plot of the droplet velocity through the AVA nozzle as well as the air speed and the nozzle contour. It can be seen that the droplets leave the spray nozzle with a velocity higher than the air speed. They are however decelerated in the settling area and have almost the same velocity as the air at the beginning of the nozzle. Due to the contraction of the nozzle, the air speed increases and the droplet velocity adjusts slowly to this changed air speed. The droplets are however not able to reach the air speed until they reach the test object.

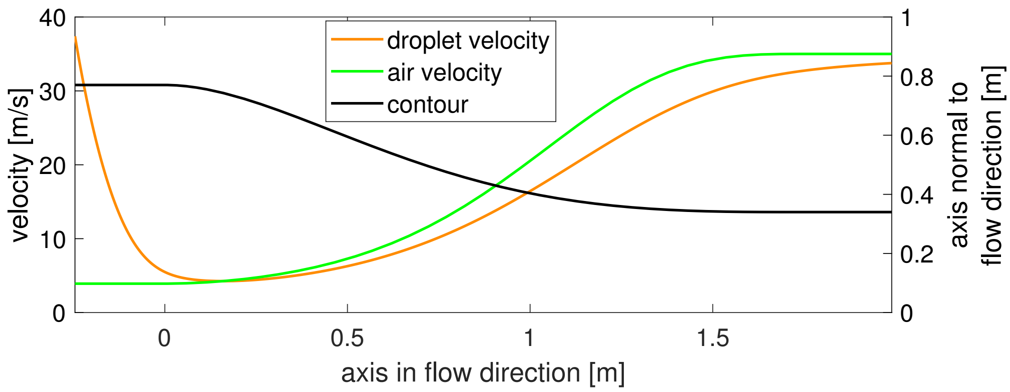

Figure 4.7: Comparison of the droplet and the air velocity inside the AVA nozzle.

Figure 4.8 shows the development of the droplet velocity over the length between the spray nozzle and the test object for different nozzle contours. The simulated droplet diameter was 75 µm. The large droplet diameter was chosen to highlight the differences in the plots. The air velocity at the end of the nozzle is $35\,\mathrm{m\,s^{-1}}$. Figure 4.8 shows that the droplets come closer to the target velocity in the nozzles that are steep in a more upstream position. Because of the contraction, the air velocity is increased and the velocity difference between droplet and air as well. According to the equation of motion 3.15, the change in the droplet's velocity is proportional to the difference between air velocity and droplet velocity. A higher velocity difference from the start of the nozzle therefore leads to a stronger acceleration of the droplet and higher final velocities. If the nozzle contraction occurs further downstream, the largest velocity difference occurs just there. Therefore, the time for the droplets to adjust their velocity is much less. Hence,

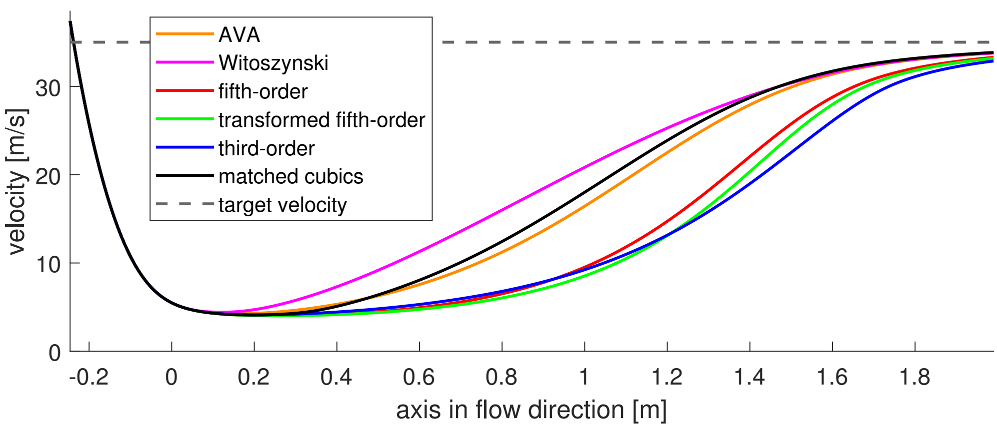

Figure 4.8: Comparison of the development of the droplet velocity for different nozzle contours.

it is preferable to have a nozzle with an earlier point of strong contraction to increase the droplet's velocity.

The development of the droplet temperature over the length between the spray nozzle and the test object for different nozzles is shown in Figure 4.9(a). To highlight the differences between different nozzle contours, a zoom was chosen for the final part of the nozzle. The zoom can be seen in Figure 4.9(b). The parameters for the calculation are the same as for Figure 4.8. The droplets start with a temperature of 288.15 K and an air temperature of 270.15 K. The temperature development is different from the velocity development. Nozzles with a strong contraction further upstream result in higher droplet temperatures at the position of the test object. This is because a strong contraction upstream leads to higher velocities there and the droplets therefore reach the test object sooner. Hence, the droplets have less time to adjust their temperature. Therefore nozzles with a later point of strong contraction are better to achieve specified temperatures of the droplets.

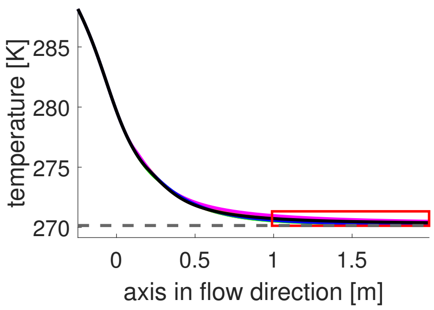

(a) Droplet temperature over the full nozzle length.

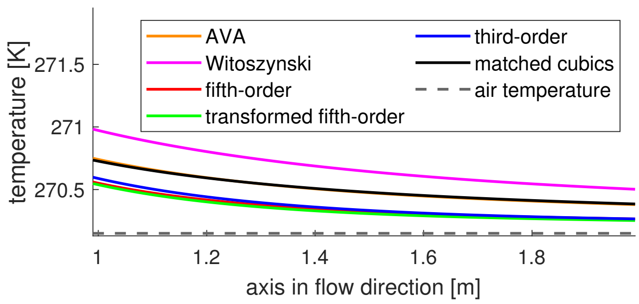

(b) Droplet temperature over the zoomed section.

Figure 4.9: Comparison of the development of the droplet temperature for different nozzle contours.

The final decision for the nozzle design was driven by the droplet velocity development, the droplet temperature development, and the droplet trajectories. A perfect nozzle can not be found. This is because nozzles with a strong contraction further upstream have a smaller deviation in the final velocity, but a higher deviation in the final temperature. Therefore, a compromise has to be found. Nozzles that are steeper towards the nozzle's end also change the effective angle under which the droplets hit the test object. Therefore it was decided that the third-order polynomial, the fifth-order polynomial, and the transformed fifth-order polynomial are not the best options. The differences between the three remaining nozzles are rather small. As the temperature plays a more important role for the icing results than the velocity, the AVA nozzle was chosen. This is because out of the remaining nozzles, the AVA nozzle leads to the droplets reaching the target temperature the closest.

Equation 3.1 was created for nozzles with a square or round cross-section. As the nozzle will be rectangular in this work, now two equations are needed: one for the upper and lower part and one for the sides. A look at the equation shows that just the area

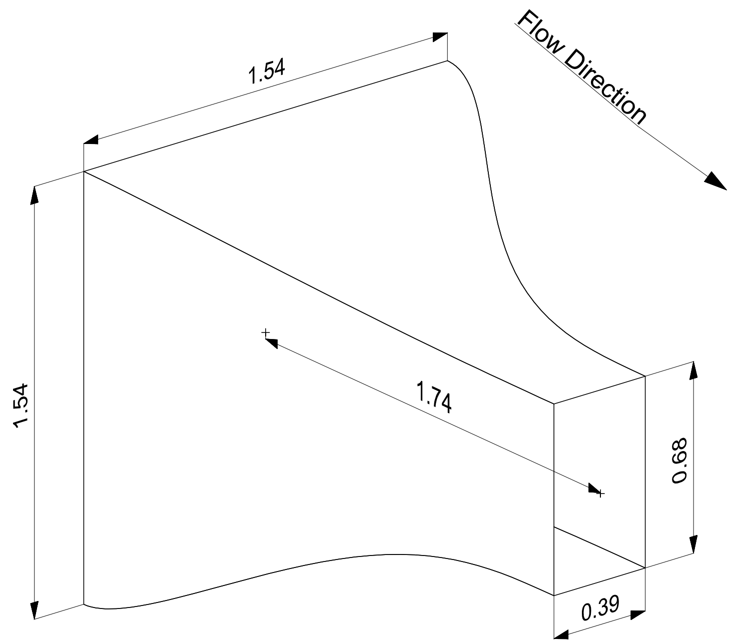

Figure 4.10: Final design of the nozzle.

ratio can be changed. To calculate the contours correctly, an equivalent area ratio is calculated. To do this, the height/width at the test section is divided by the value at the nozzle entry and this value is squared.

As explained earlier, the position of the steepest slope should be the same for every side. The only difference between the contour equations is the area ratio. As the area ratio is just a constant, it does not change the position of the steepest slope at all. Therefore no further action needs to be taken to match the positions of the steepest slopes. The final design of the nozzle is shown in Figure 4.10

4.3.3 Settling area

The settling area is upstream of the nozzle and does not change its shape over its length. Therefore it has the same shape as the upstream end of the nozzle. Hence, the settling area is square with the length of the sides being 1.54 m. This results in a hydraulic diameter of 1.54 m as well.

The spray system is the component placed the most downstream inside the settling area. Otherwise, the droplets would hit the honeycombs and screens. This would lead to ice accretion on these components. As a result, the flow quality and uniformity would suffer severely. Hence, the honeycombs and screens have to be placed upstream of the spray nozzles.

4.3.3.1 Spray System

The spray system is of huge importance. The system must be able to inject droplets with the wanted MVDs that are small compared to many other droplet operations. Additionally, the LWC must also match the values that need to be tested according to the certification regulations. Furthermore, those values need to be controllable exactly to do experiments with exactly known boundary conditions. Another important requirement for the spray system is that the droplet distribution in the test section has to be very close to uniform. Otherwise, the local conditions would be different in MVD and LWC compared to the global values. This would lead to experimental results that do not match the reality.

Selecting a suitable spray system is a difficult topic. This is due to two reasons. First, most manufacturers of spray nozzles and spray systems do not offer all necessary information on their products openly. Especially the droplet diameters that can be obtained with a spray nozzle are typically not given but of significance for this work. Additionally, turbulence enhances the mixing in an air flow significantly and therefore also the spreading of droplets. With the basic equation of motions used in this thesis, the turbulence can not be taken into account. Therefore, calculating the spreading of the droplets is not possible in the scope of this work. Hence, the selection of a spray system can not be done in this thesis and will be a topic for the future.

Nevertheless, some recommendations for suitable spray systems shall be presented. The droplets in the wind tunnel will be smaller than for most other experiments. To achieve small droplet sizes, typically air-assisted atomizers are used. In these spray nozzles, the water jet is broken into small droplets because of the shear stresses between an air flow and the water jet. For example Bansmer et al. [31], Tiihonen et al. [26], and Leone et al. [57] used air-assisted atomizers in their icing wind tunnels. The second point is that the LWC is low for this designed icing wind tunnel. Therefore, spray systems with low water flux are needed. A possibility is the use of pulsating spray nozzles as done by Bansmer et al. [31]. These nozzles are not injecting the water continuously but intermittently. With this technique, lower water fluxes can realized.

The question of the number of spray nozzles needs to be calculated carefully. Giving hints is however difficult, because existing icing wind tunnels differ significantly in their number of spray nozzles. The Braunschweig icing wind tunnel described by Bansmer et al. [31] is comparable in test section size and air speed to the designed icing wind tunnel and uses 25 spray nozzles. The VTT icing wind tunnel described by Tiihonen et al. [26], however, is slightly larger and has a comparable air speed, but only uses 9 spray nozzles. Therefore, these configurations can be used as a first idea for the final spray system design, but an analysis needs to be done before the final selection.

An initial droplet velocity needs to be known to calculate the droplet behavior. Some examples for pulsating air-assisted atomizers are given by Spraying Systems Co. [58]. These nozzles operate with pressures between 0.34 bar and 7 bar. Because a part of the pressure energy is also needed to brake the water jet into small droplets, a pressure of 3.5 bar is used to calculate the initial droplet velocity. As stated by Spraying Systems Co. [59], the orifice for air and liquid are the same for the systems of interest. Additionally, the pressures are often comparable for the air and the water. Therefore, an assumption is made that the volumetric flow of air and water is the same. Hence, the density of the mixture is the average of the density of air and the density of water. Using equation 3.16, this results in a initial droplet velocity of about $37.5\,\mathrm{m\,s^{-1}}$.

4.3.3.2 Turbulence Screens

Upstream of the spray nozzles, one or more turbulence screens are placed. Multiple screens will increase the flow quality but at the expense of higher pressure losses and a longer wind tunnel. Therefore, for this design, only one screen was chosen. As stated before, the porosity should be between 0.57 and 0.8. Higher values of the porosity lead to fewer pressure losses. At the same time, higher porosities also lead to less balancing of the nonuniformities of the flow. Therefore a balance needs to be found. As will be shown in 4.5, the pressure loss of the screen has just a minor influence on the total pressure losses. Therefore a low value of porosity of 0.6 was chosen to increase the uniformity of the flow on the expense of slightly higher pressure losses.

4.3.3.3 Honeycombs

The most upstream components inside the settling area are the honeycombs. As stated in the previous chapter, the ratio of the length to the diameter of the honeycombs should be between 6 and 8. Larger values lead to a higher quality of the flow. Therefore the designed honeycombs do have a ratio of the length to the diameter of 8. Following the recommendation of Barlow et al. [20], there should be 150 cells per diameter of the settling area. As the hydraulic diameter of the settling area is 1.54 m, the hydraulic diameter of the honeycombs is 0.01 m. Therefore the length of the honeycombs is 0.08 m.

4.3.3.4 Assembly

As mentioned in the previous chapter, the distance between screens and also between the last screen and the nozzle exit should be 0.2 times the hydraulic diameter of the settling area. By doing this, the non-uniformities of the flow can be reduced. The spray system is no screen but will be handled like a screen concerning this matter. Therefore between the three components inside the settling area and after the spray system should be a spacing of 0.2 times the hydraulic diameter each. No typical rule is given for the distance between the nozzle entry and the honeycombs. For most conventional wind tunnel designs with just one honeycomb section and one screen, typically 0.5 times the hydraulic diameter is used as the total length of the settling area. Therefore these wind tunnels would have a distance of 0.1 times the hydraulic diameter between the beginning of the settling area and the honeycombs. This distance shall also be included in this design. To still be able to insert the spray system, an extra length of one-tenth of the hydraulic diameter is inserted. Hence, the overall length of the settling area is 0.8 times the hydraulic diameter of 1.54 m. This results in a total length of the settling area of 1.23 m. The final design of the settling area is shown in Figure 4.11.

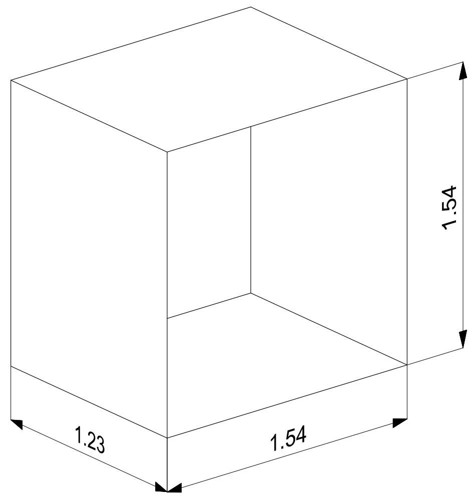

Figure 4.11: Final design of the settling area.

4.3.4 Wide-angle diffuser

The wide-angle diffuser is the connection of the fan section and the settling area. Hence, the downstream end of the wide-angle diffuser has the same shape as the settling area. Therefore the downstream end of the diffuser is square with a length of the sides of 1.54 m. The size of the fan section needs to be known for the design of the upstream end of the wide-angle diffuser. At the same time, the wide-angle diffuser can have a big pressure loss and hence change the dimensions of the needed fan. Therefore it is an iterative process to design the wide-angle diffuser and select a fan.

Smaller area ratios over the wide-angle diffuser lead to a shorter component and fewer pressure losses. However, this leads to bigger fans. Bigger fans need more space and typically cost more. As a compromise, an area ratio of about 2.5 and a fan diameter of about 1.1 m were chosen. As will be presented in section 4.5, in the end, a fan with a diameter of 1.09 m was chosen as well as an area ratio of 2.55.

As already mentioned, the cross-section at the downstream end is the same as the cross-section of the settling area. The cross-section at the upstream end is the cross-section of the fan. Therefore the wide-angle diffuser is circular at the upstream end and square at the downstream end. The cross-section will change over the length of the wide-angle diffuser.

To keep the diffuser as short as possible, an opening angle of 60° was chosen. The length of the wide-angle diffuser is then 0.56 m. To be able to prevent separation despite this high angle, one of the options presented in Subsection 3.2.4 has to be chosen. Screens are the easiest option to design and operate because they are passive components. Therefore the wide-angle diffuser will contain screens. Figure A.2 lists the number of screens necessary for different configurations of wide-angle diffusers. For an area ratio of 2.5 and an opening angle of 60°, two screens are necessary to prevent separation inside the wide-angle diffuser. As explained in the previous chapter, the first screen should probably be placed near the nozzle entry and the second screen somewhere in the

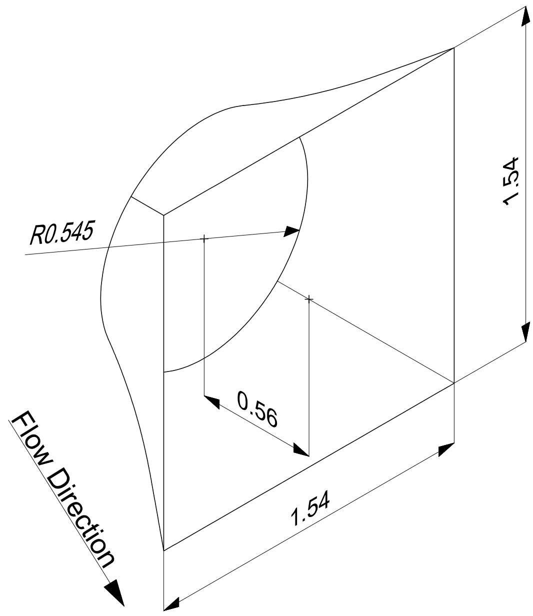

Figure 4.12: Final design of the wide-angle diffuser.

middle of the wide-angle diffuser. The final design of the wide-angle diffuser is shown in Figure 4.12.

4.3.5 Fan

The fan is placed as the most upstream part of the wind tunnel. As mentioned, the design was developed in an iterative process together with the wide-angle diffuser. However, already before this iterations, a decision about the type of fan section had to be made. As explained in subsection 3.2.5, centrifugal blowers might have a small advantage over axial fans, but it is not undisputed. Centrifugal blowers do however have the disadvantage of needing much more space than axial fans. Therefore axial fans are favored over centrifugal blowers. While the use of multiple fans might have some advantages, the uncertainty about the flow quality and flow uniformity lead to the decision for a single axial fan. The final effects of the necessary change of cross-section on the flow are not clear. However, the change of cross-section might even reduce the separation risk inside the nozzle as explained in 4.3.2. Therefore a single axial fan was chosen for the design of this wind tunnel.

While the choice of a specific fan will be explained in section 4.5, the size of the fan duct will already be named here. The term fan duct is used for the combination of the fan itself and a short section with the same cross-section behind. This short section is beneficial for the flow conditions and will have a length of 0.1 m. Therefore the fan duct has a diameter of 1.09 m and a length of 1.01 m.

4.3.6 Diffuser

The diffuser is the component connected downstream of the test section. Therefore the diffuser has a rectangular inlet with a width of 0.39 m and a height of 0.68 m. The design of the diffuser itself is a weighing between length and pressure losses. For this thesis, a compromise was chosen with an area ratio of 2.5. To keep the length short nevertheless, a rather high opening angle of 3° was chosen. As the diffuser inlet is rectangular, two possible diffuser designs were considered. The diffuser could either keep the aspect ratio over its length or have the same opening angle at every side. The diffuser is prone to flow separation. Assuming that the problem of flow separation is about the opening angle itself and not about the aspect ratio, all sides are designed to have the same opening angle. Otherwise, two sides would have a higher opening angle than 3° and the other two a lower one. The chosen design with the same opening angle on every side results in a width of 0.68 m and a height of 0.97 m at the exit of the diffuser. The length of the diffuser is 2.79 m. The final design is shown in Figure 4.13.

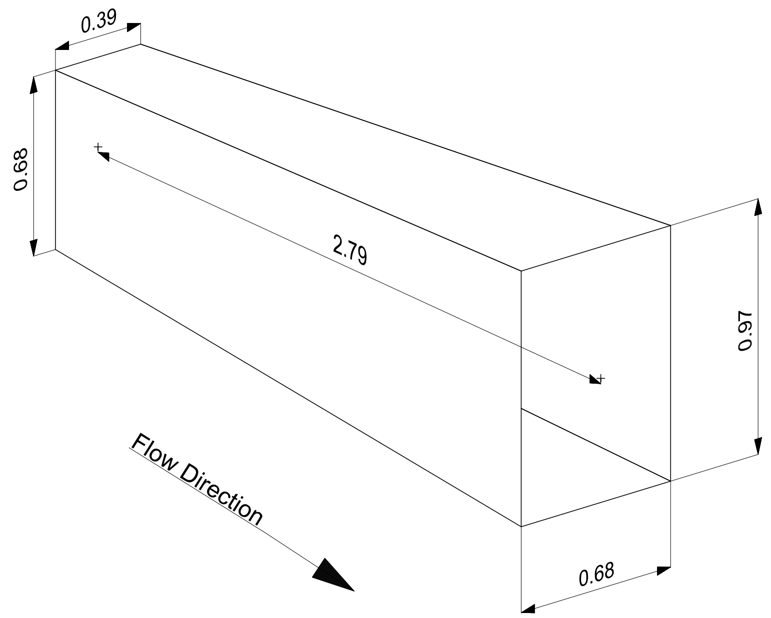

Figure 4.13: Final design of the diffuser.

4.3.7 The final design

With the design of the single components presented so far, the icing wind tunnel would have an overall length of 8.03 m. The maximum width and height of the icing wind tunnel would be the values of the flow conditioning duct and therefore 1.54 m. All dimensions are summarized in Table 4.3.

The complete icing wind tunnel with all components is shown in Figure 4.14.

Component	Length[m]	Dimensions[m]	
		Inlet	Outlet
fan duct	1.01	1.09	1.09
wide-angle diffuser	0.56	1.09	1.54 x 1.54 (1.54)
settling area	1.23	1.54 x 1.54 (1.54)	1.54 x 1.54 (1.54)
nozzle	1.74	1.54 x 1.54 (1.54)	0.39 x 0.68 (0.50)
test section	0.70	0.39 x 0.68 (0.50)	0.39 x 0.68 (0.50)
diffuser	2.79	0.39 x 0.68 (0.50)	0.68 x 0.97 (0.80)
wind tunnel	8.03	max 1.54 x 1.54 (1.54)	

Table 4.3: Dimensions of the final icing wind tunnel components. Two values are given in the dimensions column if the section is rectangular, one value if the section is round. If the section is rectangular, also the hydraulic diameter is given in brackets.

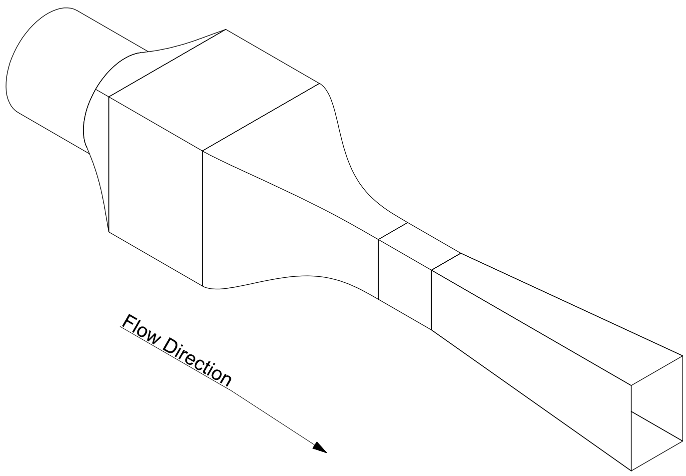

Figure 4.14: The final wind tunnel.

4.4 Droplet behavior in the icing wind tunnel

The design to this point was mostly about aerodynamic issues and not about the thermodynamics and the droplet behavior. However, as the purpose of the icing wind tunnel is to do icing experiments, the droplet behavior needs to be checked. As presented in section 3.3, droplets with a larger diameter and therefore higher mass will adjust more slowly than smaller droplets. Additionally, the droplets adjust to the speed and temperature of the air asymptotically. Therefore the droplets will never reach the temperature and velocity of the air exactly. However, a longer distance between the spray system and the test object reduces the differences between droplet and air values. An important characteristic of the icing wind tunnel will be the maximum MVD that can be tested inside the icing wind tunnel according to the requirements. Therefore, a maximum for the final deviation between air and droplet values has to be chosen.

As explained in the previous chapter, the Reynolds number has a significant influence on the ice accretions. Hence, to have a good transferability of the results of the experiments, the velocity of the droplets needs to be close to the target value. Therefore it was decided that the final deviation of the droplet speed has to be at most $2\,\mathrm{m\,s^{-1}}$ in case of the design speed of $35\,\mathrm{m\,s^{-1}}$.

Calculations with an air velocity of $35\,\mathrm{m\,s^{-1}}$ at the test section were done. The final velocity deviations for different droplet sizes are shown in Figure 4.15. According to the figure, droplets with a maximum diameter of about $95\,\mu\mathrm{m}$ can be tested without having a higher deviation than $2\,\mathrm{m\,s^{-1}}$ from the air velocity. Using the Langmuir D distribution, this results in a maximum MVD of about $42\,\mu\mathrm{m}$ that can be tested in the icing wind tunnel and still adjust fast enough to the air velocity.

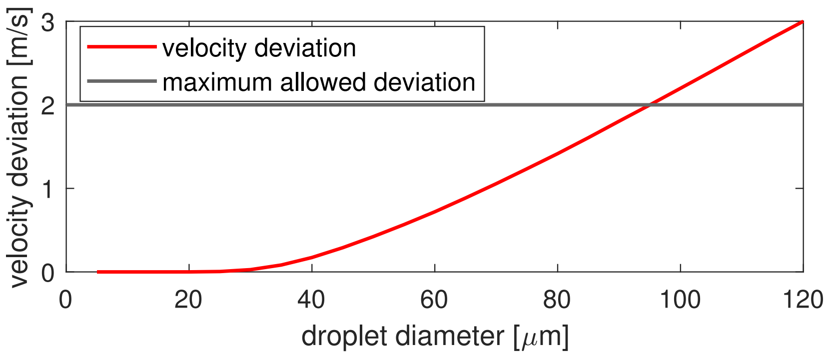

Figure 4.15: Velocity deviation for different droplet diameters.

Regarding the temperature, the region around $-3\,^\circ\mathrm{C}$ and $-2\,^\circ\mathrm{C}$ is the most important to be achieved exactly. This is because the type of ice accretions changes from rime to glaze ice in this temperature region. To have good control over the type of the ice shape, the droplet's temperature at the test object shall differ at most $0.5\,^\circ\mathrm{C}$ from an air temperature of $-3\,^\circ\mathrm{C}$.

To find out which MVDs can be tested in the icing wind tunnel, calculations with different droplet sizes were done. As higher velocities decrease the temperature change, the worst case was chosen. Therefore the air velocity at the test section is $35\,\mathrm{m\,s^{-1}}$ for the calculations. As the necessary adaption quality was decided for an air temperature of $-3\,^\circ\mathrm{C}$, the air temperature was set to $-3\,^\circ\mathrm{C}$. The final temperature deviations for different droplet sizes are presented in Figure 4.16. To remain inside a difference of $0.5\,^\circ\mathrm{C}$ to the air temperature, droplets with a maximum diameter of about $85\,\mu\mathrm{m}$ can be tested. Using the Langmuir D distribution, this results in a maximum MVD of about $38\,\mu\mathrm{m}$ that can be tested in the icing wind tunnel and still adjust fast enough to the air temperature.

Therefore droplets with MVDs of $38\,\mu\mathrm{m}$ are the biggest droplets to be tested inside the designed icing wind tunnel and still fulfill every requirement.

If a design is wanted that works for higher MVDs, the length between the spray system and the test object needs to be enlarged. On the contrary, the length can be shorter if

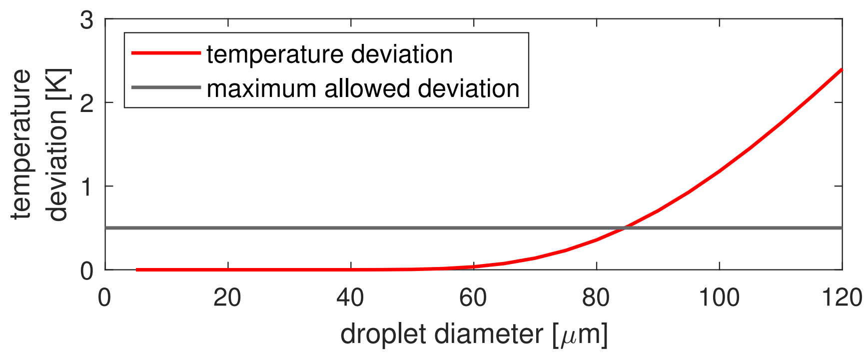

Figure 4.16: Temperature deviation for different droplet diameters.

the icing wind tunnel shall be designed for smaller droplets. One option to change the length of the droplets' trajectories is to just change the nozzle length. Figure 4.17 shows the length the nozzle would need to have for different diameters to achieve the droplet temperature and velocity as formulated in the requirements. It is however important to state that much shorter nozzle lengths increase the risk of separation drastically. For droplets with a diameter of 35 μm or less, the length of the nozzle can be as short as 0.05 m because the lengths between the spray system and nozzle entry and between the test section entry and the test object are already long enough.

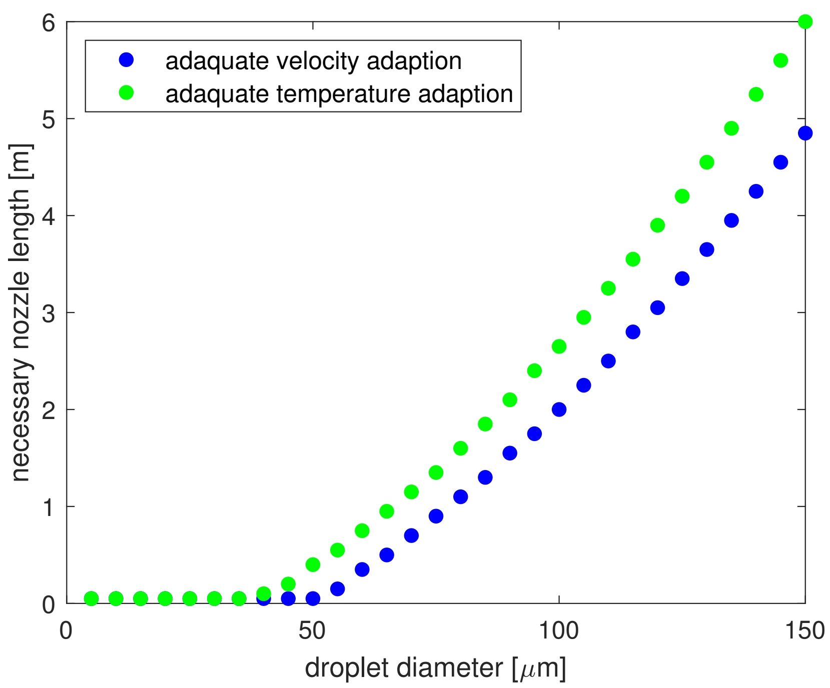

Figure 4.17: Necessary length of the nozzle to fulfill the requirements for different droplet diameters.

The maximum MVD in the EASA certifications is 50 μm. According to the Langmuir D distribution, the biggest droplets in such a droplet cloud have a diameter of about 110 μm. The necessary nozzle length to do experiments with droplets with a diameter of 110 μm is 3.25 m according to Figure 4.17. Therefore a nozzle with a length of 3.25 m is needed to test the whole bandwidth of the EASA certifications.

4.5 Pressure losses and fan selection

As presented in the previous chapter, every component of the icing wind tunnel influences the pressure loss. The values necessary to calculate the pressure loss of each component are already given in the respective subsection. The remaining values will be introduced and explained in this subsection.

For the calculation of the friction coefficient according to equation 3.30 the Reynolds number is needed. The Reynolds number is calculated with equation 2.1. As the hydraulic diameter of every component is given in the respective subsection and the viscosity in Table 4.2, just the air velocity is missing. The velocity can be calculated with the continuity equation. The velocities at the inlet and the exit of the different parts of the icing wind tunnel are summarized in Table 4.4. As higher velocities inside the icing wind tunnel lead to higher pressure losses, the maximum velocity of 35 $\mathrm{m\,s^{-1}}$ inside the test section was used as the design point.

component	inlet velocity [$\mathrm{m\,s^{-1}}$]	exit velocity [$\mathrm{m\,s^{-1}}$]
fan duct	9.95	9.95
wide-angle-diffuser	9.95	3.89
settling area	3.89	3.89
nozzle	3.89	35.00
test section	35.00	35.00
diffuser	35.00	14.00

Table 4.4: Velocities at the inlet and outlet of every component.

When calculating the pressure loss due to the drag of a structure inside the icing wind tunnel with equation 3.47, the value ϵ is needed. This value accounts for the influence the structure has on the pressure loss in downstream sections. The two structures inside the icing wind tunnel are the spray system and the test object. As both are designed with an aerodynamic shape, the downstream influence is supposed to be negligible. Therefore ϵ is assumed to be the minimum possible value of 1.

The test object itself produces drag. This drag results in a pressure loss that can be calculated with the equation for internal structures. To calculate the pressure loss, the drag coefficient is needed. The drag coefficient is higher for lower Reynolds numbers. According to Figures 4.1 and 4.2, the lowest Reynolds numbers for UAVs will be for velocities of around 10 $\mathrm{m\,s^{-1}}$ and chord lengths of 0.1 m. This would result in a Reynolds number of about 80,000. The drag coefficient of the RG15 airfoil for various Reynolds numbers is listed by Airfoil Tools [50]. As no values are given for a Reynolds number of

80,000, the drag coefficient will be taken for a Reynolds number of 50,000. The highest drag coefficient for a Reynolds number of 50,000 inside the linear region of the c_L-α-curve is 0.039. The remaining unknown is the ratio of the area of the drag item to the flow area. The drag area of an airfoil is its chord length times the width. The flow area is the part of the cross-sectional area that is not blocked. As the blockage will be 10% maximum, the flow area is 90% of the cross-sectional area of the test section.

The spray system also produces drag and therefore a pressure loss. The shape of the spray system should be one with a small drag coefficient to reduce the pressure losses and the aerodynamic losses. However, as no spray system could be selected, also the shape of the spray system is not yet determined. To not underestimate the pressure loss of the spray system, the worst case was calculated. To do this, the shape of the spray system is simplified to a circular pipe in crossflow. Therefore the drag coefficient becomes 1. For the blockage of a spray system, a maximum of 17% is recommended by Leone et al. [57]. The drag area of the spray system is its projected area and therefore maximum 17% of the cross-sectional area, while the flow area is the remaining 83% of the cross-sectional area.

The pressure loss calculation of the screen contains the parameter K_{Re}. For the calculation of the Reynolds number the diameter of the screen wire needs to be known. The diameter of the wire was assumed to be 0.5 mm as was also done by Arifuzzaman and Mashud [22]. Additionally, the mesh constant K_{MESH} needs to be fixed to calculate the losses. The value for average circular metal wires was used and therefore K_{MESH} becomes 1.3. The missing ratio of the flow area to the cross-sectional area is equivalent to the porosity of the screen.

The friction coefficient of the honeycombs depends on the surface roughness of the honeycombs. As done by Arifuzzaman and Mashud [22], polyvinyl chloride (PVC) can be used for the construction of the honeycombs. Measurements by Rocha et al. [60] showed that the surface roughness of PVC can be as high as $8\,\mu$m.

For the calculation of the pressure loss inside the diffuser, the value K_{EXP} needs to be known. The value was calculated with the equation for square cross-sections. This is because a square is closer to a rectangular shape than a circle and because this leads to a more conservative calculation.

For the calculation of the exit losses, the Mach number at the exit needs to be calculated. It is assumed that the temperature of the air stays constant inside the whole icing wind tunnel. The Mach number and therefore also the pressure losses are higher for lower temperatures. Therefore the worst-case temperature of $-15\,°$C was chosen.

The resulting pressure losses for every component and the icing wind tunnel in total are stated in Table 4.5. Also the number of the equation that was used to calculate the pressure loss is given in this table.

To compensate for possible shortcomings in the calculations, a safety margin is introduced. It was chosen that the selected fan has to be able to compensate about 1.5 times the calculated pressure losses. This results in a pressure rise of about 500 Pa the fan has to deliver. A further objective for the fan was to have a diameter of about 1.1 m to have an area ratio of about 2.5 over the wide-angle diffuser. The third point is the volume flux through the fan. A maximum volume flux of $9.28\,\mathrm{m^3\,s^{-1}}$ can be calculated with equation 3.8.

component	equation	K	pressure loss [Pa]
test section	3.28	0.016	13.40
test object	3.47	0.025	20.93
nozzle	3.31	0.014	11.72
settling area	3.28	0.011	0.11
spray system	3.47	0.205	2.12
screen	3.48	1.210	12.51
honeycombs	3.44	0.404	4.18
wide-angle-diffuser	3.51	1.360	91.41
fan duct	3.28	0.011	0.74
diffuser	3.32	0.057	47.73
exit losses	3.43	1.000	133.97
total losses			338.82

Table 4.5: Overview over the pressure losses in every component and in total.

The selected fan is the model 43W726 by Aerovent [61]. It has a diameter of 1.09 m and a length of 0.91 m. The fan is able to deliver a pressure rise of about 500 Pa for a volume flow of $11.0\,\mathrm{m^3\,s^{-1}}$. Therefore the fan is perfectly able to fulfill the requirements. The input power of this fan in the viewed mode is 8.024 kW. This parameter is important to be considered for the necessary cooling power of the cooling chamber.

4.6 Cooling chamber

4.6.1 Cooling requirements

The necessary equations for the calculation of heat released during the run of the icing wind tunnel were given in the previous chapter. The required cooling power depends on the water content in the air and on the difference between the initial droplet temperature and the air temperature. The worst case is assumed for both parameters. Therefore a LWC of $2.9\,\mathrm{g\,m^{-3}}$ and an air temperature of $-15\,°\mathrm{C}$ are used.

As already mentioned, the initial droplet temperature is assumed to be 15 °C. Therefore the maximum temperature difference is 30 °C. With a maximum LWC of about $2.9\,\mathrm{g\,m^{-3}}$ and the maximum air mass flow of $9.150\,\mathrm{m^3\,s^{-1}}$, the maximum mass flow of the water is $0.0269\,\mathrm{kg\,s^{-1}}$. This would result in a sensible heat of 3.510 kW and a latent heat of 8.985 kW. Combined with the fan input power of 8.024 kW, the produced heat adds up to 20.520 kW. This is the maximum amount of heat the cooling chamber has to remove to ensure a steady run.

A typical temperature for the air inside the icing wind tunnel will be around $-10\,°\mathrm{C}$. The resulting heat for different LWCs is plotted in Figure 4.18. According to the regulations by the EASA, the maximum LWC for a temperature of $-10\,°\mathrm{C}$ is $2.5\,\mathrm{g\,m^{-3}}$. Therefore higher LWCs do not need to be tested in an icing wind tunnel.

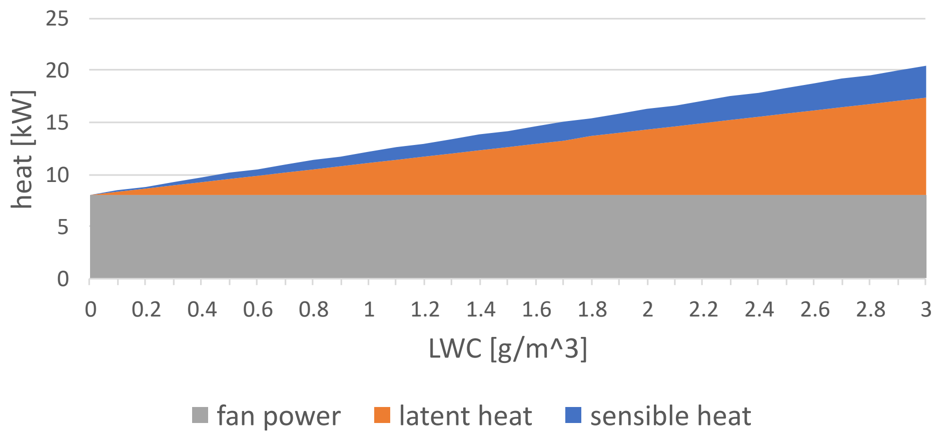

Figure 4.18: Required cooling power for the icing wind tunnel for different LWCs and an air temperature of $-10\,°C$.

4.6.2 Space requirements

As mentioned in the previous chapter, Greenway and Wood [46] did simulations for a single wind tunnel design to calculate the necessary clearance at the wind tunnel inlet. They found out that the inflow area has to be at least 1.8 times bigger than the inlet area. For the given design, the inlet is at the fan section. The fan area is $0.93\,m^2$. Therefore the area of the inflow has to be at least $1.67\,m^2$. Figure 4.19 shows different combinations of side lengths of possible chambers and lengths between the inlet and the wall. As the icing wind tunnel is 1.54 m wide and high at its biggest position, smaller chambers are not possible at all.

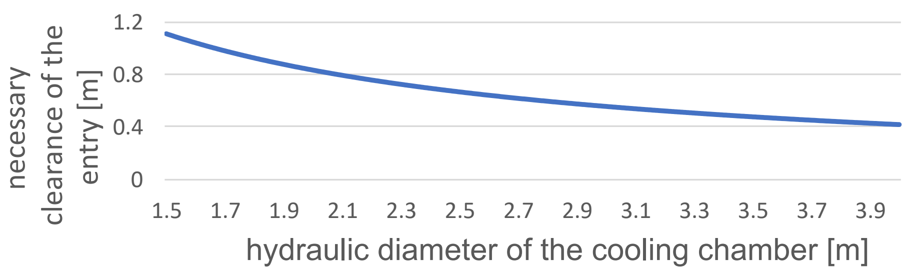

Figure 4.19: Necessary clearance to the entry of the icing wind tunnel for different hydraulic diameters of the cooling chamber.

4.7 Costs

The costs play an important role in the question of whether a project can be realized. Therefore a rough estimate of the costs of the building of the designed icing wind tunnel is presented. As there is no literature that offers formulas to calculate the costs, the estimations will be really coarse. The first point is the calculation of the necessary material volume for the wind tunnel parts. The surface area of all designed parts adds up to 26.70 m^2. Assuming a wall thickness of 5 mm, the material volume becomes 0.134 m^3. With the density of 2710 $kg\,m^{-3}$ of aluminum, the total material weight is 363.1 kg. The price of aluminum is 3.06 \$/kg according to MetalMiner [62]. This results in material costs of about 1100 \$. The share of material costs on the total costs is about 15% in the normal industry according to Wilting and Hanemaaijer [63]. Therefore the total manufacturing costs for the wind tunnel parts are 7300 \$. This calculation is however coarse and probably the real costs are higher, e.g. because of special alloys that need to be used because of the cold temperatures and the high humidity inside the wind tunnel.

Additionally, the spray system and the fan need to be bought. According to Spraying Systems Co. [64], the price for an automated system can be estimated to be in the region of 35,000 \$. Paint Booth Supply [65] lists the price of an axial fan, comparable to the selected one, at 3000 \$.

Therefore the total costs would sum up to about 45,300 \$. This is however just a very coarse estimation. Additionally, sensors to measure the pressure or the temperature for example were not considered yet.

4.8 Heat map

During the design of the icing wind tunnel different options were considered and the "result" is in the end more a recommendation than the only possible design. The final specifications for the chosen design are summarized in Table A.1 in the Appendix. To show the influence of some changes in parameters, a heat map was created that is presented in Table 4.6. The heat map presents the qualitative influence of a change of several parameter. Every change in the parameter that leads to an increase in size,

parameter of change	length	diameter	Δp_T	fan power	cooling	Δu	ΔT
current design	0	0	0	0	0	0	0
chord length	++	+	+	+	++	-	-
angle of attack	+	+	+	+	++	-	-
width	++	+	+	+	++	-	-
speed	0	0	++	++	++	++	++
AR diffuser	++	0	-	-	0	0	0
AR nozzle	+	+	+	+	0	0	- -
$T_{drop,0}$	0	0	0	0	+	0	+
air temperature	0	0	0	0	- -	0	-

Table 4.6: Impact of the increase of different parameters on the size, the total pressure losses and the necessary fan and cooling power of the icing wind tunnel, as well as on the final droplet deviations in temperature and velocity. $T_{drop,0}$ is used for the initial droplet temperature. Green color indicate positive changes, red negative changes.

typically leads to smaller final deviations in droplet temperature and velocity, but also to higher fan and cooling requirements. An exception is the area ratio of the diffuser that decreases the fan and cooling requirements because a higher area ratio leads to fewer pressure losses at the exit of the wind tunnel. Higher air speeds increase every aspect of the wind tunnel significantly.

4.9 CFD simulations

A lot of the equations used for the calculations are either empirically or use assumptions that can not always be fully fulfilled. Also some basic rules of thumb were considered while designing the components. As a first impression of whether the design might act as calculated, CFD simulations are helpful. CFD results for two different turbulence models were produced in 3D by Richard Hann with FENSAP-ICE. FENSAP-ICE is a part of the Ansys Fluid CFD program. It is specially designed for in-flight icing simulations in 3D. The used turbulence models were the Spalart-Allmaras model and the Menter $k-\omega$ SST. The results obtained with the Spalart-Allmaras model are presented here. For the ease of the simulation, just one quarter of the wind tunnel was simulated. This is possible because the wind tunnel is symmetric.

Figure 4.20 shows the velocity development of the air over the length of the icing wind tunnel. As the air velocity at the test section is almost $35\,\mathrm{m\,s^{-1}}$ the initial conditions are valid.

Figure 4.20: Plot of the velocity in the CFD simulation.

An important question is to know whether separation occurs inside the wind tunnel. This would lead to increased pressure losses and decreased flow quality. Therefore the quality of the results would be worse. A good indicator of separation is a surface stress of 0. This is because the surface stress is proportional to the wall-normal gradient of the velocity. As explained in subsection 2.2.1, the position where this gradient becomes zero is the point of separation. Therefore the CFD results were controlled for areas with surface stresses of 0. As shown in Figure 4.21 separation might especially occur in the corner of the nozzle and of the diffuser, but also in the corner of the test section.

Additionally, the pressure losses were calculated. To analyze the pressure losses inside the icing wind tunnel, the total pressure is averaged over the plane of interest and then compared to previous positions. The results for both turbulence models are shown in Table 4.7. The CFD simulations indicate much higher pressure losses for every component than the calculated values. The most probable reason is that the separation areas

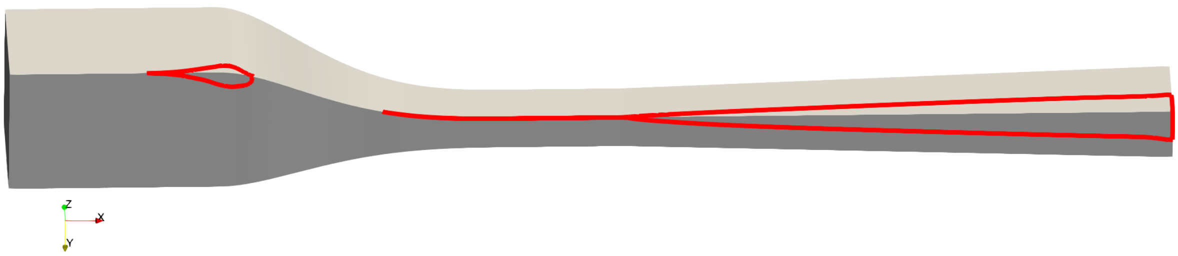

Figure 4.21: Plot of the separation zones in the CFD simulation.

lead to higher pressure losses than expected. If the pressure losses that were achieved with the CFD simulation are closer to the reality than the values calculated in subsection 4.5, a more powerful fan would be needed. The pressure losses according to the CFD simulation are about three times higher than the ones calculated in subsection 4.5. Therefore a fan would have to deliver at least a pressure rise of about 1000 Pa. The 43W718 by Aerovent [61] has the same dimensions as the fan selected previously and would be able to deliver the necessary pressure rise with a power need of 14.71 kW which is an increase of 83%. Therefore also the cooling requirements would increase to 27.03 kW compared to 20.23 kW before.

component	Spalart-Allmaras	Menter $k-\omega$ SST	calculated values
test section	33	27	13
nozzle	60	92	12
settling area	2	1	0
diffuser	125	156	48
total losses	220	276	73

Table 4.7: Comparison of the pressure losses according to the CFD simulations and the values calculated in Table 4.5. All values in Pa.

The results with the Menter $k-\omega$ SST model are presented in Appendix A.4. The velocity plot is almost exactly the same as for the Spalart-Allmaras model. The plot of the separation area shows more separation in the region of the diffuser for the Menter $k-\omega$ SST model, but overall a comparable result. The choice of the turbulence model therefore just has a minor influence on the results of the CFD simulations. Both results showed possible separation in the wind tunnel as well as higher pressure losses than calculated before. The explanation for the differences between the CFD results and the calculations can be caused by both sides. CFD results, especially with turbulence models, try to replicate the reality, but until today there are shortcomings. The calculations can also lead to wrong results, as some assumptions might have been wrong and many equations were developed empirically rather than being strictly physical.

4.10 Small icing wind tunnel

The NTNU owns a small cooling chamber. The dimensions of this chamber are approximately 3.8 m x 3.3 m. However, not even the whole space can be used, as some instruments are stored inside this room. Nevertheless, the availability of this cooling chamber lead to the thought of designing a small icing wind tunnel that would fit inside this chamber but of course has shortcomings compared to the big icing wind tunnel design.

As a first step, new requirements have to be found. They are summarized in Table 4.8. As presented earlier, the scaling of icing experiments is difficult. This is why the requirements cannot be reduced anymore without reducing the usability drastically. One changed specification arises because the cooling chamber can just be cooled down to $-10\,°\mathrm{C}$.

requirement	old value	new value
chord length	0.4 m	0.3 m
maximum angle of attack	8°	4°
unimpeded width of the test section	0.30 m	0.18 m
speed	$35\,\mathrm{m\,s^{-1}}$	$25\,\mathrm{m\,s^{-1}}$
fan duct length	0.10 m	0.05 m
air temperature	$-15\,°\mathrm{C}$	$-10\,°\mathrm{C}$

Table 4.8: Comparison of the (old) requirements for the big icing wind tunnel and the (new) simplified requirements for the small icing wind tunnel.

However, it was agreed to be all right with worse flow conditions inside the icing wind tunnel, as the small wind tunnel should mainly be for testing equipment and gaining experience. Therefore also slightly larger deviations of the droplet velocity and temperature can be accepted.

As the diffuser has a huge share of the overall length of the icing wind tunnel and the space is tight inside this cooling chamber, it was early decided that the area ratio of the diffuser has to be lower for this small tunnel than for the big one. This is because with a lower area ratio also the length of the diffuser is shorter. Therefore all calculations were done with an area ratio of 2 for the diffuser. All the other values were calculated

Version	diffuser AR	nozzle AR	IWT length [m]	pressure losses [Pa]
1	2	9	4.22	216
2	1.5	9	3.70	291
3	1	9	3.10	517
4	2	6	3.76	201
5	1.5	6	3.24	277

Table 4.9: Comparison of different options for a shorter icing wind tunnel (IWT).

as for the big icing wind tunnel. However, this lead to a too long wind tunnel. Some considerations were made about how the wind tunnel length could be reduced even further. They are presented in Table 4.9. Version 1 is the version calculated with the values as for the big tunnel except for the area ratio of 2 of the diffuser. Version 2 is a version with an even lower area ratio of the diffuser, while version 3 is a calculation without any diffuser at all. Versions 4 and 5 are calculations with a smaller area ratio of the nozzle, once with a high and once with a low area ratio of the diffuser.

It is obvious that lower area ratios reduce the length of the icing wind tunnel significantly. However, reducing the area ratio of the diffuser leads to higher pressure losses as the kinetic energy of the flow at the exit is higher. Therefore the version without a diffuser is not under further consideration. This is why version 5 was chosen in the end. The dimensions of the single components for this case can be found in Table 4.10.

Component	Length[m]	Dimensions[m]	
		Inlet	Outlet
fan duct	0.66	0.61	0.61
wide-angle diffuser	0.16	0.61	0.70 x 0.70 (0.70)
settling area	0.56	0.70 x 0.70 (0.70)	0.70 x 0.70 (0.70)
nozzle	0.79	0.70 x 0.70 (0.70)	0.24 x 0.34 (0.28)
test section	0.47	0.24 x 0.34 (0.28)	0.24 x 0.34 (0.28)
diffuser	0.60	0.24 x 0.34 (0.28)	0.30 x 0.40 (0.34)
wind tunnel	3.24	max 0.70 x 0.70 (0.70)	

Table 4.10: Dimensions of the small icing wind tunnel components. Two values are given in the dimensions column if the section is rectangular, one value if the section is round. If the section is rectangular, also the hydraulic diameter is given in brackets.

Version	IWT length [m]	total pressure losses [Pa]
Version 1 (Table 4.9)	4.22	216
chord length 0.25 m	3.82	192
angle of attack 3°	3.98	199
unimpeded width 0.15 m	3.94	197
all options combined	3.44	182

Table 4.11: Comparison of the influence of changed requirements for the shorter icing wind tunnel on the overall length and the total pressure losses.

It was also under consideration to reduce the requirements. Some examples are listed in Table 4.11. While a reduction of the requirements would also play a role to reduce the wind tunnel length, the usability of the icing wind tunnel would suffer badly. This is due to the mentioned problems with the scaling of results. As the option explained before seems to be able to fulfill the requirements under the space limitations nevertheless, a reduction of the requirements was skipped.

The maximum MVD that can be tested was also calculated for this small wind tunnel. In Figure 4.22(a) the final velocity deviation for droplets of different sizes is given. In Figure 4.22(b) the same is done for the temperature. With the designed small icing wind tunnel, a maximum diameter of slightly above 50 μm can be tested. By taking the Langmuir D distribution, the MVD of the corresponding distribution is about 23 μm. While this is much less than the highest MVD given in the EASA requirements, the MVD is still high enough to do reasonable experiments with the small icing wind tunnel.

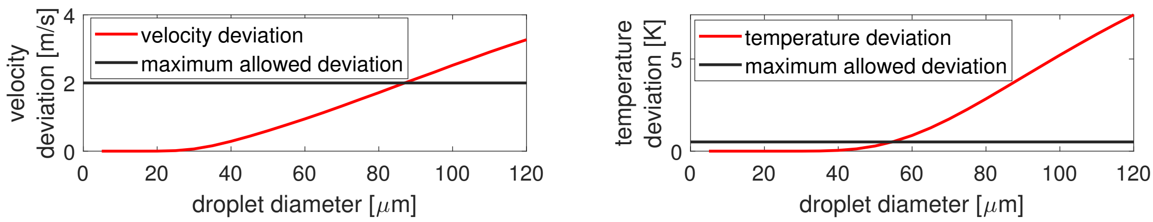

(a) Final velocity deviations.

(b) Final temperature deviations.

Figure 4.22: The final deviations in velocity and temperature for droplets with different diameters and for different water pressures inside the small icing wind tunnel.

The pressure losses for the single components and the wind tunnel in total can be calculated in the same way as done for the big one. The results can be found in Table

component	equation	K	pressure loss [Pa]
test section	3.28	0.022	9.40
test object	3.47	0.038	16.23
nozzle	3.31	0.013	5.55
settling area	3.28	0.012	0.14
spray system	3.47	0.205	2.44
screen	3.48	1.198	14.24
honeycombs	3.44	0.523	6.22
wide-angle-diffuser	3.51	0.594	19.82
fan duct	3.28	0.015	0.50
diffuser	3.32	0.028	11.96
exit losses	3.43	1.001	190.13
total losses			276.63

Table 4.12: Overview over the pressure losses in every component and in total for the small icing wind tunnel.

4.12. To counter the pressure losses, the fan must be able to deliver a pressure rise of about 415 Pa to have a safety margin for shortcomings in the calculations. Additionally, the fan will see a volume flow of about $2.0\,\mathrm{m^3\,s^{-1}}$. An example of a fan that might be suitable to fulfill these requirements is the model 24W722 by Aerovent [61]. It offers a pressure rise of about 436 Pa for a volume flow of $2.1\,\mathrm{m^3\,s^{-1}}$. If the fan is run under these maximum conditions, it will produce a heat of 1.33 kW.

Although no data is given for the cooling power of the climate chamber at the NTNU, the necessary cooling power is calculated. The necessary cooling power is plotted in Figure 4.23. The maximum cooling power necessary for the small icing wind tunnel is 3.942 kW. All specifications for the small icing wind tunnel are also summarized in Table A.1 in the Appendix.

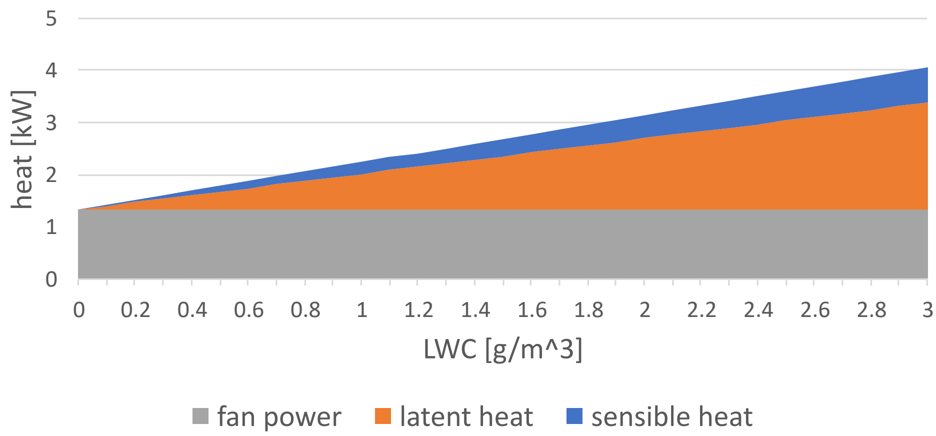

Figure 4.23: Required cooling power for the small wind tunnel for different LWCs at an air temperature of −10 °C.

5 Discussion

5.1 Conclusion and discussion

The usage of UAVs can be significantly influenced by ice accretions on the aircraft. To increase the usability, systems need to be designed that protect the aircraft in icing conditions. Therefore a better understanding of the physics behind the ice accretions is necessary. To do experiments, icing wind tunnels are often used as test facilities. Icing wind tunnels also offer the opportunity to test designed ice protection systems under realistic conditions. Today the number of icing wind tunnels is small. Additionally, most of the existing icing wind tunnels are designed for manned aircraft and not suitable for UAVs. This is why this thesis is about the design of a new icing wind tunnel for UAVs.

An objective for icing experiments is to do them with the conditions that occur in real life. This is why the designed icing wind tunnel can contain UAV airfoils with real-life chord lengths. Additionally, the wind tunnel will be able to accelerate the air to $35\,\mathrm{m\,s^{-1}}$ and therefore generate real-life air flows.

As the purpose of an icing wind tunnel is to simulate the ice accretions on the test object, the droplet behavior was calculated for the designed wind tunnel. The results show that the largest part of the typical icing environment can be tested in the designed icing wind tunnel. Additionally, the necessary nozzle length was given that is needed to do experiments with bigger droplets as well.

To run the wind tunnel, power is needed. The pressure losses in every component were calculated. The resulting total pressure loss will be balanced by an axial fan sitting as the most upstream part of the wind tunnel. In this thesis also a fan was presented that can offer the necessary power for the wind tunnel.

Without proper cooling, a reasonable run of the wind tunnel is impossible. Therefore, the requirements for the climate chamber that will contain the icing wind tunnel were formulated.

Preliminary CFD simulations were done to check the correctness of the calculations and the wind tunnel design. The results indicate the occurrence of flow separation in the corners of the wind tunnel. Additionally, the pressure losses of the CFD results are much higher than the ones calculated for the wind tunnel. Therefore the CFD results indicate that the designed wind tunnel needs more attention before it can be built.

The last part of the thesis was concerned with the down-scaling of the wind tunnel design. This was done as the NTNU owns a small climate room that could also be used as a climate chamber for an icing wind tunnel. However, its dimensions are too small to contain the icing wind tunnel with the requirements formulated for good scientific testing. Therefore a new list of requirements was formulated that can be held by a way smaller icing wind tunnel and still lead to some gain in knowledge. For this smaller icing wind tunnel, different design ideas were presented and compared.

Overall, during this thesis, the basic design of an icing wind tunnel specifically designed for UAVs is presented. The icing wind tunnel is comparable in test section size and air speed to the icing wind tunnels in Braunschweig (see Bansmer et al. [31]) and the VTT icing wind tunnel (see Tiihonen et al. [26]). According to the results, the designed icing wind tunnel is suitable as test facility for a wide range of icing experiments on UAVs.

The CFD simulations however showed some unsettled topics like separation and higher pressure losses. As the icing wind tunnel was just designed by using basic equations that often use simplifications, some uncertainties remain. Especially the droplet behavior was just calculated roughly and without taking turbulence into account. Additionally, the pressure losses differ by the factor three between calculations and the CFD results. With the uncertainty being so high, it is not sensible to select a fan. A further weakness of the work done so far is, that it was not possible yet to select a spray system for the icing wind tunnel.

Nevertheless, the design is a good starting point for a more detailed analysis. As there is a need for more icing wind tunnels for UAVs, it is absolutely recommended to continue the work and eventually build an icing wind tunnel based on this work.

5.2 Further work

The mentioned CFD results lead to the need for an overthinking of certain parts of the wind tunnel design. First, a deeper analysis of the CFD results is necessary to understand the reason for the flow separation and the higher pressure losses. If this knowledge is present, the design of the wind tunnel can be changed to reduce these effects. A first idea is to insert fillets in the corners as recommended by Barlow et al. [20]. Additionally, an other nozzle design can be checked to see if a change of the nozzle contour helps to reduce the separation area. Other possibilities are to make the nozzle longer or to reduce the opening angle of the diffuser.

A key step that needs to be taken on the way to a working icing wind tunnel is to select a suitable spray system. Some ideas were presented in section 4.3.3.1. It will probably be necessary to do detailed CFD simulations of the droplet behavior for different designs of a spray system.

Another topic for the future is to provide the necessary cooling power for the icing wind tunnel. This could be done by placing the wind tunnel in a climate chamber, by injecting liquid nitrogen, or by changing the design into a closed icing wind tunnel with a heat exchanger. If a decision is made, a CFD simulation of the icing wind tunnel and its environment is necessary to check that the flow quality is sufficient. This would be especially important for the inlet of an open return wind tunnel.

Once the icing wind tunnel is build, different instruments need to be installed, for example to measure the temperature, the speed or the water content in the icing wind tunnel. Afterwards, the icing wind tunnel and the instruments need to be calibrated as explained in SAE-ARP 5905 [66]. A thorough calibration is very helpful to have trust in the results of experiments. Especially the uniformity of the droplet cloud inside the test section should be checked to make sure that multiple measurements of the ice shapes are done at positions with comparable conditions.

Bibliography

[1] Bragg, M., Broeren, A., and Blumenthal, L. Iced-airfoil aerodynamics. *Progress in Aerospace Sciences*, 41(5):323–362, 2005.

[2] Kind, R., Potapczuk, M., Feo, A., Golia, C., and Shah, A. Experimental and computational simulation of in-flight icing phenomena. *Progress in Aerospace Sciences*, 34(5):257 – 345, 1998.

[3] Peck, L., Ryerson, C., and Martel, C. Army Aircraft Icing. ERDC/CRREL TR-02-13, US Army Corps of Engineers, 2002.

[4] Szilder, K. and McIlwain, S. In-Flight Icing of UAVs - The Influence of Reynolds Number on the Ice Accretion Process. In *SAE Technical Paper*. SAE International, 2011.

[5] Hann, R. *Atmospheric Ice Accretions, Aerodynamic Icing Penalties, and Ice Protection Systems on Unmanned Aerial Vehicles*. PhD thesis, Norwegian University of Science and Technology, 2020.

[6] Hann, R. and Johansen, T. A. Unsettled Topics in Unmanned Aerial Vehicle Icing. SAE EDGE Research Report EPR2020008, SAE International, 2020.

[7] European Aviation Safety Agency. *Certification Specifications and Acceptable Means of Compliance for Large Aeroplanes CS-25*, chapter Appendix C. 2016.

[8] Fajt, N., Hann, R., and Lutz, T. The Influence of Meteorological Conditions on the Icing Performance Penalties on a UAV Airfoil. In *8th European Conference for Aeronautics and Aerospace Sciences (EUCASS)*, 2019.

[9] Hann, R., Hearst, R. J., SÃ¦tran, L. R., and Bracchi, T. Experimental and Numerical Icing Penalties of an S826 Airfoil at Low Reynolds Numbers. *Aerospace*, 7(4), 2020.

[10] Lawson, C. Electrically Powered Ice Protection Systems for MALE UAVs - Requirements and Integration Challenges. In *25th Congress of International Council of Aeronautical Sciences*, 2006.

[11] Hann, R., Enache, A., Nielsen, M. C., Stovner, B. N., van Beeck, J., Johansen, T. A., and Borup, K. T. *UAV Icing: Experimental Heat Loads for Anti-Icing and De-Icing*. 2020.

[12] Anderson, J. *Fundamentals of Aerodynamics*. McGraw-Hill Education, 2010. ISBN 9780073398105.

[13] Versteeg, H. and Malalasekera, W. *An Introduction to Computational Fluid Dynamics: The Finite Volume Method*. Pearson Education Limited, 2007. ISBN 9780131274983.

[14] Gates, E., Lam, W., and Lozowski, E. Spray evolution in icing wind tunnels. *Cold Regions Science and Technology*, 15(1):65 – 74, 1988.

[15] Maritime Robotics. THE PX-31 Falk. `https://www.maritimerobotics.com/px-31`, 2019. Accessed: 2020-07-15.

[16] DJI. Agras T16 - Agricultural Spraying Drone. `https://www.dji.com/no/t16`, 2019. Accessed: 2020-07-03.

[17] DeGarmo, M. T. Issues Concerning Integration of Unmanned Aerial Vehicles in Civil Airspace. , MITRE, Center for Advanced Aviation System Development, McLean, Virginia, 2004.

[18] Gent, R. W., Dart, N., and Cansdale, J. T. Aircraft icing. *Philosophical Transactions of the Royal Society of London. Series A: Mathematical, Physical and Engineering Sciences*, 358:2873 – 2911, 2000.

[19] Hann, R. and Johansen, T. A. UAV Icing: The Influence of Airspeed and Chord Length on Performance Degradation. *Aircraft Engineering and Aerospace Technology*, submitted 2020.

[20] Barlow, J., Rae, W., and Pope, A. *Low-Speed Wind Tunnel Testing*. Aerospace engineering, mechanical engineering. Wiley, 1999. ISBN 9780471557746.

[21] Kulkarni, V., Sahoo, N., and Chavan, S. D. Simulation of honeycomb-screen combinations for turbulence management in a subsonic wind tunnel. *Journal of Wind Engineering and Industrial Aerodynamics*, 99(1):37 – 45, 2011.

[22] Arifuzzaman, M. and Mashud, M. Design Construction and Performance Test of a Low Cost Subsonic Wind Tunnel. *IOSR Journal of Engineering*, 02:83–92, 2012.

[23] IEA Wind Task 19. Available Technologiesfor Wind Energy in Cold Climates. Technical report, 2018.

[24] CIRA. Icing Wind Tunnel. `https://www.cira.it/en/research-infrastructures/icing-wind-tunnel-(iwt)/Icing%20Wind%20Tunnel`, 2017. Accessed: 2020-07-19.

[25] NASA Glenn Research Center. Icing Research Tunnel. `https://www1.grc.nasa.gov/facilities/irt/`, 2020. Accessed: 2020-07-19.

[26] Tiihonen, M., Jokela, T., Makkonen, L., and Bluemink, G.-J. VTT Icing wind tunnel 2.0. In *Winterwind Presentations 2016*, 2016.

[27] Cranfield University. Icing Tunnel. `https://www.cranfield.ac.uk/facilities/icing-tunnel`, 2020. Accessed: 2020-07-19.

[28] Flemming, R., Bond, T., and Britton, R. Results of a sub-scale model rotor icing test. In *29th Aerospace Sciences Meeting*, 1991.

[29] Brouwers, E., Palacios, J., Smith, E., and Peterson, A. The experimental investigation of a rotor hover icing model with shedding. *Annual Forum Proceedings - AHS International*, 4:2619–2635, 2010.

[30] Cao, Y. and Chen, K. Helicopter icing. *The Aeronautical Journal (1968)*, 114 (1152):83–90, 2010.

[31] Bansmer, S., Baumert, A., Sattler, S., Knop, I., Leroy, D., Schwarzenboeck, A., Jurkat-Witschas, T., Voigt, C., Pervier, H., and Esposito, B. Design, Construction and Commissioning of the Braunschweig Icing Wind Tunnel. *Atmospheric Measurement Techniques Discussions*, pages 1–51, 2017.

[32] Eckert, W., Mort, K., and Jope, J. Aerodynamic design guidelines and computer program for estimation of subsonic wind tunnel performance. TN D-8243, NASA, 1976.

[33] Bell, J. H. and Mehta, R. D. Contraction Design for Small Low-Speed Wind Tunnels. Tech. Rep. JIAA TR-84, Stanford University, 1988.

[34] Brassard, D. and Ferchichi, M. Transformation of a Polynomial for a Contraction Wall Profile . *Journal of Fluids Engineering*, 127(1):183–185, 2005.

[35] Morel, T. Comprehensive Design of Axisymmetric Wind Tunnel Contractions. *Journal of Fluids Engineering*, 97(2):225–233, 1975.

[36] Martin, J. S. Nozzle Design for a small, low-speed, closed-return wind tunnel. Bachelor's thesis, Houghton College, 2019.

[37] Mehta, R. D. *Aspects of the Design and Performance of Blower Wind Tunnel Components*. PhD thesis, Department of Aeronautics, Imperial College, University of London, 1978.

[38] Downie, J., Jordinson, R., and Barnes, F. On the design of three-dimensional wind tunnel contractions. *Aeronautical Journal*, 88:287–295, 1984.

[39] Mehta, R. and Bradshaw, P. Design rules for small low speed wind tunnels. *The Aeronautical Journal (1968)*, 83(827):443–453, 1979.

[40] Savio Srl. Axial fans and Centrifugal fans comparison. `https://www.savioclima.com/en/axial-fans-and-centrifugal-fans-comparison/`, 2016. Accessed: 2020-07-02.

[41] Hernández, M. A. G., López, A. I. M., Jarzabek, A. A., Perales, J. M. P., Wu, Y., and Xiaoxiao, S. Design Methodology for a Quick and Low-Cost Wind Tunnel. In *Wind Tunnel Designs and Their Diverse Engineering Applications*, chapter 1. IntechOpen, 2013.

[42] Langmuir, I. and Blodgett, K. *A Mathematical Investigation of Water Droplet Trajectories*. Army Air Forces technical report. Army Air Forces Headquarters, Air Technical Service Command, 1946.

[43] Morrison, F. A. Data Correlation for Drag Coefficient for Sphere. , Department of Chemical Engineering Michigan Technological University, 2016.

[44] PNR. Spray Engineering Handbook. `https://www.pnr-france.fr/site-web/IMG/pdf/ENGINEERING_HANDBOOK_CTG_SH07_BR.pdf`, 2012. Accessed: 2020-06-28.

[45] Knudsen, J. G. and Katz, D. L. V. *Fluid dynamics and heat transfer*. Huntington, N.Y. : R. E. Krieger Pub. Co, 1979. ISBN 978-0-88275-917-3.

[46] Greenway, M. and Wood, C. The Oxford University 4 m x 2 m Industrial Aerodynamics Wind Tunnel. *Journal of Wind Engineering and Industrial Aerodynamics*, 4(1):43–70, 1979.

[47] Chmielewski, G. E. Boundary-Layer Considerations in the Design of Aerodynamic Contractions. *Journal of Aircraft*, 11(8):435–438, 1974.

[48] Schlichting, H. *Boundary-Layer Theory*. McGraw-Hill, 1979.

[49] Nagel, A. and Shepshelovich, M. The concept of High-Lift, Mild Stall Wing. In *24th International Congress of the Aeronautical Sciences*, 2004.

[50] Airfoil Tools. RG-15 8.9% (rg15-il). `http://airfoiltools.com/airfoil/details?airfoil=rg15-il`, 2012. Accessed: 2020-07-05.

[51] Hann, R. UAV Icing: Ice Accretion Experiments and Validation. In *International Conference on Icing of Aircraft, Engines, and Structures*. SAE International, 2019.

[52] Çengel, Y. A. and Cimbala, J. M. *Fluid Mechanics: Fundamentals and Applications*. McGraw-Hill, 2014. ISBN 978-0-07-338032-2.

[53] Hare, D. E. and Sorensen, C. M. The density of supercooled water. II. Bulk samples cooled to the homogeneous nucleation limit. *The Journal of Chemical Physics*, 87 (8):4840–4845, 1987.

[54] Stepanov, I. Anomalous dependence of the heat capacity of supercooled water on pressure and temperature. *Results in Physics*, 4:28 – 30, 2014.

[55] Szedlak, A., Blanchard, A., Kostinski, A., and Cantrell, W. The Temperature Dependence of Water's Latent Heat of Freezing. *AGU Fall Meeting Abstracts*, 2009.

[56] Kreyszig, E., Kreyszig, H., and Norminton, E. J. *Advanced Engineering Mathematics*. John Wiley & Sons, Inc, 10th edition, 2011. ISBN 978-0-470-45836-5.

[57] Leone, G., Vecchione, L., Matteis, P. D., Szemskat, V., and Reister, A. The new CIRA Icing Wind Tunnel Spray Bar System development. In *38th Aerospace Sciences Meeting and Exhibit*, 2000.

[58] Spraying Systems Co. Autojet precision spray control systems. https://www.uk.spray.com/Literature_PDFs/B712C_Industrial_PulsaJet_Nozzles.pdf, 2017. Accessed: 2020-07-19.

[59] Spraying Systems Co. Automatic spray nozzles. https://www.spray.com/-/media/DAM/Sales-Materials/c/cat76AA_us_Automatic_B.pdf, 2017. page: 10. Accessed: 2020-07-19.

[60] Rocha, H. S. d., Marques, P. A. A., Camargo, A. P. d., Frizzone, J. A., and Saretta, E. Internal surface roughness of plastic pipes for irrigation. *Revista Brasileira de Engenharia Agrícola e Ambiental*, 21:143 – 149, 2017.

[61] Aerovent. Vaneaxial Fans. https://aerovent.com/wp-content/uploads/2018/12/Vaneaxial-Fans-Type-W-Models-VWBD-VW-Catalog-456.pdf, 2018. Accessed: 2020-07-05.

[62] MetalMiner. MetalMiner Prices: Aluminum Prices. https://agmetalminer.com/metal-prices/aluminum/, 2020. Accessed: 2020-07-13.

[63] Wilting, H. C. and Hanemaaijer, A. H. Share of raw material costs in total production costs. , PBL Netherlands Environmental Assessment Agency, 2014.

[64] Spraying Systems Co. Windshield Manufacturer Saves US$ 75,000 with Automated Spray System. https://www.spray.de/literature_pdfs/CS225_Windshield_Manufacturer_Saves_with_Auto_Spray_Sys.pdf, 2016. Accessed: 2020-07-13.

[65] Paint Booth Supply. 42 " "Aerovent" Tube Axial Fan Less Motor (For Use With 7.5HP). https://www.paintboothsupply.com/product_p/ata-42-075.htm, 2020. Accessed: 2020-07-13.

[66] SAE-ARP 5905. Calibration and Acceptance of Icing Wind Tunnels, 2015.

A Appendix

A.1 UAV Database

On the following pages, the UAV database with entries for 93 UAVs can be found. The references in the database belong to the reference list behind the table. The fields with the reference number are colored. This was done to show the trustworthiness of the source. Of course, having data of the manufacturer was always preferred but often just a few characteristics were given. Therefore also other, less reliable literature was checked. The color green indicates that the data was taken by the manufacturer or the US military. Yellow fields indicate that the source is a newspaper or scientific paper. The sources behind red fields are other websites that are not as trustworthy but still worth to be considered due to the data they listed.

	MTOW [kg]	Wingspan [m]	Length [m]	Cruise Speed [m/s]	Range [km]	Endurance [h]	Altitude [ft]	Aspect ratio	Chord [m]	Rotor/Prop dia? [m]	Type				
AAI (Textron) RQ-7A Shadow	150	3.90	3.4	58	735	5	14000	7	0.55			[8]	[6]	[9]	
AAI Aerosonde	25	2.95	1.7	31	3000	10	15000	15.3	0.2			[18]	[17]		
Aeromapper Avem	2	2.14		16.7	20	3	11500					[116]			
Aeronautics Defense Aerolight	40	4.00	2.56	25.6	150	4	10000					[124]	[125]		
Aeronautics Defense Orbiter 3	30	4.40			150	7	18000					[29]	[30]		
Aerostar Tactical UAS	230	8.70	4.5		250	12						[57]			
Aerovel Flexrotor	22	3.00	2	23	100	24+	18000			1.85		[104]			
AeroVironment RQ-14a Dragon Eye	2.7	1.10	0.9	10	5	1		3.7	0.3			[36]	[37]	[38]	[22]
AeroVironment RQ-20 Puma 3AE	6.8	2.80	1.4	18	60	2.5		7.4	0.38			[19]	[20]	[21]	[22]
AeroVironment Wasp AE-RQ 12A	1.3	1.02	0.76	10.3	5	0.8						[39]			
AeroVironment RQ-11B Raven	1.9	1.40	0.9	11.6	10	1.5	15000	6	0.22			[23]	[24]	[25]	[26]
AgEagle RX-60	3.2	1.37	0.7	17.9		1						[111]	[112]		
Airbus Atlante	570	8.00	5.47	37.5	200	10+	20000					[83]			
Airbus VSR700	700		6.2			10+	20000			7.2	rotary-wing	[123]			
Alpha 800	14		1.7	15.3		2.5	10000			1.8	rotary-wing	[119]			
Bayraktar Akinci	5500	20.00	12.2	83.3	11500	24	40000					[88]	[89]		
Bayraktar Mini UAV	5	2.00	1.2	30.9	15	1.33	3300					[92]	[93]		
Bayraktar TB2	630	12.00	6.5	36	150	24	27030					[90]			
Bayraktar VTOL	30	5.00	1.5	23.2-25.7	150	12	15000				hybrid	[91]			
BHE BXAP15	17	3.70	1.7	16.7-27.8	15	1.7	13000					[40]			
BlueBird SpyLite	9.5	2.75	1.35	27.8	50	4	30000					[58]	[59]		
BlueBird ThunderB	32	4.00	1.9	21.6	150	24	16000					[60]	[61]		
Boeing A160T Hummingbird	2950		10.7		4167	20+	30000			11	rotary-wing	[118]			
Boeing Insitu RQ-21 Blackjack	61	4.90	2.5	31	93	16+	19500					[10]	[11]		
Boeing Insitu ScanEagle	20	3.11	1.37	25		24+	19500	12.4	0.25			[12]	[13]		
Bramor C4EYE	4.5	2.30	0.96	16	40	3	16500					[82]			
C-Astral Atlas C4EYe	2.7	1.55	0.75	15	90	1.5	16500					[81]			
Chengdu Pterodactyl I (Wing Loong)	1100	14.00	9.05		4000	20	16500					[45]			
CTRM Aludra MK1	200	6.10	4.6	28.3	50	3	12000	8.23	0.6			[71]	[72]		
CTRM Aludra SR-08	2.1	0.81	0.425	18-36	15	1.67	13000					[69]	[70]		
CTRM Intisar 300			1.6		15	1.5	6500			1.77	rotary-wing	[122]			
Delair DT26M	15	3.30	1.6	15.8	50	2.25	10000					[109]			
Delair UX 11	1.5	1.10		15	53	1	20000					[107]	[108]		
DJI Agras MG-1	24.5		1.5	8		0.4				0.5	rotary-wing	[142]			
DJI Agras T16	40.5		2.5	7		0.3	6500			0.8	rotary-wing	[141]			
DRDO Nishant	275	6.57	4.63	34.7-41.7	160	4.5	12000					[54]			
eBee Classic	0.69	0.96		11-25	33	0.83						[85]			
Elbit Hermes 900	1180	15.00	8.7	30.9	4200	36	30000	16	0.937			[63]	[64]	[65]	
EMT Aladin	4	1.46	1.57	12.5	15	1	15000	8	0.18			[34]	[35]	[24]	
EMT Luna	40	4.17	2.36	19	100	6	16500					[51]			
FLIR Black hornet PRS	0.033		0.168	6	2	0.4				0.123	rotary-wing	[28]			
General Atomics Grey Eagle	1633	17.00	8.5	69.4	4630	25	29000					[101]	[102]	[103]	
General Atomics MQ-1B Predator	1,020	16.80	8.22	36	1250	24	25000	19	0.9			[5]	[6]	[7]	
General Atomics MQ-9 Reaper	4760	20.10	11	103	1850	14	50000	12	1.2			[128]	[129]	[130]	[131]
GIDS Shahpar	480	6.60	4.2	41.7	250	7	16500					[74]			
Honeywell RQ-16 T-Hawk	8.4		0.35	20.6		0.83	10000				rotary-wing	[126]	[127]		
Hydra Technologies Ehecati S4	55	3.70		19.5		8	15000					[73]			
IAI BIRD-EYE 650	11	3.00	1	20.6	20	4						[52]	[53]		
IAI Searcher Mk III	450	8.55	5.85	31-41	350	20	21000					[33]	[6]		

	MTOW [kg]	Wingspan [m]	Length [m]	Cruise Speed [m/s]	Range [km]	Endurance [h]	Altitude [ft]	Aspect ratio	Chord [m]	Rotor/Prop dia? [m]	Type				
IDS IA-17	27.5	2.80	1.27		80	5	15000					[66]			
Indonesian Aerospace Wulung	125	6.34	4.42	30.9	120	4	5500					[55]	[56]		
Innocon Micro Falcon LE	10	2.00		18-33.4	40	4	15000					[62]			
InstantEye M-3	0.25		0.3	9	9	0.5	12000				rotary-wing	[140]			
Leonardo Company Crex-B	2.1	1.70	0.45	10	10	1.25	10200					[67]			
Leonardo Company Mirach 40	70	1.50	2.5			1	26000					[68]			
Lipan M3	60	4.60	3.55	41.7	40	5	6500					[41]	[42]		
Lockheed Martin Condor XEP	8.3	3.70				6+	17000					[100]			
Lockheed Martin Sky Spirit ER	81.8	4.88	3.1	51.4	92.6	22	16000					[136]			
Lockheed Martin Stalker XE	10.9	3.70		15.6		8+	12000					[98]	[99]		
MaritimeRobotiocs PX-31	22	3.20	3.2	25		10	20000					[14]			
MartinUAV V-Bat	37.2	2.74	2.4	23.2	563	8+	15000					[97]			
MMIST CQ-10A Snow Goose	635	2.00	2.9		296	19	18000					[134]			
NCIST Cardinal II	5.5	1.30	1.9	15.3	8	1						[86]	[87]		
Northrop Grumman Bat UAS	159	4.26	2	33.4		18	17000					[96]			
Northrop Grumman MQ8-B Fire Scout	1428.8		9.2	41.2	200	8	20000			8.4	rotary-wing	[132]	[133]		
Northrop Grumman RQ-4 Block 30 Global Hawk	14,628	39.90	14.5	159	22780	32+	60000	25	1.6			[1]	[2]	[3]	[4]
Nostromo Yarara W	35	4.00	2.5	32	50	6	13000					[43]	[44]		
Prioria Maveric	1.16	0.75	0.91	18	15	1.5	10000					[27]			
ProxDynamics PD 100-RS	0.016				1	0.42				0.12	rotary-wing	[120]			
Qods Mohajer-4	175	5.30	3.64	50	1500	7	15000					[135]			
Raytheon Coyote	5.9	1.50	0.9	28.3	130	2	30000					[105]	[106]		
Rheinmetall DeTec KZO	161	3.42	2.25	42	140	5.5	13000					[31]			
Saxon Viper M10	20	3.00		22.2	100	8						[117]			
Skyfront Perimeter 8	19		2	9.7	177	5					rotary-wing	[139]			
Sperwer A Mk II		4.20	3.5	46.3	200	6	15000					[50]			
ST Aerospace Skyblade III	5	2.60	1.4	12.9	8	1						[79]	[80]		
Sunbirds SB4 Phoenix Solar	3.5	3.20	1.62	11.1	290	all day long						[115]			
Sunbirds Tigerwing	2.8	1.80	1.4	9.7	64	1.5						[114]			
TAI Anka	1600	17.30	8	56.6	200	24	30000					[94]	[95]		
Tekever AR4 Evo	4	2.10	1.35	15		2						[77]			
Tekever AR5	180	7.30	4	27.8		20						[78]			
Textron Systems Aerosonde Fixed Wing	45.5	3.70		23-33	140	14	15000					[32]			
Thales Fulmar X	20	3.00	1.2	27.8	800	12	10000					[84]			
Threod Eos C	13	4.76	1.83	14	50	3	10000					[46]	[47]		
Threod Stream C	40	3.90	2.3	22-28	150	6	9843					[48]	[49]		
Topcon Sirius Pro	2.7	1.63	1.2	18.1		0.83						[113]			
UAV Factory Penguin B	21.5	3.30	2.27	22		20+	16500	13.8	0.24			[15]	[16]		
Uconsystem Remo M-002	3.5	1.80	1.44		10	1.5						[110]			
V-200 Skeldar	235		4		200	5+	10000			4.6	rotary-wing	[121]			
WB Group FLYEYE mini UAV	11	3.60	1.9		30	2.5	13000					[75]			
WB Group FT-5 LOS Tactical UAV	85	6.40	3.1		180	12	16500					[76]			
XY Aviations FT-25D	90	2.50	3	97.2		0.45	16500	4.8	0.52			[138]			
XY Aviations H-150	105	4.90	2.92	36.1		4	10000	12	0.4			[137]			

References UAV Database

[1] Northrop Grumman (2016): "RQ-4 Block 30 Global Hawk". URL: http://web.archive.org/web/20200112193929/https://www.northropgrumman.com/Capabilities/GlobalHawk/Documents/GH_Brochure_B30.pdf (access: 20.01.2020)

[2] U.S. Air Force (2014, October 27): "RQ-4 Global Hawk". URL: https://www.af.mil/About-Us/Fact-Sheets/Display/Article/104516/rq-4-global-hawk/ (access: 20.01.2020)

[3] Zsolt Bottyán: "In-flight icing characteristics of unmanned aerial vehicles during special atmospheric condition over the carpathian-basin". Landscape & Environment 7 (2) 2013. 74-80

[4] Guy Norris (2001, January 30): "Unmanned Air Vehicles - Global leader". URL: https://www.flightglobal.com/unmanned-air-vehicles-global-leader/35917.article (access: 20.01.2020)

[5] U.S. Air Force (2015, September 23): "MQ-1B Predator". URL: https://www.af.mil/About-Us/Fact-Sheets/Display/Article/104469/mq-1b-predator/ (access: 20.01.2020)

[6] David Lednicer (2010, September 15): "The Incomplete Guide to Airfoil Usage". URL: https://m-selig.ae.illinois.edu/ads/aircraft.html (access: 20.01.2020)

[7] The Warfighter Encyclopedia (2001, January 27): "RQ-1 Predator". URL: https://web.archive.org/web/20041105115728/https://wrc.navair-rdte.navy.mil/warfighter_enc/aircraft/UAVs/predator.htm (access: 20.01.2020)

[8] Military Factory (2019, April 11): "AAI (Textron) RQ-7 Shadow". URL: https://www.militaryfactory.com/aircraft/detail.asp?aircraft_id=326 (access: 20.01.2020)

[9] RCGroups (2011, March 30): "Shadow 200 UAV – research". URL: https://www.rcgroups.com/forums/showthread.php?1415637-Shadow-200-UAV-research (access: 20.01.2020)

[10] Insitu (2015): "RQ-21A Blackjack". URL: https://www.insitu.com/images/uploads/pdfs/RQ-21ABlackjack_v2_ProductCard_PR120115.pdf (access: 20.01.2020)

[11] Hope Hodge Seck: "Marine Special Operators Fly New Surveillance Drone in Iraq". URL: https://www.military.com/daily-news/2016/10/08/marine-special-operators-fly-new-surveillance-drone-in-iraq.html?ERSC=todayinmil.sm (access: 20.01.2020)

[12] Insitu: "ScanEagle System". URL: https://web.archive.org/web/20130126192751/http://www.insitu.com/systems/scaneagle (access: 20.01.2020)

[13] RCGroups (2006, July 31): "ScanEagle UAV Project". URL: https://www.rcgroups.com/forums/showthread.php?549982-ScanEagle-UAV-Project (access: 20.01.2020)

[14] Maritime Robotics: "PX-31". URL: https://0257507f-59fc-4319-ab54-9d567d769b35.filesusr.com/ugd/a0d8a5_d4defc8e2e814a4dabeda68ee2b5cb74.pdf (access: 20.01.2020)

[15] UAV Factory: "Penguin B UAV platform". URL: https://www.uavfactory.com/product/46 (access: 20.01.2020)

[16] Airforce Technology: "Penguin B Unmanned Aerial Vehicle (UAV)". URL: https://www.airforce-technology.com/projects/penguin-b-unmanned-aerial-vehicle/ (access: 20.01.2020)

[17] Military Factory (2018, August 8): "AAI MQ-19 Aerosonde". URL: https://www.militaryfactory.com/aircraft/detail.asp?aircraft_id=1042 (access: 20.01.2020)

[18] Parvathavadhani Krishna Bahumanyam (2014, September 10): "Evaluation of Novel Wing design for UAV". URL: https://www.comsol.dk/paper/download/194633/bahumanyam_presentation.pdf (access: 20.01.2020)

[19] AeroVironment (2019): "PUMA™ 3 AE ALL ENVIRONMENT". URL: https://www.avinc.com/images /uploads/product_docs/Puma3AE_Datasheet_2019_v4.pdf (access: 20.01.2020)

[20] Jason Minnich (2017, May 1): "Solar Powering UAVs". URL: https://www.aerodefensetech.com/component/content/article/adt/features/articles/26830 (access: 20.01.2020)

[21] MAG Aerospace: "RQ-20 Puma". URL: https://magaero.com/rq-20-puma/ (access: 20.01.2020)

[22] Kim Lynge Sørensen (2016, September): "Autonomous Icing ProtectionSolution for Small UnmannedAircraft". URL: http://folk.ntnu.no/torarnj/Kim_thesis_12_09_2016.pdf (access: 20.01.2020)

[23] AeroVironment: "UAS: RQ-11B Raven". URL: https://www.avinc.com/uas/view/raven (access: 20.01.2020)

[24] Ralph D. Lorenz: "Titan Bumblebee: A 1kg Lander-Launched UAV Concept". JBIS, Vol. 61, pp.118-124, 2008

[25] Christopher K. Gilmore, Michael Chaykowsky, Brent Thomas (2019): "Autonomous Unmanned Aerial Vehicles for Blood Delivery". Rand Corporation. ISBN: 978-1-9774-0346-9

[26] U.S. Air Force (2017, March): "RQ-11B Raven". URL: https://www.af.mil/About-Us/Fact-Sheets/Display/Article/104533/rq-11b-raven/ (access: 20.01.2020)

[27] Prioria Robotics (2019): "Maveric UAS". URL: http://web.archive.org/web/20190527025715/http://www.prioria.com/maveric/ (access: 20.01.2020)

[28] FLIR (2019, January 4): "Black Hornet PRS". URL: https://flir.netx.net/file/asset/14121/original (access: 20.01.2020)

[29] Aeronautics: "Orbiter 3 Small Tactical UAS". URL: https://aeronautics-sys.com/wp-content/themes/aeronautics/pdf/orbiter_3.pdf (access: 20.01.2020)

[30] Arie Egozi (2015, March 3): "Vietnam ups interest in unmanned Orbiter 3". URL: https://www.flightglobal.com/military-uavs/vietnam-ups-interest-in-unmanned-orbiter-3/116093.article (access: 20.01.2020)

[31] Airbus: "KZO". URL: https://www.airbus.com/defence/uav.html (access: 20.01.2020)

[32] Textron Systems: "Aerosonde". URL: https://www.textronsystems.com/products/aerosonde (access: 20.01.2020)

[33] IAI: "Searcher Mk III". URL: https://www.iai.co.il/p/searcher-mk-iii (access: 20.01.2020)

[34] EMT Penzberg: "ALADIN Technical Data". URL: https://www.emt-penzberg.de/en/produkte/aladin/technical-data.html (access: 20.01.2020)

[35] EMT Penzberg: "ALADIN". URL: https://www.emt-penzberg.de/uploads/media/ALADIN_en_01.pdf (access: 20.01.2020)

[36] Avino: "Dragon Eye". URL: http://web.archive.org/web/20101227001758/http://www.avinc.com/downloads/Dragon_Eye_AV_datasheet.pdf (access: 20.01.2020)

[37] Andreas Parsch (2007): "AeroVironment RQ-14 Dragon Eye / Swift". URL: http://www.designation-systems.net/dusrm/app2/q-14.html (access: 20.01.2020)

[38] Kevin Reynolds et.al (2015, April 8): "The Opportunities and Challenges Associated With 3D Printing Aircraft Systems". URL: http://aero-comlab.stanford.edu/seminar/Presentations_2015/KReynolds_RDahlgren_2015.pdf (access: 20.01.2020)

[39] AeroVironment: "UAS: Wasp AE RQ-12A". URL: http://www.avinc.com/uas/view/wasp (access: 20.01.2020)

[40] BHE: "BHE UAV Brochure". URL: https://www.bhe-mw.eu/sites/default/files/documents/datasheet/uav_brossura_2014_v4a_eng_mail_lq_0.pdf (access: 20.01.2020)

[41] Nueve G’s (2010, January 20): "Lipán M3". URL: https://web.archive.org/web/20100603014536/http://nueveg.wordpress.com/2010/01/20/lipan-m3/ (access: 20.01.2020)

[42] Avia Pro (2016, June 27): "Lipan M3. Specifications. A photo". URL: http://avia-pro.net/blog/lipan-m3-tehnicheskie-harakteristiki-foto (access: 20.01.2020)

[43] Nostromo: "Unmanned Solutions". URL: https://nostromo-group.com/wp-content/uploads/2015/05/Nostromo_UAV_Technologies_Summary.pdf (access: 20.01.2020)

[44] Air Force Technology: "Nostromo Yarara Unmanned Aerial Vehicle (UAV)". URL: https://www.airforce-technology.com/projects/nostromo-yarara-uav/ (access: 20.01.2020)

[45] Robert Wall (2010, November 17): "China's Armed Predator". URL: http://web.archive.org/web/20121017214319/http://www.aviationweek.com/Blogs.aspx?plckBlogId=Blog:27ec4a53-dcc8-42d0-bd3a-01329aef79a7&plckController=Blog&plckScript= blogScript&plckElementId=blogDest&plckBlogPage=BlogViewPost&plckPostId=Blog:27ec4a53-dcc8-42d0-bd3a-01329aef79a7Post:e2c4ebce-729c-4722-b293-b3de048981d3 (access: 20.01.2020)

[46] Threod Systems: "EOS C UAS". URL: https://threod.com/product/eos-c-uas/ (access: 20.01.2020)

[47] Geo-matching: "Threod Systems EOS Mini UAS". URL: https://geo-matching.com/uas-for-mapping-and-3d-modelling/eos-mini-uas (access: 20.01.2020)

[48] Threod Systems: "STREAM C UAS". URL: https://threod.com/product/stream-c-uas/ (access: 20.01.2020)

[49] Pat Host (2019, May 2): "Xponential 2019: Threod Systems developing direction finder for Stream C VTOL UAV". URL: https://www.janes.com/article/88255/xponential-2019-threod-systems-developing-direction-finder-for-stream-c-vtol-uav (access: 20.01.2020)

[50] Safran Sagem: "SPERWER Mk.II TACTICAL UAV SYSTEM". URL: https://www.safran-electronics-defense.com/sites/sagem/files/d1446e-sperwer_mkii.pdf (access: 20.01.2020)

[51] EMT Penzberg: "LUNA Technical Data". URL: https://www.emt-penzberg.de/en/produkte/drohnensystem/spezifikationen.html (access: 20.01.2020)

[52] IAI: "BirdEye 650". URL: https://www.iai.co.il/p/birdeye-650 (access: 20.01.2020)

[53] Russian Unmanned Vehicle Systems Association: "Bird Eye 650".

URL: https://en.ruvsa.com/catalog/bird_eye_650/ (access: 20.01.2020)

[54] Vivek Bhardwaj (2015, October 21): DRDO Nishant Unmanned Aerial Vehicle (UAV),Indian Armed Forces. URL: http://aermech.in/drdo-nishant-unmanned-aerial-vehicle-uavindian-armed-forces/ (access: 20.01.2020)

[55] PT Dirgantara Indonesia: "UAV (Unmanned Aerial Vehicle) WULUNG". URL: https://www.indonesian-aerospace.com/techdev/index/set/uav (access: 20.01.2020)

[56] Greg Waldron (2016, May 4): "Indonesia makes progress with Wulung UAV". URL: https://www.flightglobal.com/civil-uavs/indonesia-makes-progress-with-wulung-uav/120484.article (access: 20.01.2020)

[57] Aeronautics: "Aerostar Tactical UAS". URL: http://aeronautics-sys.com/wp-content/themes/aeronautics/pdf/aerostar.pdf (access: 20.01.2020)

[58] BlueBird: "SpyLite". URL: http://www.bluebird-uav.com/spylite/ (access: 20.01.2020)

[59] Avia Pro (2016, December 13): "BlueBird SpyLite. Specifications. A photo". URL: http://avia-pro.net/blog/bluebird-spylite-tehnicheskie-harakteristiki-foto (access: 20.01.2020)

[60] BlueBird: "ThunderB". URL: http://www.bluebird-uav.com/thunderb-2/ (access: 20.01.2020)

[61] BlueBird: "ThunderB Long Endurance Tactical UAS". URL: http://www.bluebird-uav.com/wp-content/uploads/2018/07/BlueBird-ThunderB.pdf (access: 20.01.2020)

[62] DirectIndustry: "MicroFalcon brochure". URL: https://pdf.directindustry.com/pdf/innocon/ microfalcon-brochure/101647-286557-_2.html (access: 20.01.2020)

[63] Elbit Systems: "Hermes™ 900". URL: https://elbitsystems.com/products/uas/hermes-900/ (access: 20.01.2020)

[64] Defense Update (2009): "First Flight of the Elbit Systems Hermes 900 UAV". URL: https://web.archive.org/web/20170906091557/https://defense-update.com/features/2009/december/hermes900_first_flight_091209.html (access: 20.01.2020)

[65] State of Israel (2019, February 10): "TYPE CERTIFICATEDATASHEET NO. IA327". URL: https://caa.gov.il/index.php?option=com_docman&view=download&alias=8118-tcds-ia327&category_slug=tc-2&Itemid=669&lang=he (access: 20.01.2020)

[66] IDS (2019): "IA-17 is a small fixed wing UAV". URL: https://www.idscorporation.com/pf/ia-17/#1481041686162-8652efc6-06ecdb70-83b62d44-7c9e (access: 20.01.2020)

[67] Leonardo: "CREX-B". URL: https://www.leonardocompany.com/documents/20142/3148889/CREX_B_LQ_mm07807_.pdf?t=1538987370086 (access: 20.01.2020)

[68] Leonardo: "MIRACH 40". URL: https://www.leonardocompany.com/documents/20142/3149330/Mirach_40_Integrated_Aerial_Target_System_LQ_mm08519_.pdf?t=1538987433406 (access: 20.01.2020)

[69] CTRM: "Unmanned Systems Technology Sdn Bhd (The ALUDRA SR-08)". URL: https://www.ctrm.com.my/ps_alu_sr.php (access: 20.01.2020)

[70] Tan Kar Zhen, Muhammed Zubair, Kamarul Arifin Ahmad: "Experimental and Numerical Investigation of the Effects of Passive Vortex Generators on Aludra UAV Performance". Chinese Journal of Aeronautics 24(2011) 577-58

[71] CTRM: "Unmanned Systems Technology Sdn Bhd (The Aludra MK1)". URL: https://www.ctrm.com.my/ps_alu_mk1.php (access: 20.01.2020)

[72] Nur Nabillah Mohd Kamal et.al.: "Comparison Study Between Schrenk's Approximation Method and Computational Fluid Dynamics of Aerodynamic Loading on UAV NACA 4415 Wing". Journal of Advanced Research in Fluid Mechanics and Thermal Sciences64, Issue 2(2019) 283-292

[73] Peter La Franchi (2007, June 18): "Mexico throws its hat into the ring with Ehecatl". URL: https://www.flightglobal.com/mexico-throws-its-hat-into-the-ring-with-ehecatl/74391.article (access: 20.01.2020)

[74] GIDS: "Shahpar". URL: http://gids.com.pk/shahpar (access: 20.01.2020)

[75] WB Group: "FLYEYE mini UAS". URL: https://www.wbgroup.pl/en/produkt/flyeye-mini-uav/ (access: 20.01.2020)

[76] WB Group: "FT-5 LOS tactical UAV". URL: https://www.wbgroup.pl/en/produkt/ft-5-los-tactical-uav/ (access: 20.01.2020)

[77] Tekever: "Tekever AR4". URL: http://airray.tekever.com/ar4-evo/ (access: 20.01.2020)

[78] Tekever: "Tekever AR5". URL: http://airray.tekever.com/ar5/ (access: 20.01.2020)

[79] ST Aerospace: "Skyblade III". URL: https://web.archive.org/web/20110531152537/http://www.staero.aero/www/keyoffering.asp?serkeyid=ODAwMDAwMTg (access: 20.01.2020)

[80] Mindef Singapore (2012, October 10): "Fact Sheet: Skyblade III Mini-unmanned Aerial Vehicle". URL: https://www.mindef.gov.sg/web/portal/mindef/news-and-events/latest-releases/article-detail/2012/october/2012oct10-news-releases-00215 (access: 20.01.2020)

[81] C-Astral: "Atlas C4EYE". URL: http://www.c-astral.com/en/unmanned-systems/atlas-c4eye#0 (access: 20.01.2020)

[82] C-Astral: "Bramor C4EYE". URL: http://www.c-astral.com/en/unmanned-systems/bramor-c4eye (access: 20.01.2020)

[83] Airbus: "Atlante". URL: https://www.airbus.com/defence/uav.html (access: 20.01.2020)

[84] Thales: "Fulmar X". URL: https://www.thalesgroup.com/en/fulmar-x#carousel-1263279395 (access: 20.01.2020)

[85] senseFly: "eBee Classic". URL: https://www.sensefly.com/drone/ebee-mapping-drone/ (access: 20.01.2020)

[86] NCIST: "Cardinal II Unmanned Aircraft System". URL: http://www.ncsist.org.tw/eng/csistdup/products/product.aspx?product_id=268&catalog=41 (access: 20.01.2020)

[87] AirForce Technology: "Cardinal II Unmanned Aircraft System". URL: https://www.airforce-technology.com/projects/cardinal-ii-unmanned-aircraft-system/ (access: 20.01.2020)

[88] Baykar: "Bayraktar Akinci System". URL: https://baykardefence.com/uav-14.html (access: 20.01.2020)

[89] Military Factory (2019, December 10): "Bayraktar Akinci (Raider)". URL: https://www.militaryfactory.com/aircraft/detail.asp?aircraft_id=1995 (access: 20.01.2020)

[90] Baykar: "Bayraktar TB2". URL: https://baykardefence.com/uav-15.html (access: 20.01.2020)

[91] Baykar: "Bayraktar VTOL UAV". URL: https://baykardefence.com/uav-17.html (access: 20.01.2020)

[92] Baykar: "Bayraktar Mini UAV". URL: https://baykardefence.com/uav-16.html (access: 20.01.2020)

[93] Russian Unmanned Vehicle Systems Association: "Bayraktar Mini UAV System". URL: https://en.ruvsa.com/catalog/bayraktar_mini_uav_system/ (access: 20.01.2020)

[94] Turkish Aerospace: "ANKA". URL: https://www.tusas.com/en/product/anka-multi-role-isr-system (access: 20.01.2020)

[95] TAI (2011): "ANKA". URL: https://web.archive.org/web/20110722124219/http://www.tai.com.tr/ds_Resource/image/content/ANKA-ENG.pdf (access: 20.01.2020)

[96] Northrop Grumman (2017): "Bat UAS™". URL: http://web.archive.org/web/20180313092822/https://www.northropgrumman.com/Capabilities/BATUAS/Documents/pageDocuments/BAT_Datasheet.pdf (access: 20.01.2020)

[97] Martin UAV: "V-BAT". URL: http://martinuav.com/portfolio/v-bat/ (access: 20.01.2020)

[98] Lockheed Martin: "Stalker XE UAS". URL: https://www.lockheedmartin.com/en-us/products/stalker.html (access: 20.01.2020)

[99] Lockheed Martin (2018, May 22): "Lockheed Martin Stalker XE Upgraded with New VTOL Launch and Landing Capability". URL: https://news.lockheedmartin.com/2018-May-22-Lockheed-Martin-Stalker-XE-Upgraded-with-New-VTOL-Launch-and-Landing-Capability (access: 20.01.2020)

[100] Lockheed Martin: "Condor™ eXtended Endurance & Payload (XEP)". URL: https://www.lockheedmartin.com/en-us/products/condor-extended-endurance-payload.html (access: 20.01.2020)

[101] General Atomics Aeronautical (2014): "GRAY EAGLE". URL: http://www.ga-asi.com/Websites/gaasi/images/products/aircraft_systems/pdf/Gray_Eagle021915.pdf (access: 20.01.2020)

[102] U.S. Army: "MQ-1C Gray Eagle Unmanned Aircraft System (UAS)". URL: https://asc.army.mil/web/portfolio-item/aviation_gray-eagle-uas/ (access: 20.01.2020)

[103] GlobalSecurity: "MQ-1C Grey Eagle". URL: https://www.globalsecurity.org/military/systems/aircraft/warrior.htm (access: 20.01.2020)

[104] Aerovel: "Flexrotor". URL: https://aerovel.com/flexrotor/ (access: 20.01.2020)

[105] Joseph J. Cione (2016, October 25): "The Coyote Unmanned Aircraft System". URL: http://web.archive.org/web/20170924182211/https://swfsc.noaa.gov/uploadedFiles/Events/Meetings/UAS_2016/Presentation/Cione_UAS_SD2.pdf (access: 20.01.2020)

[106] David Vergun (2019, June 29): "Tucson Tech: Coyote gets new teeth as Raytheon builds counter-drone tech". URL: http://web.archive.org/web/20190701135328/https://tucson.com/business/ tucson-tech-coyote-gets-new-teeth-as-raytheon-builds-counter/article_ec3aec46-c998-5893-9ec6-8c56e8b066e7.html (access: 20.01.2020)

[107] Delair: "UX11". URL: https://delair.aero/wp-content/uploads/2019/04/Datasheet-Delair-UX11-V032019-EN.pdf (access: 20.01.2020)

[108] Delair: "Frequently Asked Questions Delair UX11". URL: https://delair.aero/professional-drones-2/professional-mapping-drone-delair-ux11/delair-ux11-frequently-asked-questions/#1555405396213-a805e8c5-9427 (access: 20.01.2020)

[109] Delair: "DT26M". URL: https://delair.aero/wp-content/uploads/2018/01/Delair-datasheet-DT26M_WEB_Oct2017vA.pdf (access: 20.01.2020)

[110] Uconsystem: "REMO M-002". URL: http://www.uconsystem.com/eng/products/industrial/remom-002.asp (access: 20.01.2020)

[111] AgEagle Aerial Systems (2018, August): "AgEagle RX-60". URL: https://2af5709d-5d5d-42ce-b099-b35395abb99f.filesusr.com/ugd/89e3c5_e3de865b41b644fbb68adea13706723c.pdf?index=true (access: 20.01.2020)

[112] Molly McMillin (2017, March 27): "Sales soar at AgEagle, Neodesha-based drone manufacturer". URL: https://www-1.kansas.com/news/business/aviation/article1138377.html# (access: 20.01.2020)

[113] Topcon: "Sirius Pro Specifications". URL: https://www.topconpositioning.com/mass-data-collection/aerial-mapping/sirius-pro#panel-product-specifications (access: 20.01.2020)

[114] Sunbirds: "SUNBIRDS TIGERWING". URL: https://sunbirds.aero/tigerwing (access: 20.01.2020)

[115] Sunbirds: "SB4 PHOENIX SOLAR-POWERED DRONE". URL: https://sunbirds.aero/sb4-phoenix-long-range (access: 20.01.2020)

[116] Aeromapper: "Meet The AVEM". URL: https://www.aeromapper.com/avem/ (access: 20.01.2020)

[117] Saxon Remote Systems: "Saxon Viper M10". URL: https://www.saxonremotesystems.com/viper-m-series-uas (access: 20.01.2020)

[118] Boeing (2010, June): "A160T Hummingbird". URL: https://web.archive.org/web/20140515080454/http://www.uvsr.org/docs/Boeing_A160T-Hummingbird_201006.pdf (access: 20.01.2020)

[119] Alpha Unmanned Systems: "Alpha 800 UAV Helicopter. Technical specifications". URL: https://alphaunmannedsystems.com/alpha-800-technical-specifications/ (access: 20.01.2020)

[120] Prox Dynamics: "PD-100 PRS". URL: https://web.archive.org/web/20140121141151/http://www.proxdynamics.com/products/pd_100_prs/ (access: 20.01.2020)

[121] UMS SKELDAR: "V-200 SKELDAR". URL: https://umsskeldar.aero/our-products/rpas-systems/v-200-skeldar/ (access: 20.01.2020)

[122] CTRM: "Unmanned Systems Technology Sdn Bhd (The INTISAR 300)". URL: https://www.ctrm.com.my/ps_int_300.php (access: 20.01.2020)

[123] Airbus: "VSR700". URL: https://www.airbus.com/helicopters/UAS/VSR700.html (access: 20.01.2020)

[124] Shepard Press (2008): "Unmanned Vehicles. Handbook 2008". ISSN: 1365-6546

[125] AirForce Technology: "Aerolight Unmanned Aerial Vehicle". URL: https://www.airforce-technology.com/projects/aerolight-uav/ (access: 20.01.2020)

[126] AvionicsVideos (2009, August 10): "Honeywell T Hawk Described". URL: https://www.youtube.com/watch?v=8k8_lpwyqBM (access: 20.01.2020)

[127] Honeywell (2010, June 14): "Honeywell T-Hawk™ Unmanned Aerial Vehicle Reaches 10,000 Flight Milestone". URL: http://www51.honeywell.com/honeywell/news-events/press-releases-details/06.15.10T-HawkReachesMilestone.html (access: 20.01.2020)

[128] U.S. Air Force (2015, September): "MQ-9 Reaper". URL: https://www.af.mil/About-Us/Fact-Sheets/Display/Article/104470/mq-9-reaper/ (access: 20.01.2020)

[129] Aviation (2017, November 6): "What airfoil design does the MQ-9 Reaper UAV use?". URL: https://aviation.stackexchange.com/questions/45407/what-airfoil-design-does-the-mq-9-reaper-uav-use (access: 20.01.2020)

[130] Defense Update: "MQ-9 Reaper Hunter/Killer UAV". URL: https://web.archive.org/web/20101122084244/http://www.defense-update.com/products/p/predatorB.htm (access: 20.01.2020)

[131] GitHub (2016, July 8): "MQ-9-JSBSim2.xml". URL: https://github.com/meirm/MQ-9/blob/master/MQ-9-JSBSim2.xml (access: 20.01.2020)

[132] Northrop Grumman (2012): "MQ-8B Fire Scout". URL: https://web.archive.org/web/20140420235117/http://www.northropgrumman.com/Capabilities/FireScout/Documents/pageDocuments/MQ-8B_Fire_Scout_Data_Sheet.pdf (access: 20.01.2020)

[133] NAVAIR: "MQ-8B Fire Scout". URL: https://www.navair.navy.mil/product/mq-8b (access: 20.01.2020)

[134] March Field Air Museum: "CQ-10A (UAV) Snow Goose". URL: https://www.marchfield.org/aircraft/unmanned/cq-10a-uav-snow-goose-mist-mobility/ (access: 20.01.2020)

[135] Mashregnews (2008, October 21): "Mohajers 3 and 4 Permit to enter the Iranian Premier League + photo" URL: https://www.mashreghnews.ir/news/70051/%D9%85%D9%87%D8%A7%D8%AC%D8%B13-%D9%88-4-%D9%85%D8%AC%D9%88%D8%B2-%D9%88%D8%B1%D9%88%D8%AF-%D8%A7%DB%8C%D8%B1%D8%A7%D9%86-%D8%A8%D9%87-%D9%84%DB%8C%DA%AF-%D8%A8%D8%B1%D8%AA%D8%B1-%D9%87%D9%88%D8%A7%D9%BE%DB%8C%D9%85%D8%A7%D9%87%D8%A7%DB%8C-%D8%A8%D8%AF%D9%88%D9%86-%D8%B3%D8%B1%D9%86%D8%B4%DB%8C%D9%86 (access: 20.01.2020)

[136] Defense Update (2007, August 28): "Sky Spirt Mini UAV". URL: https://defense-update.com/20070828_sky_spirit.html (access: 20.01.2020)

[137] XY Aviations: "Product name: H-150". URL: https://web.archive.org/web/20131202230724/http://www.xy-aviation.com/products_show.asp?id=98 (access: 20.01.2020)

[138] XY Aviations: "Product name: FT-25D". URL: https://web.archive.org/web/20131202222235/http://www.xy-aviation.com/products_show.asp?id=100 (access: 20.01.2020)

[139] Skyfront: "Perimeter 8". URL: https://skyfront.com/perimeter-8/ (access: 20.01.2020)

[140] InstantEye Robotics: "IntantEye Mk-3 GEN5-D1-D2". URL: https://instanteyerobotics.com/wp-content/uploads/2019/11/InstantEye-Mk-3-GEN5-D1-D2-V9.pdf (access: 20.01.2020)

[141] DJI: "Agras T16". URL: https://www.dji.com/no/t16/info#specs (access: 20.01.2020)

[142] DJI: "Agras MG-1". URL: https://www.dji.com/no/mg-1/info#specs (access: 20.01.2020)

A.2 Additional Figures

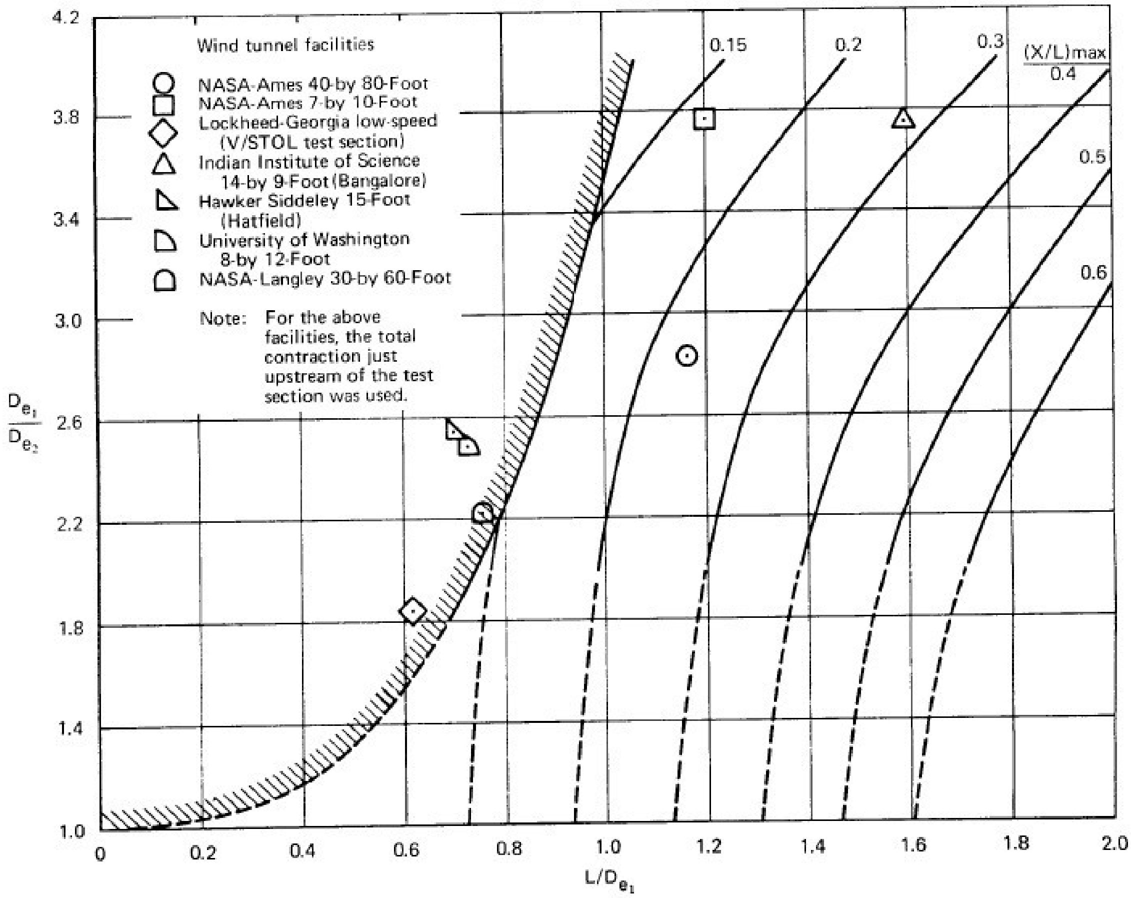

Figure A.1: Design rules for the length of nozzles for different ratios of inlet to outlet diameter. Adapted from Eckert et al. [32].

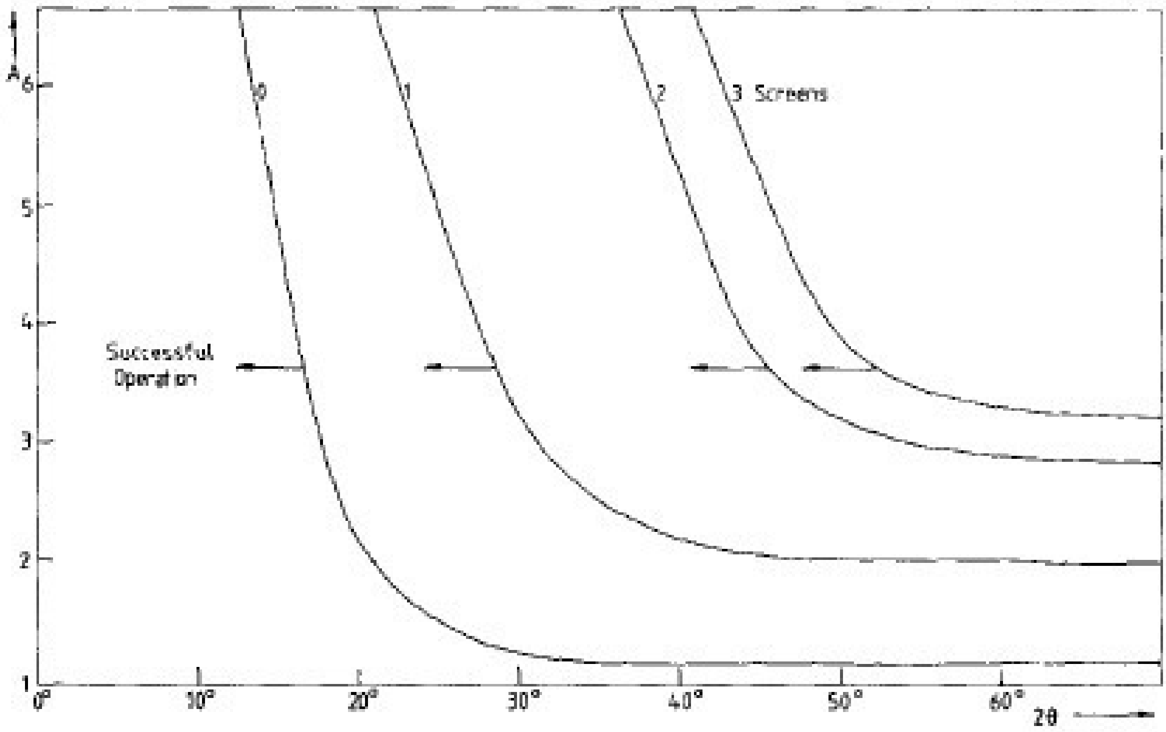

Figure A.2: Necessary number of screens in the wide-angle diffuser for certain opening angles and area ratios. Adapted from Mehta and Bradshaw [39].

A.3 The RG15 airfoil

Here, the coordinates of the surface of an RG 15 airfoil are plotted. The x-axis is the axis in flow direction. The z-axis is perpendicular to the x-axis. Both axes are normalized with the chord length of the airfoil. Therefore the x-axis has values between 0 and 1.

x-position	z-position
1.000000	0.000000
0.996710	0.000540
0.987260	0.002290
0.972370	0.005140
0.952480	0.008650
0.927640	0.012540
0.898100	0.016850
0.864270	0.021520
0.826600	0.026440
0.785570	0.031490
0.741650	0.036540
0.695370	0.041460
0.647230	0.046120
0.597780	0.050390
0.547530	0.054140
0.497020	0.057270
0.446760	0.059660
0.397270	0.061230
0.349020	0.061900
0.302480	0.061620
0.258090	0.060360
0.216240	0.058100
0.177300	0.054860
0.141610	0.050680
0.109450	0.045640
0.081080	0.039850
0.056730	0.033430
0.036580	0.026540
0.020760	0.019350
0.009320	0.012140
0.002350	0.005260
0.000000	0.000000
0.000020	-0.000480
0.003360	-0.005340
0.012470	-0.010060
0.026700	-0.014360
0.045960	-0.018110
0.070100	-0.021230
0.098960	-0.023720
0.132240	-0.025590
0.169630	-0.026880
0.210730	-0.027620
0.255090	-0.027850
0.302210	-0.027620
0.351560	-0.026960
0.402570	-0.025900
0.454630	-0.024460
0.507130	-0.022620
0.559440	-0.020250
0.611280	-0.017170
0.662440	-0.013660
0.712370	-0.010150
0.760370	-0.006910
0.805750	-0.004130
0.847790	-0.001920
0.885830	-0.000340
0.919250	0.000620
0.947480	0.001010
0.970030	0.000970
0.986520	0.000640
0.996600	0.000210
1.000000	0.000000

The shape of an RG15 airfoil with an angle of attack of 0° is shown in Figure A.3.

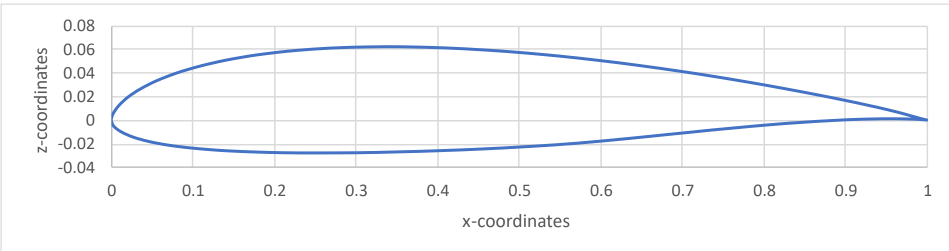

Figure A.3: The RG15 airfoil with an angle of attack of 0°. Axes are normalized with the chord length.

A.4 CFD simulation using the Menter $k-\omega$ SST model

As explained in subsection 2.2.1, the impact of turbulence is modeled in our CFD simulations. By modeling the turbulence, the calculated flow field can differ from the true flow field. Therefore doing a comparison with at least a second turbulence model is always reasonable. For this thesis, the CFD simulations were done with two different turbulence models. The results of the Spalart-Allmaras model were presented in the main part of the thesis. The velocity plot of the simulation with the Menter $k-\omega$ SST model is shown in Figure A.4.

Figure A.4: Velocity plot of the CFD simulation with a second turbulence model.

The flow field looks similar to the one calculated with the Spalart-Allmaras turbulence model. The same is true for the separation plot in Figure A.5. The pressure losses of both models were already presented in Table 4.7. While the two simulations show small differences, they are much closer to each other than two the values calculated with the basic equations given mostly by Eckert et al. [32].

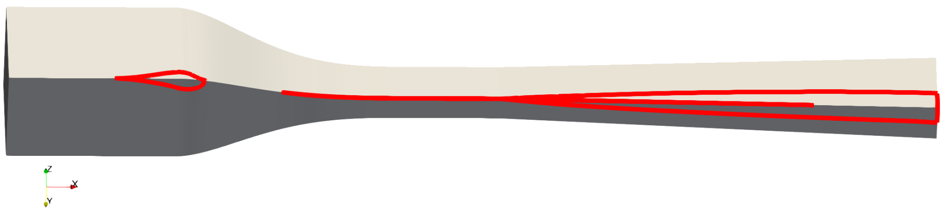

Figure A.5: Plot of the separation zones in the CFD simulation with a second turbulence model.

The comparison of the two different turbulence models showed just very small differences. Therefore the differences between CFD simulations and the values calculated with algebraic equations depends not on the choice of the turbulence model.

A.5 Icing wind tunnel specifications

The final specifications of the two icing wind tunnels designed in this thesis are compared in Table A.1.

parameter	big icing wind tunnel	small icing wind tunnel
maximum speed at test section	$35\,\mathrm{m\,s^{-1}}$	$25\,\mathrm{m\,s^{-1}}$
maximum chord length	0.4 m	0.3 m
maximum angle of attack	8°	4°
unimpeded test section width	0.30 m	0.18 m
minimum air temperature	−15 °C	−10 °C
maximum MVD	$38\,\mu$m	$23\,\mu$m
wind tunnel length	8.03 m	3.24 m
maximum cross-section	1.54 m x 1.54 m	0.70 m x 0.70 m
fan power	8.024 kW	1.33 kW
necessary cooling power	20.52 kW	3.942 kW

Table A.1: Comparison of the specifications of the big and the small icing wind tunnel.